THE AUSTRALIAN NATIONAL UNIVERSITY

Hydraulic and Physical Properties of Friable Regolith

Michael Lorn Turner

December 2007

A thesis submitted for the degree of Doctor of Philosophy of The Australian National University.

Research School of Physical Sciences,

Department of Applied Mathematics.

The Australian National University.

Except where otherwise stated, this thesis is my own work,

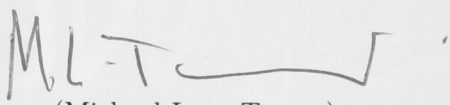

(Michael Lorn Turner)

Aknowledgements

I am deeply indebted to my supervisory panel, Professor Mark Knackstedt, and Assoc. Professor Tim Senden for their continual support, guidance, patience, and trust. I appreciate your encouragement and dedication to the cause.

In addition, I would like to thank my adviser Dr. Bear McPhail, and the Cooperative Research Centre for Environments and Mineral Exploration and the Research School of Physical Science and Engineering at the Australian National University for their support of my research. Colleagues at the Department of Applied Mathematics deserve special mention for always remembering to ask how my thesis was progressing - despite knowing that the answer would usually be curt. In this regard, I would like to make special mention of my friends at the Thursday night bible study who never missed an opportunity to remind me that I was finishing last week.

I would like to express thanks to my family. To my mother for concern about all and sundry even when none was warranted and for her ability to be interested just for the sake of it. My Dad for continuing to ask why the thesis is taking so long but believing none the less that one day it would actually be completed. And most importantly, I acknowledge my wife, Claudia, not only for her constant support, tolerance and belief that one day it would all be over, but also for not bailing out. I love you.

Abstract

A high-resolution and large-field x-ray micro-CT facility has been used to obtain the 3D structure of four unconsolidated sediment samples. Three of the four images, two Ottawa sand samples and a sandy sediment from an active river bed (LRC), can be considered high quality. In these three samples the x-ray attenuation data allowed unambiguous phase separation of the pore and mineral phase peaks. This enabled direct structural analysis of the pores and particles in detail. A fourth sample, which exhibited pore and particle sizes across many orders of magnitude was more difficult to analyse quantitatively.

Particle size distribution (PSD) was obtained from analysis of the 3D images and direct enumeration of the particle size statistics was undertaken. These data were compared to the conventional methods of sieve and laser light scattering (LLS). Analysis of the digital data included a measure of the long, intermediate and short axes of each individual particle. The comparison of these different axes measures to the experimental data showed that the PSD from sieve is slightly larger than the measured short axis and the LLS is slightly smaller than the long axes derived from the digital data. This result quantifies differences reported previously between sieve and LLS data. The differences could provide a means to estimate the variation of aspect ratio in particle sizes and illustrates the value of this digital analysis for granular systems.

Textural data is also available from the image anlysis and the sphericity and Zingg ratio measures showed that the 3 homogeneous samples contain particles with a sphericity value of between 0.75 and 0.77. The calculation of the Zingg ratio also showed that the LRC and the two Ottawa samples are largely made up of compact grains with similar mean aspect ratios.

One of the more important packing characteristics is the co-ordination number. Large differences in grain co-ordination is observed for the 3 samples. The well sorted samples have very low co-ordination numbers characterised by a very tight distribution range, the more disordered samples in

contrast, exhibited large co-ordination numbers and ranges many times as large.

The structure of the pore space in 3D is measured directly on the 3D image. Pore-size distribution, pore and throat statistics of the complex media, shape and interconnectivity of the unconsolidated sediment samples is directly enumerated. From the particle and pore partitioning of the image data we quantitatively probe whether pore and particle sizes are correlated. From this analysis we see that particle and pore size are *not* spatially correlated and that the presence of a large particle does not necessitate the presence of large pores.

3D characterisation of the pore structure also enabled the calculation of the permeability coefficient on the realistic description of the connected pore space. This information is compared to the estimations of permeability made by a pedo-transfer function (PTF) and other indirect estimations. We find that methods based on hydraulic radius and a percolation based calculation matched sample permeabilities. These were larger than values given by a method based on idealized periodic packings and a pedo-transfer function.

The relative permeability curves were simulated on the image and calculated using a PTF. The curves were compared and found to be very different. The differences are easily explained by comparing the model and the actual description of the void phase obtained from the image.

List of Acronyms and Symbols

α_i an empirically derived fitting parameter that relates the length of a pore calculated from spherical, ordered packed particles to that of a natural system allowing for particle shapes and sizes

ϕ porosity

ϕ_n porosity in number percent

ϕ_u Phi units

ρ density

ϕ_e effective porosity

ϕ porosity

2D two dimensional

3D three dimensional

APAC Australian Partnership for Advanced Computing

A&P the Arya and Paris pedo-transfer model for the calculation of permeability

ANU Australian National University

BSEM back scatter electon microscopy

CCD charge-coupled device

CK the Carman-Kozeny model for the calculation of permeability

CRT covering radius/sphere transform

CT computed tomography

c an empirical constant based on soil type and read from Table 3 given in Figure 2.15

D particle diameter

e void ratio of an undisturbed sample

EDT Euclidian distance map

FOV field of view

I length of the intermediate axis of a particle

K, k permeability

K_r relative permeabilty

LB Lattice-Boltzman calculation of permeabilty

$\mathbf{l}_c$ critical pore radius

L length of the long axis of a particle

LIS the long, intermediate and short axis respectively

LLS the laser light scattering technique for measuring particle size distribution

LRC the Loxton River core sample investigated in this thesis

MICP mercury injection capillary pressure (mercury porosimetry)

MPS maximum projection sphericity

NAPL non-aqueous phase liquid

n_i the equivalent number of spherical particles in the ith particle size fraction

N_i number of hypothetical scaled spherical particles required to trace the pore length of a tortuous natural pore structure of length contributed by n_i natural particles

OSC the first of the Ottawa sand samples investigated in this thesis

OSC2 the second of the Ottawa sand samples investigated in this thesis

P&L an equation derived for calculating permeability by Manmath Panda and Larry Lake

PSD particle size distribution

PTF pedo-transfer function

q_i flow rates of an individual saturated pore

Q_i volumetric flow rate

ROI region of interest

R_i mean particle radius for the ith particle size fraction

r_i pore radius associated with a discrete particle size fraction

S length of the short axis of a particle

S_w water saturation where w is water saturation percentage

SD sorting co-efficient

τ tortuosity

W_i the mass fraction of particles in the ith distribution

WRC water retention curve

x an empirical constant based on soil type and read from Table 3 given in Figure 2.15

Z co-ordination number

Contents

List of Figures

List of Tables

Part I

Introduction

Chapter 1

Measuring Physical and Hydraulic Properties of Porous materials

1.1 Introduction

The physical properties of soil and sedimentary materials are dependent on the shape, size and arrangement of the constituent particles. Our ability to measure and describe these properties is fundamental to understanding their behaviour (Feyen and Gorelick, 2005). The hydraulic properties of porous materials are of particular interest; saturated and unsaturated hydraulic conductivity (permeability) and water retention (capillary pressure), control the flux and storage of water (and contaminants) in the subsurface (Koltermann and Gorelick, 1996). This impacts on a range of applications. In an Australian context, understanding salt migration in soils is crucial to addressing the problem of dryland salinity and deteriorating water quality (Lawrie et al., 2000). The amelioration of salt-affected soils usually involves drainage techniques that aim to increase the flux of salt out of the soil. Permeability is one of the most important design parameters in estimating the stability of an underground excavation (Fillion and Moyer, 1996) earth fill (Ozcoban et al., 2007) and rock fill dams (Lee et al., 2005) and impacts on irrigation and drainage management (Kettle et al., 2007). In a global context, under-

standing contamination issues including virus and bacterial transport (Bradford and Bettahar, 2005; Keller and Sirivithayapakorn, 2004), radioactive waste disposal (Ophori, 1999; Ludwig et al., 2001) and non-aqueous phase liquid (NAPL) contamination and the implementation of effective remediation strategies (Eggleston, 2000; Meinardus et al., 2002) require fundamental understanding of the hydraulic properties of unconsolidated soils (Bradford et al., 2003; Feyen and Gorelick, 2005).

The primary controlling parameter in all these problems is the hydraulic conductivity / permeability parameter, or the relative ease with which a fluid flows through a porous material (Anderson, 1989; Koltermann and Gorelick, 1996; Eggleston and Rojstaczer, 1998; Ophori, 1999; Swartz et al., 2003). Direct methods of obtaining hydraulic conductivity are based on field pump tests; these tests are limited for practical situations due to unavailability of equipment, cost, time requirements and difficulty in operation. An alternative procedure is based on predicting the hydraulic properties from more easily and routinely available textural and structural soil properties. A range of approximate methodologies are used:

1.1.1 Empirical methods (Pedo-Transfer Functions):

Explicit formulation of the relationship between texture and hydraulic properties of soil are a challenge due to the very complex pore particle geometry (Kasteel et al., 2000; Pan et al., 2004). In soil science and many groundwater applications, pore-size distribution and hydraulic conductivity are commonly inferred from the particle size distribution (PSD) using pedo-transfer functions (PTF). These functions are constitutive relations between two or more soil properties that show a reasonably high level of statistical confidence; data available is correlated to the data required (McBratney et al., 2002). These functions commonly use the PSD as the primary input data (Anderson, 1989; Fredlund et al., 2000; Wösten et al., 2001; Eggleston and Rojstaczer, 2001). The output data required includes the pore-size distribution and the permeability or hydraulic conductivity under fully and partially saturated conditions.

A very popular method to correlate the PSD into hydraulic properties was

given by Arya and Paris (1981). In this method textural, mineralogical and organic matter content was used to predict hydraulic properties via multiple regression techniques. This method is highly cited; to date over 200 citations to this work have been made in the literature. The basis for this model is a similarity between the shapes of the PSD curve and the water retention (capillary pressure) curve.

1.1.2 Methods based on idealised periodic packings:

When uniform spheres are packed in systematic arrangements (e.g., cubic, orthorhombic, rhombohedral, tetragonal) the porosity of the packing varies from 30% to >40% (Graton and Fraser, 1935). For these idealised systems the sizes of the pores can be directly predicted from the grain size and the overall flow properties of the material accurately estimated. Berg (1970) extended this methodology to account for the sorting (deviation of a sediment from a monodisperse grain pack) and developed a semi-empirical equation which defined the flow properties of unconsolidated sediments with a range of grain sizes. Another method is based on a representative unit cell model (Duplessis and Masliyah, 1991); this particular model has been very successful in predicting flow properties of high porosity foam materials and granular sands.

1.1.3 Hydraulic radius models:

The simplest model for hydraulic permeability was proposed by Kozeny (1927) and modified by Carman (1937). This model (CK), one of the most widely accepted derivations of fluid permeability, is developed by comparing Darcy's law with the Hagen-Poiseuille law for slow laminar flow through a bundle of circular capillary tubes (Carrier, 2003; Hansen, 2004). Panda and Lake (1994) (P&L) modified the CK equation to media consisting of mixed particle sizes. This method has been shown to match permeability to the parameters of the particle size distribution for unconsolidated media.

1.1.4 Percolation-based models:

The effective hydraulic conductance of a system with a broad range of pore size is assumed to be controlled by the largest conductances which form percolating or spanning pathways across the sample. Katz and Thompson (1986, 1987) developed this approach to a description of the permeability of sedimentary rock arguing that permeability can be correlated to a critical pore diameter corresponding to the diameter of the smallest pore of the set of large pores that percolate through the rock. A feature of this method is that the critical pore diameter can be directly measured from capillary pressure experiments.

1.2 3D imaging and analysis of unconsolidated sediments

In reality, the hydraulic properties of unconsolidated sediments are a direct consequence of their complex micro-structure; (the term unconsolidated refers to the non-lithified or friable nature of the materials), and micro-structural attributes include the sizes and shapes of the constituent grain phase and the pores between the grains which define the porosity, pore and constriction size and shape, and ultimately permeability (Fiés and Bruand, 1998; Hilpert et al., 2003). Understanding these inter-relationships requires accurate description of the structure including inherent heterogeneities at the pore-scale in three dimensions (Bouma et al., 1977; Webster, 1994; Solymar and Fabricius, 1999; Tsakiroglou and Payatakes, 2000; Lin and Miller, 2004; Lehmann et al., 2006). This information has to date been generally unavailable (White and Sully, 1987; Sahimi, 1993; Ruan and Illangasekare, 1999; Kasteel et al., 2000; Pan et al., 2004; Li et al., 2007). The group at Applied Mathematics at ANU have developed a capability to characterise and predict hydraulic conductivity properties from experimental three dimensional (3D) images of sedimentary micro-structures. A micro-CT (CT) facility for imaging, visualising and evaluating sedimentary rock properties in 3D is used (Sakellariou et al., 2004a,b). Structural properties of the sediment including particle and pore sizes, shapes and interconnectivity can be

directly probed in 3D down to scales of a few microns. In addition, direct calculation of hydraulic conductivity properties can be undertaken on the digitized tomographic images. Initial comparisons with conventional laboratory measurements have been very promising (Arns et al., 2001, 2005a,b). The results have demonstrated the feasibility of combining digitized images with numerical calculations to predict structural and hydraulic properties.

In this thesis I undertake a comprehensive micro-CT study of four unconsolidated sedimentary samples; the samples include two samples of a homogenous model repacked sand sample, and 2 increasingly heterogeneous undisturbed sandy core samples from field studies in Australia and New Zealand. The samples were chosen in an attempt to cover a range of heterogeneity with the New Zealand sample representing a more difficult end member. The results of this study are compared to results obtained using traditional techniques.

Outcomes of the thesis include:

1.3 Outcomes

1.3.1 High quality 3D micro-CT data of unconsolidated sediments

A high-resolution, large-field x-ray micro-CT facility has been used to obtain the 3D structure of four unconsolidated sediment samples. Three of the four images, two Ottawa sand samples and a sandy sediment from an active river bed, can be considered of high image quality. In these three samples the x-ray attenuation data allowed unambiguous phase separation of the pore and mineral phase peaks. This enabled direct structural analysis of the pores and particles in detail. The fourth sample, Rotorua, was more difficult to analyse quantitatively.

1.3.2 Direct enumeration of the particle size statistics of the three samples in 3D.

Particle size descriptions of unconsolidated sediment are traditionally obtained by particle sieving and more recently laser light diffraction particle sizing. Textural characteristics are generally based on visual descriptions of representative particles and petrographic analysis of 2D thin sections. The classical methods have limitations in quantitatively describing the full 3D rock fabric. In this thesis I describe the 3D grain based characterisation of four samples from micro-tomographic imaging. Laser particle sizing and sieving are undertaken on the same samples and the data are directly compared. For the three homogenous samples the comparison of particle size from digital image data versus sieve data is good. For the fourth sample, limitations in resolving the clay phase and partitioning porous pumice particles from the digital image data leads to poorer comparisons. It is shown that the development of a grain partitioning methodology can give complimentary data to conventional petrographic techniques. A single image can yield over 50,000 grains per sample and from the full 3D image grain textural and fabric information can be directly generated. Measurements of particle sphericity, aspect ratio and particle connectivity are reported. Systematic shape changes with grain size can be directly noted. Grain connectivity is strongly dependent on the heterogeneity of the sediment with well sorted samples exhibiting significantly lower values. Limitations of the digital technique are also discussed.

1.3.3 Direct comparison of digital, laser diffraction and sieve methods of particle sizing:

Many studies have focused on the comparison of laser diffraction and sieve methods of particle sizing. The effect of particle non-sphericity has been noted and leads to important differences in the two measures. In particular, in a laser diffraction study of rod-like particles (Xu and Di Guida, 2003) it was reported that the measured particle size is heavily skewed towards the length of a particles longest axis due to the random orientation of the particle passing

through the light beam during the laser measurement. Eshel et al. (2004) notes that non-sphericity also affects the sieve measure due to non spherical particles ability to pass or be retained on a sieve of a given mesh size which is determined by the particles shape and ability to assume an orientation relative to the sieve that will allow it pass through. According to Matthews (1991) the coarser population is retained on the sieve and the smallest axes is measured. These findings are directly tested in this thesis: Digital analysis includes the measurement of the full distribution of the longest, intermediate and shortest grain axis on all 50,000+ grains within the image volume. These data are compared to sieve and laser diffraction studies on the same samples. In this thesis we explicitly show that sieve data corresponds well to the distribution of the short axis in particles and that laser light scattering data corresponds well to the longest particle axis. This is a direct verification of the results of Xu and Di Guida (2003); Matthews (1991).

1.3.4 Direct measurement of pore size information in 3D. Direct testing of particle-to-pore size correlations:

Using numerical methods for characterising pore bodies and constrictions via pore partitioning methods we directly enumerate in 3D the pore size, shape and interconnectivity of the four unconsolidated sediment samples. The image based derivation of pore size is directly compared to pore sizes derived from empirical methods; in particular the pore size distribution derived by the Arya and Paris (1981) PTF model (hereafter A&P). It is found that the largest pore sizes given by the empirical model are over an order of magnitude larger than found in the sample. This error is due to the assumption of a direct correlation between pore and particle size. The error in the assumption is directly enumerated from further 3D image analysis.

From the particle and pore partitioning one can directly test assumptions of different models; the A&P model, which assumes that particles and pore sizes correlate in contrast to Berg (1970), who assume little correlation between particles and pores. The pore size of all pores neighbouring a particle is enumerated and the resultant correlation plotted; we observe no correlation

between particle and pore size in any of the 4 samples studied.

1.3.5 Permeability estimation: Direct calculation versus empirical fits

Flow and transport processes in porous media depend on the geometric properties of their pores (Lehmann et al., 2006). The 3D characterisation of the pore structure at micron scale resolutions has made the direct calculation of permeability on the pore geometry of the connected pore space possible. This quantitative information can be compared to the estimations of permeability made by PTF calculations, packing, hydraulic radius and percolation models. We find that the hydraulic radius and percolation based models give the best estimate of K. The method based on packing consistently underestimates K by a factor of 3, while the PTF can differ by more than an order of magnitude.

1.3.6 Relative permeability: Direct calculation versus empirical fits:

The dependance of flow and transport processes on the geometric properties of the pore space is also critical in determining relative permeability (K_r) (Paterson et al., 1996; Rajaram et al., 1997; Valvatne et al., 2005). Calculation of K_r as a direct consequence of the geometry of the connected pore space is also now possible. These measures are compared to the estimations of K_r made by A&P. From the comparisons we find that A&P also performed badly in K_r estimation due to the simplified representation of pore space based on parallel tubes.

1.4 Outline

The outline of this thesis is as follows: Chapter 1 is an introduction to the range of concepts developed in this thesis. In Chapter 2 I describe the methods, apparatus, and theory applied to the study of hydraulic properties in porous media used in this study. In Chapters 3-5 I present the results of

the experimental measurements undertaken and 3D imaging studies of the 4 samples.

In Chapter 6 I review the thesis outcomes and discuss future directions for study.

Chapter 2

Methodology

This chapter describes the materials and methodologies utilised in this thesis. In Section 2.1 the samples and sampling procedures are described. Experimental procedures and apparatus are discussed in Section 2.2, and the specific calculations and measurement techniques are discussed from Section 5.3 onwards.

2.1 Samples

Four porous material systems were investigated in this thesis, they include 2 well sorted quartz grain packs (duplicates), an undisturbed river bed sediment and an undisturbed pumice sand.

2.1.1 Ottawa Sand

The first 2 systems studied are unground silica sand from the U.S. Silica Co® in Illinois, USA; Ottawa sand (product specifications are given in Section 3.1). Ottawa sand is a model granular material that is used extensively in the study of porous materials because it exhibits consistent properties across mineralogy, particle size, shape and sorting. It is used here to provide a model end member to the more heterogeneous natural samples. The material was acquired from the U.S. Silica Co® as a bag of silica sand that had been sourced and graded according to the company specifications given in Figure 3.1. From this we note that the constituent particles are entirely quartz in the

size range 200-600μm (diameter). An initial $20cm^3$ of this material was split into 2 samples and each was packed in a separate $17mm$ diameter Al tube, each with a volume of $7.39cm^3$. Packing was done by hand. A small amount was added to the tube ($\approx 1cc$), the tube was tapped to facilitate settling and then lightly pressed down with a small rod. This was repeated until the tube was filled. The 2 packs are named OSC and OSC2 and are essentially duplicate samples. The duplication is used to monitor the robustness of the investigative methods.

2.1.2 Loxton River Core (LRC)

The vibro-core retrieval method was used to retrieve a $65mm$ diameter core sample from an active river bed (Tan et al., 2006). This sample is examined in detail in Section 4. The vibro-core used a hydraulic vibration head mounted on top of a stainless steel barrel that vibrates into the saturated sediments. High frequency is used to cause local liquefaction of the sediment. As the sediment moves apart at the edges of the core, the weight of the core-rod(s) and head (spinning) pushes the drill rod into the sediment. A core catcher situated inside the core tube prevents the loss of materials when the drill rods are retrieved. When the drill rods are retrieved the material is extruded into a plastic sleeve using compressed air. The sample is then refrigerated to reduce organic contamination. Figure 4.1(a) is the $65mm$ diameter core sample removed and stored in a plastic sleeve. Further information about vibro-core retrieval is available at http://www.aquasurvey.com/Services/Vibracoring/Vibrocore_video/vibrocore_video.html.

The sample is a clean homogenous quartz sand, 80-95% quartz with up to 10% muscovite and <2% feldspar (Tan et al., 2006).

2.1.3 Rotorua

The sample from NZ was a shallow unconsolidated regolith sample from a coarse pumice sand aquifer (6.4-6.5m depth interval) in Rotorua, New Zealand, retrieved during a groundwater contaminant transport study. Acquisition in the field was via a $45mm$ diameter push tube sampler (Figure 2.1). This tool is used for obtaining undisturbed samples of soils which are

Figure 2.1: Extended nose of a push tube sampler.

not too hard to penetrate or contain too much gravel. The push-tube sampler was pushed into the undisturbed soil in one continuous, uniform motion without rotation. The soil which is displaced by the sampling tube is compressed into the surrounding soils (US Army Corps of Engineers, 2001). The sample was stored in a PVC tube and refrigerated. This sample is poorly sorted with particles of many mineralogies, shapes and sizes represented, including intragranular porosity, and is used in this study as an example of an end member material with extreme heterogeneities.

2.1.4 Subsampling for image analysis

The core samples retrieved from the field were cylindrical and $45mm$ (NZ pumice sand) and $65mm$ in diameter (LRC riverbed sample). These were stored and transported in rigid PVC tubes to minimise disturbance of the natural structure. A smaller cylindrical subsample of the original core maintaining the natural structure and bulk density was required for 3D image analysis. Extraction of this subsample from the original, larger, cylindrical sample (Figure 2.2(a)) was accomplished via smaller diameter aluminium tubes with $0.5mm$ thick walls (Figure 2.2(b)) inserted by means of a piston (Figure 2.2(c)). Sample size for imaging was $17mm$ diameter for the fine evenly textured materials, Ottawa sand and LRC to $35mm$ in diameter for the coarser grained material from NZ. The material immediatley surrounding the tube (delineated in red in Figure 2.2(a)) was saved and used to accommo-

date the multiple analytical techniques used in the study. When this extra material is used it is referred to as sister core material.

2.2 Experimental Characterisation

2.2.1 Microscopy

A microscopic examination of dried separated particles from sister core material was performed using a Leica® MZ 12 stereomicroscope fitted with a Nikon® Coolpix™ 8800 (8 megapixel) digital camera. From this investigation a qualitative description of particle texture and fabric was possible by visually comparing the images to reference figures and tables (see Sections 2.4 and 2.5).

2.2.2 Helium Pycnometry

Where density is reported a Helium pycnometer was used to determine solid volume. In this study we used an Accupyc™ 1330 pycnometer from Micromeritics® (http://www.micromeritics.com/products/accupyc_overview.aspx). This apparatus determines volume by measuring the pressure change caused by the addition of an object into a calibrated volume. Pycnometric measurement performed by this apparatus is considered the most accurate method of measuring absolute skeletal or true density. The procedure involves firstly oven drying the sample at 105C for a minimum 24 hours. This sample is then placed in a chamber of known volume which is then repeatedly evacuated and filled with He to remove moisture and air (purging). The pressure in this chamber is then measured. A reference chamber of known volume is then filled with He to a known pressure which is greater than the pressure in the sample chamber. A valve joining the 2 chambers is then opened and the pressure of the system allowed to equilibrate by the pressure in the sample chamber rising and the pressure in the reference chamber falling. The larger the volume of the sample in the sample chamber the higher the pressure in the equilibrated system volume (Figure 2.3). From the resultant pressure the

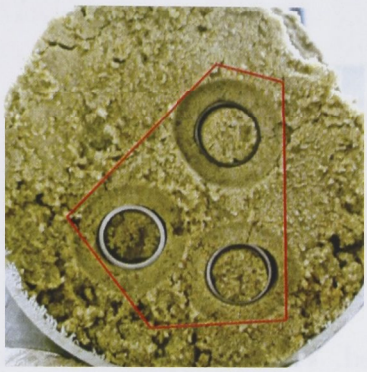

(a)

(b)

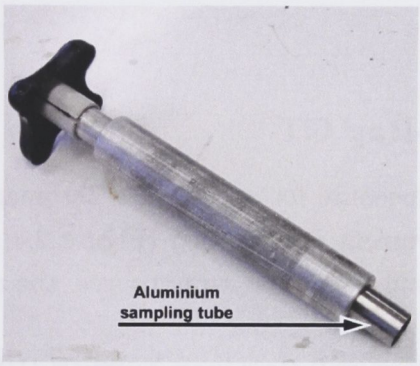

(c)

Figure 2.2: Subsampling of the original large diameter core samples recovered from the field. (a) 3 x 17mm Al tube samples and delineation of area for recovery of sister core material. (b) Removal of the Al tubes and sister core material from the original larger core. (c) Piston push rod for insertion of the Al subsampling tubes.

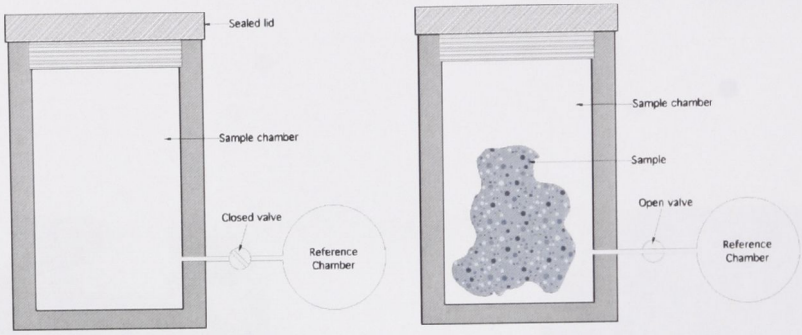

Figure 2.3: Helium pycnometer schematic. Sample chamber has a known volume. The reference chamber is filled to a known pressure. The chambers are connected and the pressure difference is measured.

skeletal solid volume of the sample is determined. Viana et al. (2002) give a complete overview of the Accupyc 1330 used in this investigation.

2.2.3 Micro X-Ray CT

In this section the procedure for acquiring a 3D image (tomogram) by the micro x-ray CT instrument is described (Figure 2.4(a)). The x-ray CT is composed of three main parts; the x-ray source, the rotation stage and the camera or CCD.

The x-ray source (Figure 2.4(a)) is an X-Tek^{TM} (UK) RTR-UF225/0 continuously pumped x-ray gun. It has high precision electron beam optics which produces a superior brilliance and fine focus of the x-ray beam. The electron beam can be set to a voltage of 225 kV (typical setting 80 kV) and a current of $2\mu A$ (typical setting $0.2\mu A$) and can be focussed down to a spot size of 2-5μm. The target is tungsten which generates polychromatic x-rays via bremsstrahlung.

The rotation stage is a Newport^{TM} RV120 which rotates the specimen during data collection and has a precision of 1 milli-degree.

The x-ray camera is a Roper^{TM} PI-SCX100:2048 which was specifically designed for the facility. Hermetically sealed behind a $0.5mm$ Be window, a

scintillator made from a $140\mu m$ thick CsI(Tl) hexagonal crystal with High Reflective coating is grown directly onto a tapered fibre optic bundle which efficiently channels the light directly onto a CCD for image formation. The CCD is a 2084×2084 pixel Grade 1, Kodak^{TM} KAF4302E and is Peltier cooled to -50 °C. The image is retrieved from the CCD with two 16-bit ADCs capable of 1 MegaPixel per second readout. The pixel pitch of the CCD is $24\mu m$ and coupled with a magnification of 1.4 in the tapered fibre optic bundle, the x-ray camera has an active area of $70\times70mm$. A detailed description of the instrument can be found in Sakellariou et al. (2004b); Sheppard et al. (2006).

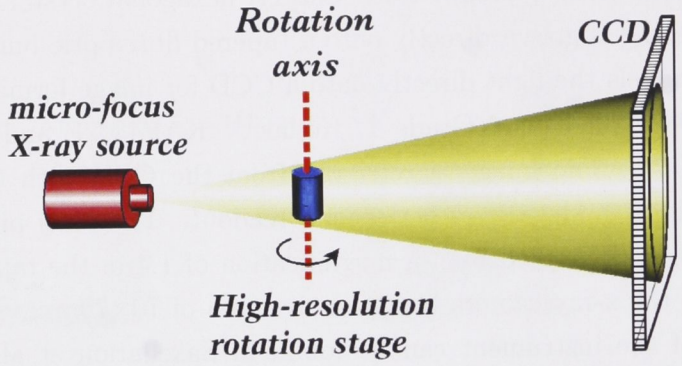

(a)

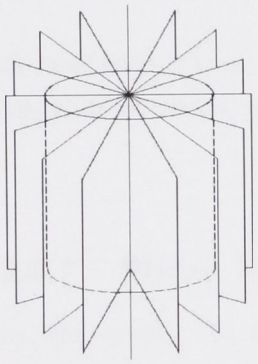

(b)

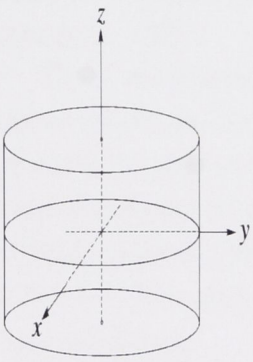

(c)

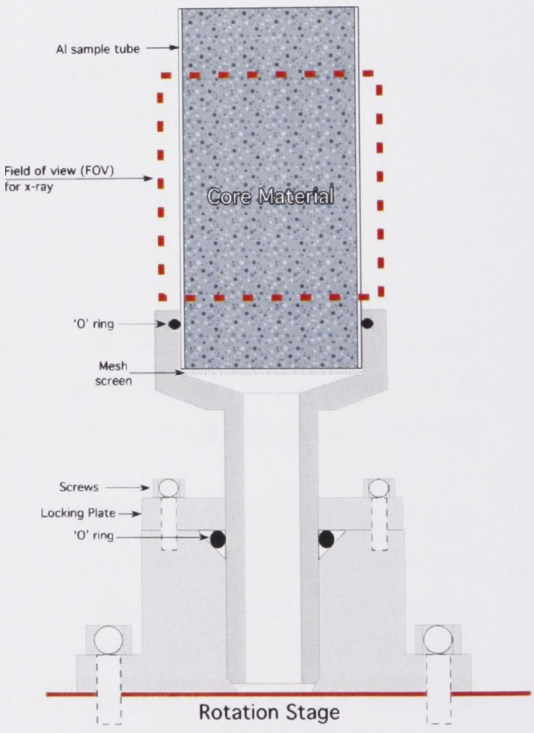

(d)

Figure 2.4: (a) Representation of the micro-CT operation. The object to be imaged incrementally rotates through 360^0 within the field of view made by the x-ray beam (yellow cone) and CCD. The angle of each individual movement within the 360^0 rotation is governed by the number of projections required to produce a tomogram of the desired voxel size. (b) As many as 3000 2 dimensional (2D) projections/radiographs are obtained (8 are shown here), one at each unique rotation angle. (c) Schematic of the x, y, and z directions when referring to tomographic data. (d) Sample arrangement for imaging showing the field of view.

2.2.3.1 Procedure

Acquiring a tomogram firstly involves placing the sample on the rotation stage at an appropriate distance between the source and camera to attain the required magnification. The sample must be accommodated within the field of view (FOV) such that there is free space on either side of the sample (Figure 2.4(a and d)). By moving the rotation stage closer to the CCD one can consider a large FOV ($60mm$ cross section with $30\mu m$ resolution) or by moving the sample closer to the source, high resolution images can be attained down to a $4mm$ cross section with $2\mu m$ resolution.

In this investigation the samples are constrained within an Al tube to maintain the structural integrity of the material. The Al tube is arranged in an attachment specially designed to eliminate sample movement and position the tube in the centre of the rotation stage within the FOV (Figure 2.4(d)).

2.2.3.2 Imaging

To obtain a tomographic image multiple radiographic projections are obtained. For each projection the sample is held stationary within the FOV and exposed to x-rays for an extended period (exposure time); 10-30 seconds is typical. Exposure time is adjusted to maximise the x-ray intensity of the beam reaching the CCD. This is a function of the energy of the x-rays leaving the source, by the type and thickness of the filter used to minimise beam hardening, and the distance between the source and CCD.

The x-ray intensity of the beam travelling through the sample from the source to the CCD over the exposure time period is recorded as a 2048^2 2D radiograph. The sample is then rotated 0.12^0 to the next stationary position and the process is repeated. 3000 2-D radiographs are acquired during a full 360^0 degree rotation of the sample; this process can take up to 36 hours and is strongly dependent upon source to camera distance; a shorter source to camera distance means a shorter exposure time per radiograph is required.

2.2.3.3 Reconstruction

The collection of 3000 radiographs are reconstructed into a 3D volume comprising numerous 3D volume elements (voxels) each with a characteristic attenuation value. This process is called the reconstruction phase. Reconstruction relies on two processes, a pre-processing step followed by a Feldkamp reconstruction step (Feldkamp et al., 1984). To generate a tomogram, the projection data are individually preprocessed to represent linear interactions between the specimen and the probe. Due to the use of a poly energetic x-ray beam at this facility, beam hardening artefacts are introduced into the tomogram, so the x-ray beam is pre-filtered to minimise it's energy spread. In this study a $3mm$ SiO_2 disc was used for all the imaging. Once the projection data are linearised, other steps follow to minimise artefacts in the tomogram that are the result of non-ideal aspects of the experiment. The resulting virtual plane adheres to the strict geometric requirements of the Feldkamp algorithm (a description of this process is recorded in detail in Sakellariou et al. (2004a); Sheppard et al. (2006)). All reconstructed data are processed on multiple processors at the Australian Partnership for Advanced Computing (APAC) National Facility at the Australian National University: a 2048^3 tomogram is generated in approximately 5 hours on 128 CPUs. An example of a resultant greyscale 2D slice obtained after reconstruction is shown in Figure 2.5(a).

2.2.3.4 Segmentation

Segmentation is the process of phase separating the image into discrete solid and void phases. This phase separation is required to characterise the particle and pore phases and for the analysis of transport properties. The reconstructed data (tomogram) consists of a large 3D array (>8 billion voxels) of x-ray attenuation coefficients. The x-ray intensity value at each voxel in the tomogram range from 0 to 65535 (Figure 2.5(a)). The first step in the process involves defining the fiducial volume (the image subvolume of interest) from the full 2048^3 tomogram. Voxels in the fiducial volume are then plotted in an x-ray attenuation histogram; an example for a clean sand (Figure 2.5(a)), is shown in Figure 2.5(b). Phase separation is straight forward on this sim-

ple sample. The binary histogram Figure 2.5(b) has two clear peaks, one corresponding to the void phase and one corresponding to the solid phase. Segmentation is therefore straight forward; one begins by defining absolute threshold values of $\leq$5100 for the pore phase and $\geq$7500 for the solid phase. Phase separation in the ambiguous intensity regions between these phases is then made using the converging active contours algorithm (Sheppard et al., 2004). A visual examination of the resulting binarised dataset (Figure 2.5(c)) verifies that the segmentation is realistic.

Figure 2.6(a) is a 2D cross section through a sample that does not exhibit a clean distinction between the solid and void phases. The sample exhibits an extensive porous clay fraction with particles below the image resolution. The clay rich regions exhibit an intermediate attenuation between those of the pore and solid (particle) phases. Initial approximation of the thresholds was $\leq$8000 for the pore phase and $\geq$12000 for the solid phase (Figure 2.6(b)). Phase separation in the ambiguous intensity regions between these phases was then made using the converging active contours algorithm. The resulting segmentation is presented in Figure 2.6(c). Porosity is calculated at this stage by counting the proportion of voxels labelled void. While the pore phase representation seems realistic, it is clearly difficult to unambiguously phase separate this image into pore and solid phases.

The segmentation stage of the process is obviously crucial to any subsequent analysis of the binarised dataset. The current methodology is dependent upon the operator choosing the best initial absolute threshold values from where the converging active contours algorithm begins. A test of the robustness of the analysis has been undertaken on a reservoir sandstone (Sheppard et al., 2005, 2006). A sample with 29% porosity was thresholded with 26% and 32% porosity; extreme examples deliberately chosen to lie beyond the range of normal variation. Despite the extreme variation in porosity little change in the particle size analysis and pore connectivity was observed. The porosity/permeability trends were consistent across the different samples.

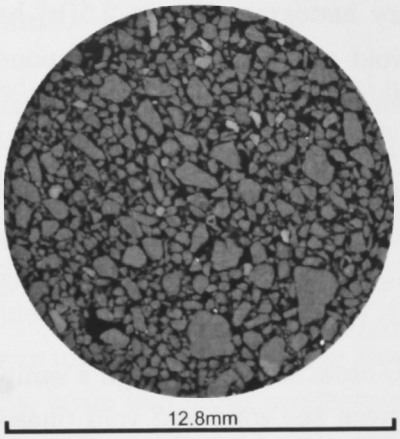

(a) Greyscale indicates x-ray intensity value.

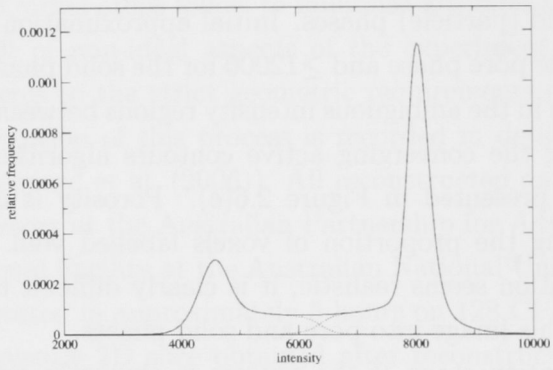

(b)

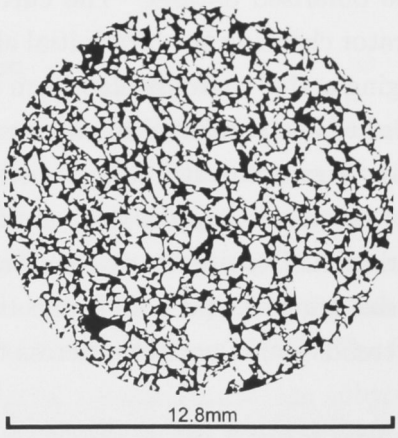

(c)

Figure 2.5: (a) Greyscale 2D slice through the 3D image of a clean quartz sand. (b) Histogram of x-ray attenution values for (a). The dotted line is the applied cutoff to binarise the dataset. (c) Resultant binarised image.

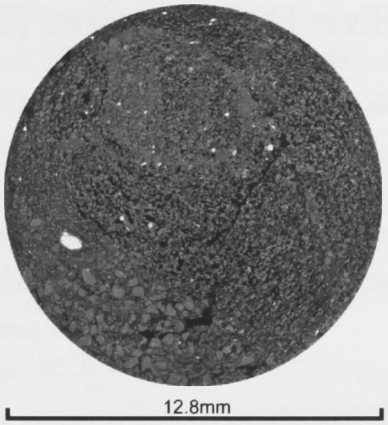

(a) Greyscale indicates x-ray intensity value.

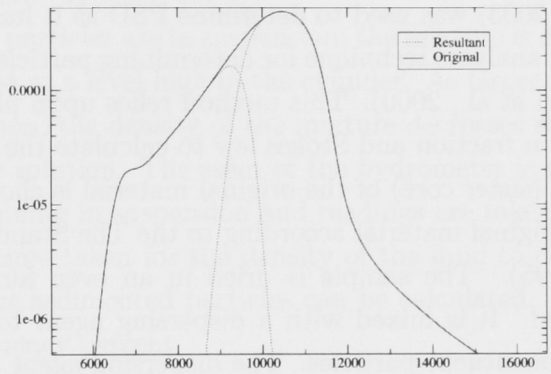

(b)

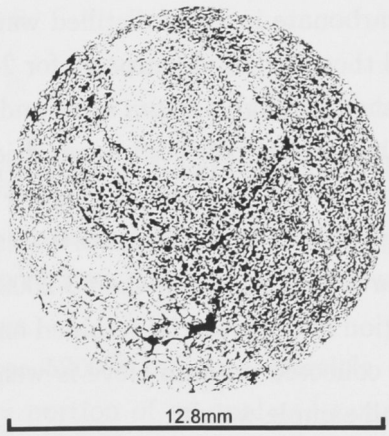

(c)

Figure 2.6: (a) Greyscale 2D slice through the 3D image of a sandy clay regolith sample. (b) Histogram of x-ray attenution values for (a). The dotted line is the applied cutoff to binarise the dataset. (c) Resultant binarised image.

2.3 Particle Size Distribution (PSD)

PSD has traditionally been measured using a set of nested sieves and a fluid density technique such as the pipette or hydrometer method. In recent years laser light scattering (LLS) has become a popular method to determine PSD in the $0.01\mu m$ - $1000\mu m$ range. In this thesis analysis of the 3D image has also been used to obtain the PSD. Here the methods used in this thesis are detailed.

2.3.1 Sieve Hydrometer

In this thesis the sieve-hydrometer method (The Standards Association of Australia, 1995, 2003) was used to determine PSD as it has found universal acceptance as an analyses technique for determining particle size distribution in soils (Fredlund et al., 2000). This method relies upon physical sieving to obtain the $>63\mu m$ fraction and Stokes law to calculate the $<63\mu m$ fraction.

A subsample (sister core) of the original material is chosen. It was separated from the original material according to the The Standards Association of Australia (1995). The sample is dried in an oven for 24 hrs at 105C and then weighed. It is mixed with a dispersing agent to facilitate disaggregation into constituent particles. The dispersing agent used is a sodium hexametaphosphate solution prepared by dissolving 33g of the salt with 7g of anhydrous sodium carbonate in 1L of distilled water. This mixture is left to stand for 1 hour and then stirred vigourously for 2-3 minutes in a blender. The sample is then washed through a $63\mu m$ sieve and the washings collected. The material left on the sieve is collected, oven dried, reweighed and then sieved through the nested sieves. The nested sieves (Figure 2.7(a)) have apertures graded according to the Udden-Wentworth scale (Figure 2.8). These are used to measure particle diameter in the 63-$2000\mu m$ range. Weights are recorded as the proportion of the material retained on a particular sieve. The weight of the material collected on each sieve is weighed and recorded as a proportion of the overall sample weight.

The washings containing the $<63\mu m$ fraction are then added to a 1L measuring cylinder at 20C and vigourously shaken. A hydrometer is suspended in the solution (Figure 2.7(b)) and readings taken from the stem at 0.5, 1,

2, and 4 minutes. The hydrometer is then removed rinsed and replaced to take readings at 8, 15, and 30 minutes, and 1, 2, and 4 hours, and then twice daily. The hydrometer (Figure 2.7(b)) measures the density of the soil/water mixture to determine the volume of sediment suspended in the water column. The scale records the g/ml of sediment in suspension when the reading is taken (The Standards Association of Australia, 2003). Stokes law is then invoked which states that heavier (larger, usually) particles sink faster than smaller particles when suspended in a liquid.

The equation is: $V = \frac{(2gr^2)(d_1 - d_2)}{9\mu}$ where V = velocity of fall (cm/sec^1), g = acceleration of gravity (cm/sec^2), r = "equivalent" radius of particle (cm), d_1 = density of particle (g/cm^3), d_2 = density of medium (g/cm^3), and μ = viscosity of medium $(dynesec/cm^2)$.

Initially most particles are in suspension; the mixture is dense and the hydrometer will float at a level high in the cylinder. As larger mineral particles fall from suspension, the density of the mixture decreases and the hydrometer sinks into the solution. The stem of the hydrometer is marked in grams of sediment remaining in suspension and readings are taken as a function of time. From the time taken for the density of the fluid to change the equivalent radius of the sedimented particles can be calculated. Data is returned as a volume frequency percent.

2.3.2 Static Laser Light Scattering (LLS)

Static laser light scattering using a Saturn DigiSizer 5200® operated by Particle & Surface Sciences™ Pty. Limited, Gosford was used to obtain LLS particle size distributions.

The Saturn DigiSizer 5200® measures particle diameter in the range $0.1\mu m$ to $1000\mu m$. Any portion of an analysed sample with a particle size greater than $1000\mu m$ is sieved on through nested sieves $3000\mu m$, 2800, 2000, 1600, 1000 and $850\mu m$; this is then incorporated into the overall distribution. Typically 0.5cc of material is used for the LLS analysis. According to

Figure 2.7: (a) Nested sieves graded according to the Udden-Wentworth scale. (b) Hydrometer for measuring mass of suspended sediment in a graduated measuring cylinder.

Australian Standard covering the use of laser diffraction methods to measure particle size (The Standards Association of Australia, 2000) the technique is based on the phenomenon that particles scatter light in all directions with an intensity pattern that is dependent on particle size; diffraction angle increases with decreasing particle size (McCave et al., 1986), assuming a spherical shape for all particles. Data reduction is accomplished using Mie theory calculations which extract the particle size information from the intensity characteristics of the scattering pattern (Jones, 2003). An overview of the process used at Particle & Surface Sciences Pty. Limited is available on their website at, http://www.pss.aus.net/products/micromeritics/equip_particle_size/5200/5200.html. The Australian standard covering this procedure is The Standards Association of Australia (2000). The LLS technique has been tested and compared to other techniques by many investigators including Loizeau et al. (1994), Buurman et al. (1997), Konert and Vandenberghe (1997), Beuselinck et al. (1998), Campbell (2003) and Eshel et al. (2004). From these studies we see that PSD is dependent upon the technique used; generally LLS overestimates particle size relative to sieving.

Millimeters	μm	Phi (ϕ)	Wentworth size class	
		-20		
4096		-12	Boulder (-8 to -12ϕ)	
1024		-10		
256		-8	Pebble (-6 to -8ϕ)	
64		-6		
16		-4	Pebble (-2 to -6ϕ)	Gravel
4		-2		
3.36		-1.75		
2.83		-1.50	Gravel	
2.38		-1.25		
2.00		-1.00		
1.68		-0.75		
1.41		-0.50	Very coarse sand	
1.19		-0.25		
1.00		-0.00		
0.84		0.25		
0.71		0.50	Coarse sand	
0.59		0.75		
1/2 0.50	500	1.00		
0.42	420	1.25		
0.35	350	1.50	Medium sand	Sand
0.30	300	1.75		
1/4 0.25	250	2.00		
0.210	210	2.25		
0.177	177	2.50	Fine sand	
0.149	149	2.75		
1/8 0.125	125	3.00		
0.105	105	3.25		
0.088	88	3.50	Very fine sand	
0.074	74	3.75		
1/16 0.0625	63	4.00		
0.0530	53	4.25		
0.0440	44	4.50	Coarse silt	
0.0370	37	4.75		
1/32 0.0310	31	5	Medium silt	
1/64 0.0156	15.6	6	Fine silt	
1/128 0.0078	7.8	7	Very fine silt	
1/256 0.0039	3.9	8		Mud
0.0020	2.0	9		
0.00098	0.98	10		
0.00049	0.49	11	Clay	
0.00024	0.24	12		
0.00012	0.12	13		
0.00006	0.06	14		

(a)

Figure 2.8: The Udden-Wentworth scale ($-\log_2$) is used to describe the particle size classes (Udden, 1898; Wentworth, 1922). Particle size data is given in phi units (ϕ_u) intervals, microns and millimeters. One phi unit is equal to one Udden-Wentworth grade and is computed by taking the negative log of the diameter in millimeters.

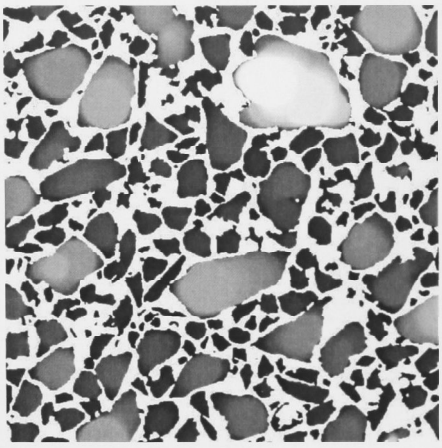

(a) Covering sphere transform in the solid phase. The greyscale indicates the CRT value at each voxel with dark to light indicating small to large radii.

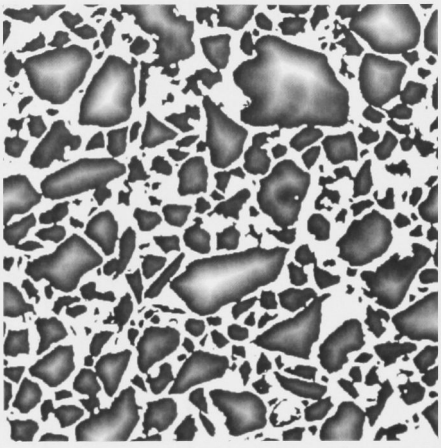

(b) Euclidian distance map in the solid phase showing the medial axis. The length associated with the EDT is smaller than the CRT.

Figure 2.9: Covering radius and euclidian distance transforms.

2.3.3 3D Image Analysis

In this section a short description of morphological image tools is given.

2.3.3.1 Covering Sphere Transform (CRT)

The CRT is a model free technique for defining feature size within a 3D image based on defining locally for every point within the structure, the diameter of the largest sphere which fully lies within an individual phase and covers that point. The corresponding radius of that sphere is referred to as the covering radius (Arns et al., 2005a). An example of the CRT map of the particle phase is given in Figure 2.9(a).

2.3.3.2 Euclidian Distance Map

The Euclidian distance (EDT) map defines for each voxel of the binarised image the distance to the nearest boundary voxel (Dougherty and Lotufo, 2003). Figure 2.9(b) shows the labelling results with the voxels furthest from the boundary brightest (Saadatfar et al., 2005).

2.3.4 Particle partitioning

Extracting the PSD from the 3D image uses a technique explained previously in detail by Sheppard et al. (2005, 2006), and Saadatfar et al. (2005). Essentially this method involves partitioning of the particle phase in the image via a watershed algorithm (Dougherty and Lotufo, 2003). Particle centres, which are used to seed the watershed algorithm, are identified by calculating the Euclidian distance and covering radius transforms. The EDT transform defines the distance from every voxel in the particle phase to the nearest particle/pore boundary. The particle centres are identified as those voxels that are maxima in the covering radius map. Each one of these voxels forms a seed that will grow into a single particle via a region growing algorithm based on the Euclidian distance map (Figure 2.10). Regions are then partitioned according to boundaries that coincide with constrictions of the grain space (Figure 2.10). An example of the results obtained using this process are presented in Figure 2.11(a, b). A typical tomogram yields more than 50,000 particles per image. It must be noted that the final number of particles does not include any particle that intersects the drawn fiducial boundaries. These particles are excluded from the distribution because they represent a portion of a particle only and are therefore of unknown size.

Once the partitioning process is concluded the volume of each particle is calculated and an equivalent spherical particle diameter ($D = \sqrt[3]{\frac{6V}{\pi}}$) assigned. From the diameter the volume of each particle was recomputed as a proportion of the overall granular volume and the particle size reported as a volume weighted particle size distribution.

The ability of the image analysis to resolve individual features within a given tomogram depends upon the voxel size of the dataset (See Section 2.2.3.1). Features smaller than $2 \times 2 \times 2$ voxels are unlikely to be resolved and thus a lower bound on particle identification is set by voxel size. At this scale individual particles may not be resolved as discrete features but may be merged into larger particles; identified as surface roughness. The particle network generated from this partitioning is presented in Figure 2.11(c).

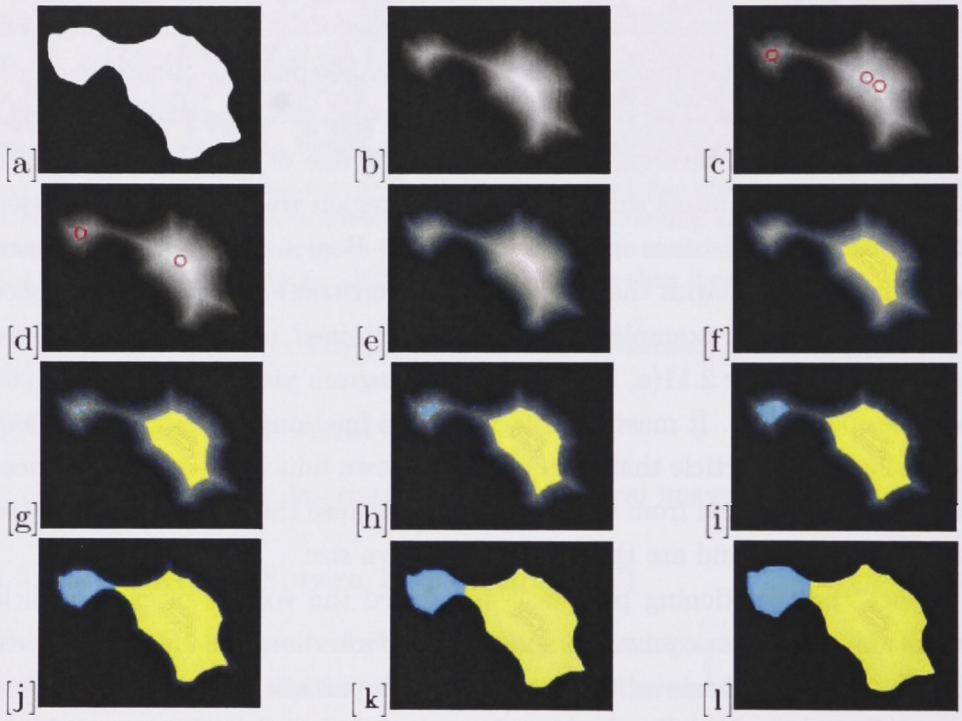

Figure 2.10: (a) Solid phase in the binarised image. Euclidian distance map of the solid phase (a larger example is presented in Figure 2.3.3.2) (c-d) maxima identification and merging of duplicates. (e) Contouring the Euclidian distance map. (e-l) region growing to identify individual particles from the binary image (after Saadatfar, 2007).

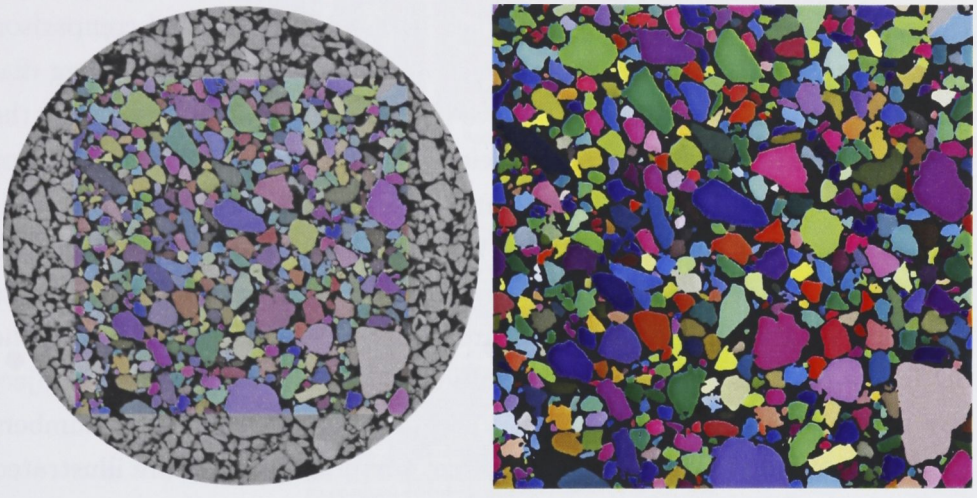

(a) (b)

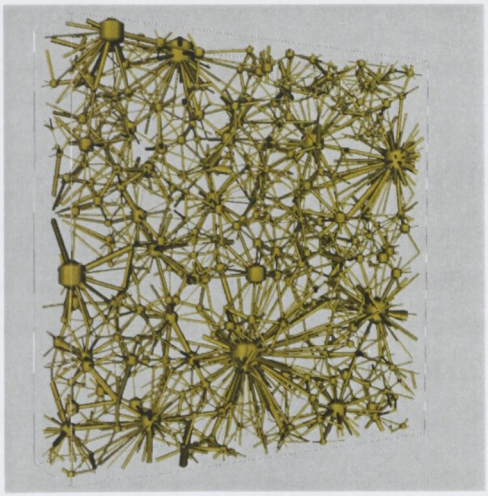

(c)

Figure 2.11: (a) A 2D slice through the 3D fiducial volume of an unconsolidated sandpack with labelled grains coloured. (b) A subsection of the particle phase partitioning. (c) Particle network. Spheres are particle centres and sticks are adjoining particles.

2.4 Texture

Textural analysis is a description of the shape and interrelationship of individual particles and is generally obtained by a subjective visual comparison of a subset of particles to standards such as the Powers plot and Zingg diagrams (see Figure 2.12). A quantitative result from manually measuring the 3 major axes of every individual particle is possible, such as those performed by Sneed and Folk (1958) who measured 1200 particles in the 32-64mm diameter range and Krumbein (1941) who advocated measuring at least 25 pebbles (16-32mm in diameter) for meaningful statistics; the requirements to undertake this method however, are prohibitive. Direct analysis of the 3D image removes the time constraints of a manual study and its subjective nature. Moreover direct analysis is capable of analysing large numbers (>50,000) of individual particles. Different textural measures are illustrated in Fig 2.12. Sphericity, sorting, the Zingg ratio and co-ordination number were all calculated directly from the partitioned 3D images.

2.4.1 Sphericity

This parameter is defined as the degree to which the shape of an individual particle approaches the shape of a sphere. It is most often determined by comparison to a chart of reference images such as that constructed by Powers (1953) (see Figure 2.12a).

Wadell (1932, 1933, 1935) quantitatively described degree of sphericity as

$$\Psi = \frac{\delta}{\Delta} \tag{2.1}$$

where δ is the diameter of a circle which has an area equal to the area of the largest projection of the grain, and Δ is the diameter of the smallest circle that will circumscribe the grain projection, and later

$$\Psi = \sqrt[3]{\frac{V_p}{V_{cs}}} \tag{2.2}$$

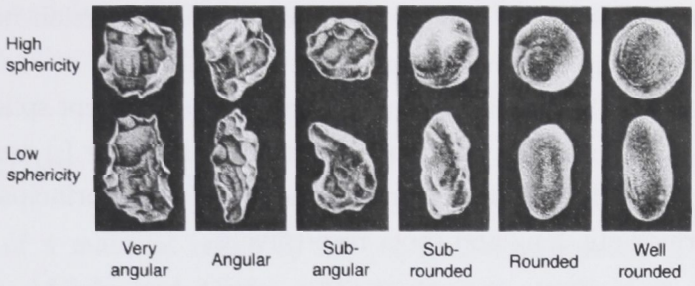

(a) Powers Plot for presenting the roundness sphericity parameters (reproduced from Powers 1953).

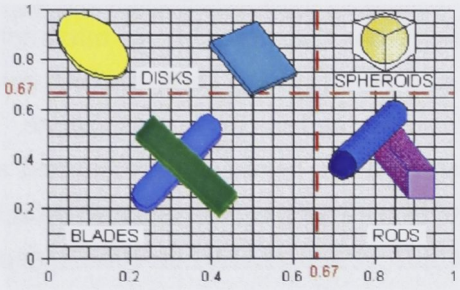

(b) Grain shape. x axis is breadth/length and the y axis is thickness/breadth (after Zingg 1935).

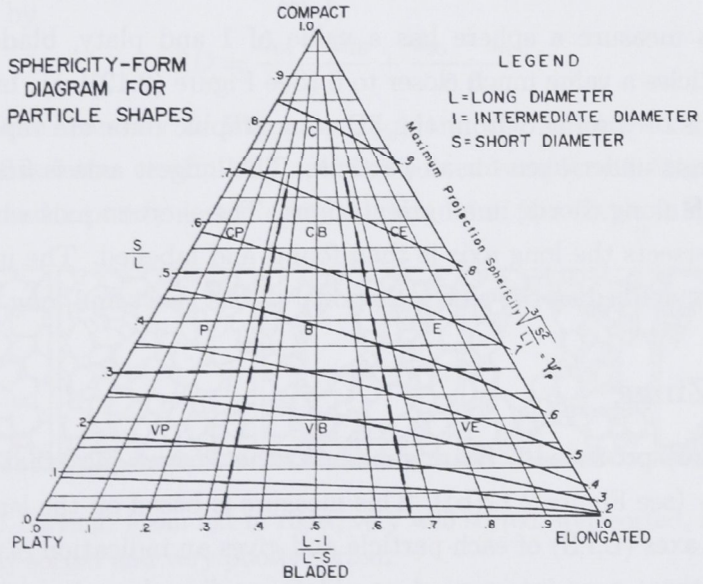

(c) Sphericity-Form Diagram (reproduced from Sneed and Folk 1958). C is compact or very spherical, P is platy, B is bladed and E is elongate. V signifies very.

Figure 2.12: Textural measures.

where V_p = volume of the particle as measured by immersion in water and V_{cs} = volume of the circumscribing sphere (Wadell, 1935).

Krumbein (1941) used the 3 principal axes in his intercept sphericity measure where the volume of a circumscribed sphere (diameter L) was compared to the volume of the ellipsoid characterised by all three principal axes I, L, and S, intermediate, long and short respectively

$$\Psi = \sqrt[3]{\frac{IS}{L^2}} \tag{2.3}$$

The concept of sphericity was also described as maximum projection sphericity (MPS) by Sneed and Folk (1958). These authors manually measured the principal axes of pebbles in the tens of *mm* size range. They improved upon the ratio idea and assumed the particle approximated a triaxial ellipsoid by using measurements of the 3 principal axes and included a maximum projection area (the product of L and I) to describe how a particle behaves in water,

$$\Psi_p = \sqrt[3]{\frac{S^2}{LI}} \tag{2.4}$$

Using this measure a sphere has a value of 1 and platy, bladed or elongated particles a value much closer to 0 (See Figure (2.12)(c)). In this thesis calculations of the MPS from the 3D tomographic data are reported. The calculation is undertaken for all particles; The longest axis is first identified by a search along chords in all orientations. The shortest axis which orthogonally intersects the long axis is then found and labelled. The intermediate axis is that defined as the axis orthogonal to the short and long.

2.4.2 Zingg

Zingg (1935) produced a chart similar to the Powers plot that dealt with shape only (see Figure 2.12(b)). This measure is based on the lengths of the 3 primary axes (L,I,S) of each particle and gives an indication of the relative length of these axes interpreted as oblate or disc shaped, equant (sphere or cube like), bladed or prolate, and rod shaped particles. This description provides a shape classification by plotting the ratio of the intermediate to long

axis of the particle (ordinate), against the ratio of the short to intermediate particle axis (abscissa).

2.5 Fabric

The fabric of a material refers to the physical arrangement of aggregates and particles (Allaby and Allaby, 1999; Blatt et al., 1972), such as counting the number of contacts a particle may have with neighbouring particles (co-ordination number) and the ratio of smallest to largest particle diameter or the sorting coefficient.

2.5.1 Sorting

Sorting of a sediment is an expression of the range over which the constituent particle diameters range (Allaby and Allaby, 1999). Figure 2.13 is an illustration of particle sorting ranging from very well sorted to very poorly sorted. Sorting as derived from the PSD statistics are expressed as the standard deviation (SD) of the distribution according to Folk and Ward (1957) and is determined by

$$SD = \frac{d_{84} - d_{16}}{4} + \frac{d_{95} - d_5}{6.6} \tag{2.5}$$

where d is the diameter in Phi units (ϕ_u) and the subscript refers to the percentile (Saadatfar et al., 2005). A well sorted sample will therefore have a small SD and a poorly sorted sample a large one (see Table 2.1).

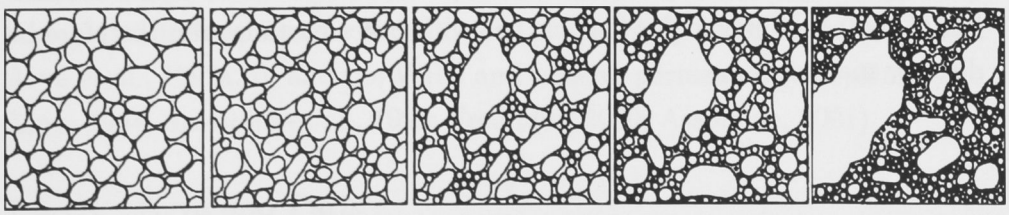

Figure 2.13: Sorting. From left to right, very well sorted, well sorted, moderately sorted, poorly sorted and very poorly sorted.

SD	
0.00 - $0.35\phi_u$	very well sorted
0.35 - $0.50\phi_u$	well sorted
0.50 - $0.71\phi_u$	moderately well sorted
0.71 - $1.00\phi_u$	moderately sorted
1.00 - $2.00\phi_u$	poorly sorted
2.00 - $4.00\phi_u$	very poorly sorted
4.00 - $\infty\phi_u$	extremely poorly sorted

Table 2.1: SD in Phi values as a description of sorting.

2.5.2 Co-ordination number (Z)

The co-ordination number refers to the number of contacts a particular particle has with neighbouring particles or number of touching neighbours per particle (Blouwolff and Fraden, 2006). Since this parameter is not directly measurable from a single planar cross section and needs to be measured from a 3D model (Bernal and Mason, 1960; Fauzi et al., 2002), it is well suited to the image analysis techniques employed here.

Z gives an indication of the sorting and packing characteristics of a sample. For example a very large particle in a matrix of small particles would exhibit particles with a large Z and a broad distribution of particle connectivity (see Figure 2.13 extreme right). In contrast a packing of similar sized particles would have a consistent Z distribution and few extreme values of Z (Figure 2.13 extreme left). All particle contacts in 3D within the full volume are identifiable once the particle identification process is complete. The number of contacts a particular particle has with other particles can therefore be directly measured.

2.6 Pore Size Distribution

Flow and transport properties of granular materials (e.g. porosity/permeability relationships) depend primarily on the pore size distribution of the material (Hilfer, 1993; Assouline and Rouault, 1997; Assouline, 2001).

This parameter is experimentaly obtained by draining a wet core at successively increasing suctions up to a pressure of 3 bars. The sample is weighed at each successively increased pressure to determine the moisture content at each pressure. Special care needs to be taken to avoid distortion of the wet core. The radius of the largest equivalent cylindrical pore remaining filled with water at a particular applied pressure is recorded. The water retention curve (WRC) then relates water content and pressure as described by (Loveday, 1974). This procedure erroneously asssumes that soil pores are equivalent to a bundle of capillary tubes with continuous variation in diameter. Another problem with this technique is the hysteretic nature of the measure where the curve follows different paths depending upon the drying and wetting history of the soil (Hillel, 1971).

In this thesis the pore size distribution is derived empirically from particle size information and via direct analysis of 3D images.

2.6.1 Pedo-Transfer Functions

Pedo-Transfer Functions (PTF) are constitutive relations between two or more soil properties that show a reasonably high level of statistical confidence. They commonly use the particle size distribution as the primary variable to derive pore-size distribution, permeability (Arya and Paris, 1981; Arya et al., 1999a,b), and the WRC and relative permeability (Fredlund and Xing, 1994; Smettem et al., 1999; Fredlund, 2000; Assouline, 2001).

2.6.1.1 Arya and Paris

One of the more widely applied PTF that derives pore size distribution and permeability from PSD is known as the Arya and Paris model (hereafter A&P)(Arya and Paris, 1981; Arya et al., 1999a,b). This model has over 200 citations in the literature; two recent examples are (Vaz et al., 2005;

Chakraborty et al., 2006). This model is based on the observation of similarities between the shape of the particle-size distribution and the experimentally measured WRC.

Using this model the pore-radius (r_i) associated with each discrete particle size fraction is calculated from the PSD and defined according to Arya and Paris (1981);

$$r_i = 0.816 R_i \sqrt{e n_i^{(1-\alpha_i)}} \tag{2.6}$$

where the R_i is the mean particle radius for the ith particle size fraction. e is the void ratio of the undisturbed sample given by the density relationship;

$$e = (\rho_{Particle} - \rho_{Bulk})/\rho_{Bulk} \tag{2.7}$$

where $\rho_{Particle}$ is particle density and is ρ_{Bulk} bulk density. n_i is the equivalent number of spherical particles in the ith particle size fraction;

$$n_i = \frac{3W_i}{4\pi\rho_{Particle}R_i^3}$$

where W_i is the mass fraction of particles in the ith distribution. α_i is an empirically derived fitting parameter that relates the length of a pore calculated from spherical, ordered packed particles (see Figure 2.14) to that of a natural system allowing for particle shapes and sizes. This parameter varies with soil type and is estimated at 1.38 from experimental WRC's (Arya and Paris, 1981).

This model defines a representative pore radius corresponding to each particle-size fraction of the PSD (Arya and Paris, 1981). The PSD is divided into fractions and then reassembled with each size fraction in a discrete domain preserving the ρ_{Bulk} of the natural sample (see Figure 2.14)). The pore volume assumed to be associated with each discrete size fraction is then computed from the $\rho_{Particle}$, void ratio (equation 2.7) and mass of each fraction. Particles are assumed to be spherical and the pores parallel cylindrical tubes. The empirical parameter α_i used in equation 2.6, initially taken to be 1.38, was redefined by Arya et al. (1999b), to allow particles to contribute to pore length in more than one dimension. This led to $\alpha_i = logN_i/logn_i$, where N_i

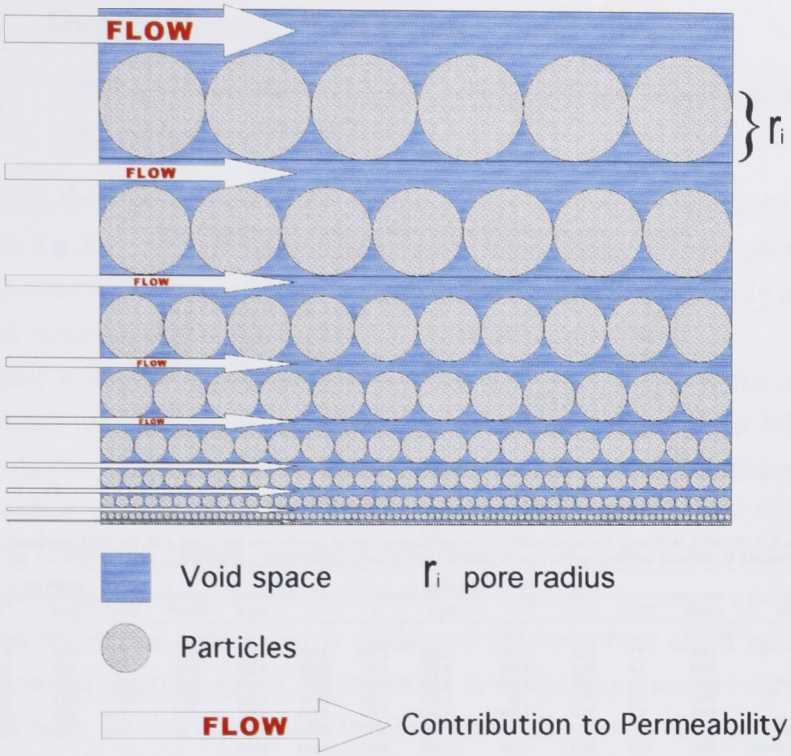

(a)

Figure 2.14: Schematic of the sorting described in the Arya and Paris Model ((Arya and Paris, 1981; Arya et al., 1999b)).

is the number of hypothetical scaled spherical particles required to trace the pore length of a tortuous natural pore structure of length contributed by n_i natural particles;

$$logN_i = a + blog(w_i/R_i)$$

where a and b allow the relationship $\alpha_i = logN_i/logn_i$ to approximate experimental WRC's measured for specific textural classes (see Figure 2.15), (details can be found in Arya et al. (1999b)). The redefinition of α_i by Arya et al. (1999b), is used in this study except where it causes large errors.

Table 2. Parameters of Eq. [10] relating log N_i to log(w_i/R_i^3), and the goodness of fit, r^2, for four soil textural classes.†

Textural class	Soils	Data pairs	a	b	r^2
Sand	6	62	−2.478	1.490	0.882
Sandy loam	6	75	−3.398	1.773	0.952
Loam	4	50	−1.681	1.395	0.936
Clay	5	88	−2.600	1.305	0.954

† cf. Arya et al., 1999.

(a)

Table 3. UNSODA soils used for model calibration and testing, model parameters log c and x in Eq. [19], goodness of fit, r^2, shape factor log S, and root mean square residuals (RMSR) of log-transformed $K(\theta)_{calc.}$ and $K(\theta)_{meas}$ data.

	Model calibration								Model test				
Texture	Code†	Clay	Sand	ρ_b	log c	x	r^2	log S	Code†	Clay	Sand	ρ_b	RMSR
		—— % ——		g cm^{-3}						—— % ——		g cm^{-3}	
Sand	1050	3.2	92.2	1.600	2.590	4.714	0.978	2.949	4000	1.5	93.8	1.460	0.669
	4650	1.0	94.0	1.622	2.507	4.471	0.970	3.032	1063	4.0	93.0	1.550	0.638
	4661	3.0	92.9	1.490	2.226	4.095	0.883	3.313	1043	3.0	93.0	1.593	1.603
	1464	2.4	93.0	1.67	0.171	2.808	0.963	5.368	4171	11.7	65.1	1.480	0.616
	1061	4.0	91.0	1.590	1.642	3.718	0.916	3.897	1054	2.5	97.2	1.540	1.563
Average					1.849	3.999	0.913	3.690					1.000
Sandy loam	1381	11.0	61.2	1.730	−0.952	3.000	0.977	6.491					
	1130	7.0	71.0	1.560	−0.808	2.882	0.981	6.347					
	4160	11.2	66.3	1.700	−2.426	2.664	0.972	7.965					
	4162	19.4	65.0	1.520	0.231	3.351	0.987	5.308					
Average					−0.871	3.063	0.964	6.410					
Loam	3192	16.3	44.2	1.440	2.392	4.139	0.996	3.147	2531	15.7	41.0	1.461	0.592
	4102	18.3	40.0	1.530	2.647	4.072	0.965	2.891	1370	25.9	46.0	0.950	1.719
	4610	24.0	39.0	1.110	−0.766	3.413	0.999	6.305	4600	24.0	39.0	1.040	1.155
	4101	16.3	41.6	1.500	2.780	4.344	0.976	2.759	2530	22.6	45.0	1.361	0.638
									4620	24.0	39.0	1.210	1.397
									3190	16.5	47.9	1.410	0.657
Average					2.647	4.258	0.972	2.892					0.996
Clay	4681	11.6	54.4	1.080	−0.226	3.625	0.969	5.765	2361	3.5	57.0	1.387	0.516
	4121	7.2	53.2	1.110	−1.203	3.227	0.997	6.742	1400	4.7	58.0	1.450	0.487
	2360	20.5	45.0	1.420	−0.262	3.531	0.986	5.801	4680	13.8	47.3	1.100	1.065
									4120	11.8	50.8	1.240	0.549
									2362	3.8	63.0	1.250	0.542
Average					−0.488	3.506	0.976	6.027					0.670
Average for all textures					0.482	3.602	0.938	5.507					0.878

† UNSODA code.
‡ Bulk density.

2.15

(b)

Figure 2.15: (a) Table 2 reproduced from Arya et al. (1999a). Parameters a and b are chosen from this table according to textural class from PSD (percent sand and clay). (b) Table 3 reproduced from Arya et al. (1999a). log c and the x parameter are also chosen according to the sample texture (percentage sand, silt and clay).

2.6.2 Image Based Pore Sizes

2.6.2.1 CRT and Numerical Mercury Injection Capillary Pressure Experiment (MICP)

Following the binarisation of the image during the segmentation stage (recall Section 2.2.3.4) numerical analysis of the flow and structural properties of the 3D structure becomes possible. The CRT (see Section 2.3.3.1) is the first natural measure of the pore size of a 3D digital image.

Using a similar technique to the covering radius transform an MICP simulation can be performed directly on voxelated images. In MICP at a fixed capillary pressure (pore entry radius) all the accessible throats which have radius greater than or equal to the equivalent pore entry radius are invaded (Figure 2.16(a)). Starting with the largest sphere and incrementing the sphere radius downwards (incrementing capillary pressure upwards), the non-wetting phase saturation is measured as the subset of all spheres that have invaded the pore space. This results in a capillary pressure curve for the imaged core. In this simulation invasion from all sides is used as the boundary condition and can be compared to a mercury porosimetry experiment, where all outside faces are connected to the non-wetting phase as shown in Figure 2.16(b). Saturation versus pore entry radius is reported. In Figure 2.17 we show an example where numerical MICP matched experimental data on the same rock material (Bauget et al., 2005b).

2.6.2.2 Network analysis / Pore partitioning

The generation of the network structure used here is based on the EDT (recall Section 2.3.3.2), with pore space geometry and topological information extracted mathematically from the tomogram (Sheppard et al., 2005). From the Euclidian distance map and a homotopic thinning algorithm a medial axis is generated. The pore body region centres could then be identified and a network of junctions and links formed. A watershed transform is then

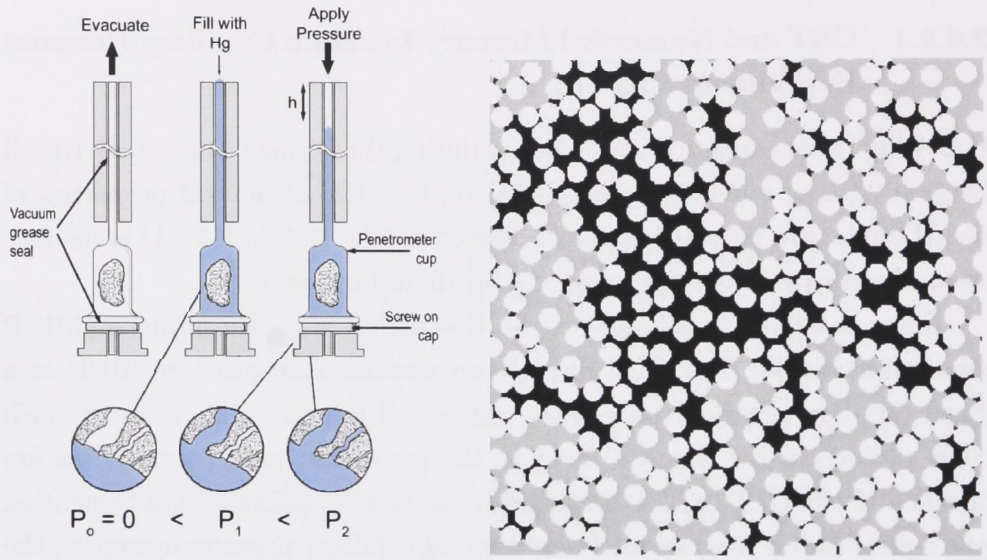

Figure 2.16: (a) Schematic of the Hg injection process. Hg is blue. (b) Simulation of mercury injection into a model porous medium. Mercury is invading from all sides. Gray denotes intruded mercury (after Garboczi and Bentz, 1991). Note the large amount of pore space shielded from invasion by small radii constrictions.

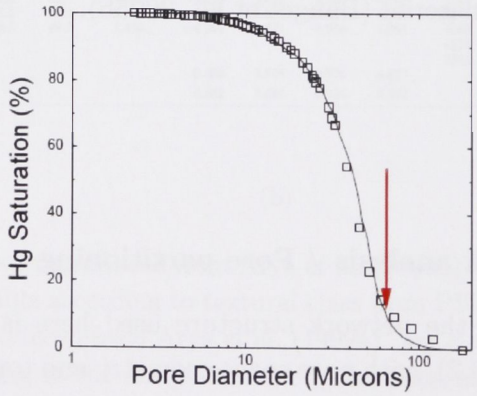

Figure 2.17: Experimental and simulated MICP curves closely match. Data is from a sandstone. The inflection point (indicated by the red arrow) referred to by Katz and Thompson (1986) can be read from this curve at approximately $65\mu m$.

applied to the remaining region centres to full identify each region, thereby partitioning the full pore space (Figure 2.18(a)). A region merging algorithm was then used to simplify the network (Figure 2.18(b)). Throats were then assigned a portion of the volume in each pore (Sheppard et al., 2006).

Figure 2.18(a) shows a 2D slice through the partitioned volume. Figure 2.18(b) is a completed pore throat network for a simple sandstone. Most resultant pore networks from images are made up of approximately 100,000 pores and 200,000 throats. Figure 2.18(c) is the pore throat distribution percentage of pore volume vs pore radius. The volume percentage values are given as percentages of the pore or throat volume and not of the entire void volume.

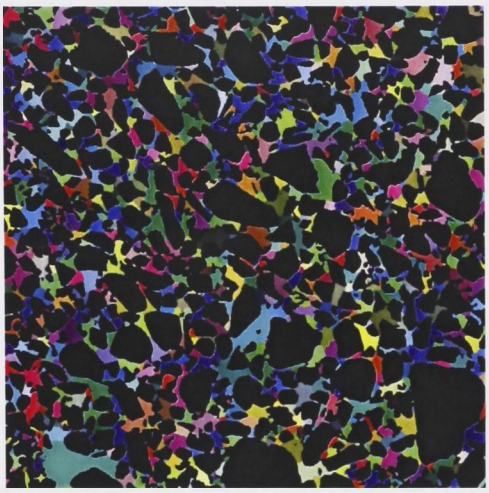

(a) 2D slice through the 3D pore/throat partition of an unconsolidated sandpack.

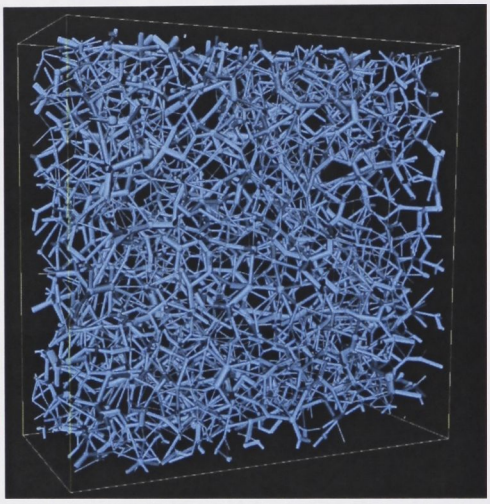

(b) Pore/throat network of an unconsolidated sandpack.

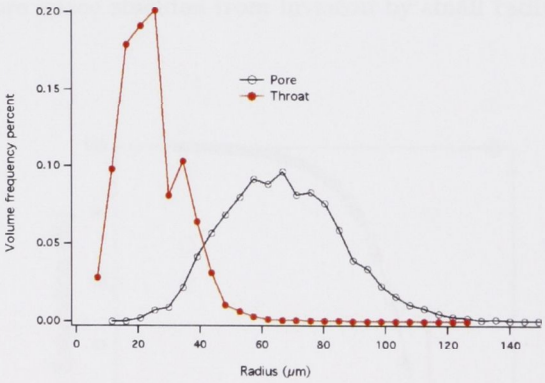

(c) Pore/throat distribution of an unconsolidated sandpack.

Figure 2.18: Pore network of a sand pack from analysis of a 3D image.

2.7 Permeability (K)

2.7.1 K from Empirical correlations

2.7.1.1 Arya and Paris (1981) and Arya et. al. (1999b)

Arya and Paris model the pore space as i families of pores associated with varying particle sizes. From each family the volumetric flow rate (Q_i) can be written as the sum of the flow rates of individual saturated pores (q_i) within the ith pore fraction of a particular soil sample (Arya et al., 1999a). In Arya and Paris each pore is assumed to be an equivalent capillary tube and the flow rate (q_i) is calculated as a function of pore radius (r_i). The heterogeneous distribution of pores, pore shape, tortuosity, connectivity, fluid properties and saturation are expressed as a single empirical variable cr_i^x, where c and x are empirical constants based on soil type and read from the tables given in Figure 2.15. r_i was previously calculated according to equation 2.6 from the PSD and packing characteristics.

The hydraulic conductivity value (K) is then the sum of all the flow rates calculated for each individual pore,

$$K = \frac{c\phi_e}{\pi} \sum_{i=1}^{n} R_i^{(x-2)} w_i [0.667 e n_i^{(1-\alpha_i)}]^{(x-2)/2} \qquad (2.8)$$

(Arya et al., 1999a).

The effective porosity is $\phi_e = S_{water}[1 - (\rho_{Bulk} - \rho_{Particle})]$ and e is again the void ratio from equation 2.7. Hydraulic conductivity is calculated for each particle fraction and summed to give absolute saturated K. Details of this algorithm can be found in Arya et al. (1999a).

2.7.1.2 Berg (1970)

Berg (1970) showed that the K of cubic, orthorhombic and tetragonal packing is well described by

$$K = 5.1 * 10^{-6} {\phi_n}^{5.1} D^2 \tag{2.9}$$

where ϕ_n is porosity in number percent and D is the particle diameter given in mm. Berg then approached the problem of real sediments and addressed the problem of sorting. Sorting is the measure of deviation from a median diameter. Berg noted that for permeability the smaller particles are more significant because they result in smaller pores and thus lower K. In contrast to the model of A&P, Berg noted that small particles are distributed at random within the population. This leads to a reduced pore size which will impede flow regardless of the number of larger pores randomly distributed. He argues that K is controlled by a dominant small pore size because in a random array of particles, large pores alternate with smaller pores and the smaller pores are the key to the permeability; they offer the greatest resistance to flow. This is exactly the opposite to the model of A&P where it is assumed that different particle sizes aggregate into parallel families of flow paths and therefore, when large and small pores exist in an aggregate the large pores will control the flow capacity. Berg assumes that the K of an unconsolidated sediment is controlled by a pore size determined by the particle size of the 90th percentile in the distribution. He also combined the effects of packing, particle size, sorting and particle shape, giving a general expression for K

$$K = 5.1 * 10^{-6} \phi_n^{5.1} D^2 e^{(-1.385 Pd_{\phi u})} \tag{2.10}$$

where $Pd_{\phi u} = \frac{P_{10} - P_{90}}{z}$ is defined as the percentile deviation of the PSD in phi units.

2.7.1.3 Panda and Lake (1994)

Panda and Lake (1994) proposed a method based on the Carmen-Kozeny model (Carman, 1937). Using the Hagen-Poiseuille law, the permeability for steady laminar flow in a uniform, smooth walled tube of radius R is

$$k = R^2/8$$

If we equate the travel time from one end of the tube to the other to the travel time across a permeable medium of equivalent length we arrive at

$$k = R^2\phi/8\tau \tag{2.11}$$

where ϕ is the porosity and τ is the tortuosity of the medium. Since, in a realistic permeable medium it is impossible to define a representative radius, R is often replaced by the hydraulic radius, defined as

$$R_h = \frac{volume\,open\,to\,flow}{wetted\,surface\,area}$$

For flow in a tube, $R_h = R/2$ using the definition of porosity, this becomes

$$R_h = \frac{\phi}{a_v(1-\phi)}$$

where a_v is the specific internal surface area of the medium (ratio of exposed surface area to solid volume), an intrinsic permeable media property. Substituting this into equation 2.11 we obtain,

$$k = \frac{\phi^3}{2\tau(1-\phi)^2 a_v^2} \tag{2.12}$$

For the special case of an assembly of single size spheres of diameter D_p, $a_v = 6/D_p$, and k becomes,

$$k = \frac{D_p^2\phi^3}{72\tau(1-\phi)^2} \tag{2.13}$$

Panda and Lake modified equation 2.12 to a medium consisting of spherical particles with a range of particle diameters with an arbitrary PSD. They consider a homogeneously packed assembly of particles that has a number frequency distribution of the PSD given by $f(D_p)$such that

$$\int_0^\infty f(D_p)dD_p = 1$$

then the average value of a_v for this assembly is given by,

$$a_v = 6E_2/E_3 \tag{2.14}$$

where E_2 and E_3 are the second and third uncentred moments of the PSD. After rearrangement of terms Panda and Lake showed that the permeability can be described as a function of porosity, tortuosity (τ) (assumed to be 3), mean particle size $\overline{D}p$, standard deviation σ, and skewness γ;

$$k = \frac{\overline{D}p^2\phi^3}{72\tau(1-\phi)^2} \times \frac{(\gamma C_{Dp}^3 + 3C_{Dp}^2 + 1)^2}{1 + C_{Dp}^2} \tag{2.15}$$

where C_{Dp} is the coefficient of variation of the PSD; $\sigma/\overline{D}p$. This equation is essentially a modification of the basic Carman-Kozeny model to explicitly include the PSD statistics ($\overline{D}p$, C_{Dp}, and γ) in addition to the bulk properties (ϕ and τ). It is valid for any PSD type. It reduces to equation 2.13 for homogenous media where C_{Dp} is equal to 0.

The terms in brackets can be seen as a correction to the permeability calculated by the basic Carman-Kozeny model (Panda and Lake, 1994).

2.7.2 K from MICP (l_c)

According to Katz and Thompson (1986) K can be calculated from the critical pore size (l_c), the constant C, and the electrical conductivity, σ/σ_0 where σ is the conductivity of the rock saturated with a brine solution of conductivity σ_0 via;

$$K = Cl_c^2\sigma/\sigma_0 = Cl_c^2\phi/\tau \tag{2.16}$$

where C is a constant ($\frac{1}{226}$). In a recent study of sandstones the value of $\frac{1}{226}$ used for C has been reanalysed and found to be more properly represented by 0.16 when l_c is defined as a critical radius (Bauget et al., 2005a; Arns et al., 2005b). This value is used in all calculations using equation 2.16 in this thesis. The parameters in the equation can be extracted from an MICP experiment. l_c is defined as the point on the mercury injection curve where positive curvature changes through a rapid rise to negative curvature or the pressure at which the intrusion volume vs pressure on the Hg intrusion curve is the steepest (recall the red arrow in Figure 2.17). This point (inflection point) is interpreted as the measured pore diameter at which the intruded Hg initially forms a connected cluster that spans the sample (Katz and Thompson, 1986). In effect the smallest constriction present in the connected cluster

that spans the sample (Bauget et al., 2005a). τ is calculated by its relationship to F and ϕ where the conductivity of the solid phase is set at zero. The formation factor $F = \frac{1}{\sigma/\sigma_0} = \tau/\phi$ reflects the porosity and connectivity of the pore space and is derived directly from the image by calculating the effective electrical conductivity of the fluid filled rock (σ), which is divided by the conductivity of the saturating fluid (σ_0).

Examples of K obtained using this method have been compared to values obtained experimentally for a range of rock samples; results are presented in Figure 2.19(a). From this Figure we see that this method is a reliable technique for calculating K.

2.7.3 K from 3D Images

2.7.3.1 Lattice-Boltzman (LB)

A microstructure defined by a digital image is already naturally discretised and lends itself immediately to numerical computation of any number of quantities. The permeability calculation used here is based on a lattice-Boltzmann method (LB) using D3Q19 (3 Dimensional lattice with 19 possible momenta components) (Qian et al., 1992). The implementation of the algorithm is similar to that detailed in Martys et al. (1999); Martys (2001). The physical boundary condition at solid-fluid interfaces is the no-flow condition which in the LB methods is most simply realised by the bounce-back rule (Martys and Chen, 1996). Mirror image boundary conditions (Martys et al., 1999) are applied in the plane perpendicular to the flow direction and all simulations performed on an $L \times L \times 2L$ system. The pressure gradient acting on the fluid is simulated by a body force (Ferreol and Rothman, 1995) applied in the central L^3 subset where permeability is measured. In all cases the LB relaxation parameter $\tau = 1$ is used. A problem with LB methods is the computational expense; running a simulation at the full image volume remains prohibitive. The group at ANU has considered extensively whether a smaller size of image is large enough to give relevant predictions. This requires comparison of grid size to some statistical length scale (e.g., correlation length, average particle size). Errors will occur if we use too few pores/particles in the system to calculate the numerical permeability. They have found that

a system size which has an acceptable finite size error but is small enough to be computationally feasible is of the order of 500-1000 grains per image. In the work here permeability simulations are performed on 225×216^3 blocks from within the fiducial volume. Values are plotted against the calculated ϕ for each block (see Figure 2.19(b)). An average over all the calculated permeability values gives an indication of the K of the larger sample. Figure 2.19(c) shows K for a Fontainbleau sandstone sample simulated from 3D images using LB compared to K measured experimentally for a sandstone sample. From this data it can be seen that the Lattice-Boltzman technique is an accurate method of calculating K for simple sands at small length scales.

2.8 Relative Permeability (K_r)

Relative permeability refers to a fluid's ability to displace another immicible fluid within a porous media and the associated changes in flow characteristics with varying saturation (Domenico and Schwartz, 1998; Sahimi, 1993). Fluid phases referred to in this thesis are air and water. Air is always the displaced or non-wetting fluid. Partial saturation conditions always refer to the percentage of void volume filled with water (eg. 100% saturation (S_{100}) refers to 100% saturation with water). The fluid geometries at intermediate saturations are distributed assuming the fluids have migrated and occupy the most favourable pore spaces; as this is a water wet case the air will fill the largest pores and throats while the water will preferentially occupy the smaller pores and throats (Figure 2.20(a)). To define the phase distribution at different saturations and under varying wetting conditions we define locally on the image the diameter of the largest sphere which lies within the pore space and covers every voxel (CRT). Non wetting fluid resides in the regions of large covering sphere radius and the wetting fluid resides in regions with small covering radius. By incrementing the value of the covering sphere radius one can vary the effective saturation. An illustration of the fluid distributions within a small subset of an unconsolidated sample volume under water-wet conditions at high and low water saturations is shown in 2D in Figure 2.20(a) and (b).

As a direct consequence of an increasing wetting phase saturation, K_{water}

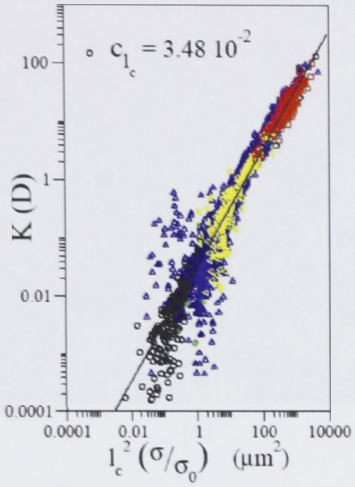

(a) Comparison of simulated permeability to the Katz and Thompson prediction (from Bauget et.al. 2005a). Different colours denote different rock types.

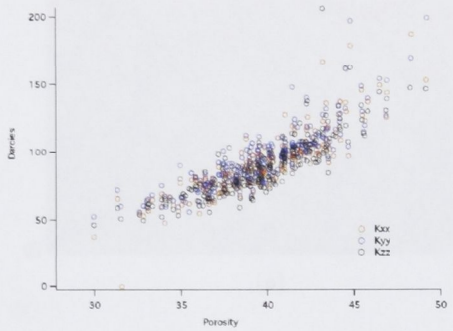

(b) An example of permeability calculated by LB and porosity calculated on 225 subsets from within a 3D image .

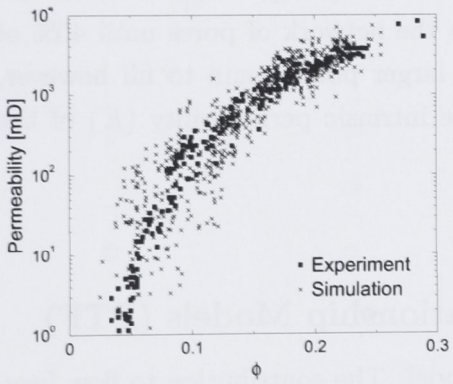

(c) Comparison of permeability simulation from lattice Boltzman calculation with experimentally measured data on Fontainbleau sandstone. (from Arns et. al. 2005)

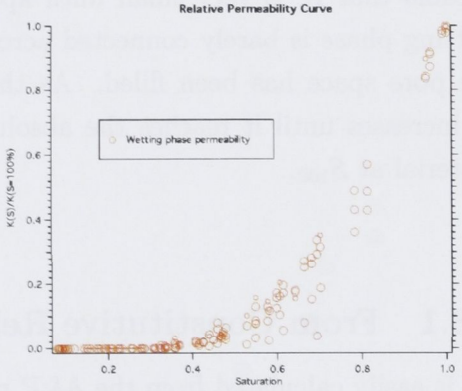

(d) An example of relative permeability data calculated from the 3D image using the LB technique.

Figure 2.19: Comparitive K measures using Katz and Thompson and lattice Bolzman techniques.

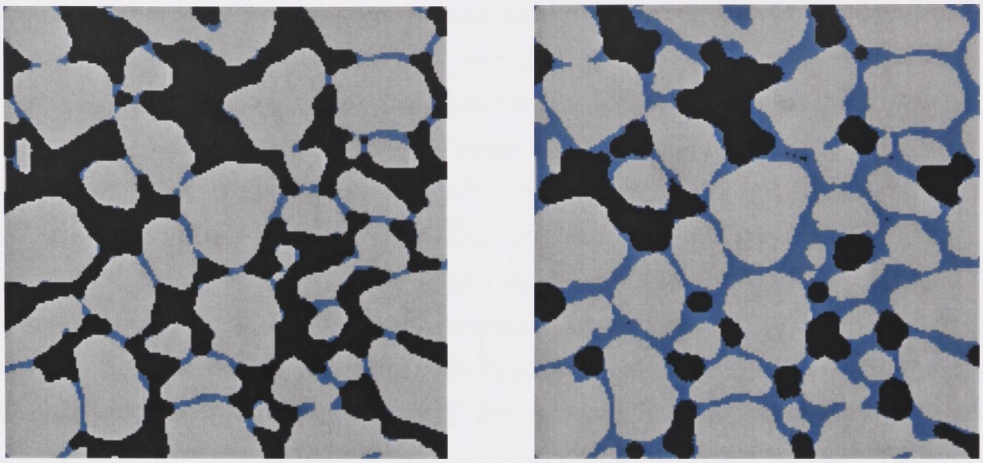

(a) (b)

Figure 2.20: Figures (a) and (b) show the displacement of the defending, non-wetting phase, air, by the invading wetting phase, water. Air is black and water is green.

will increase; a plot of K_{water} versus S_w is given in Figure 2.19(d). It is notable that K is very small until approximately S_{40}; this is because the wetting phase is barely connected across the network of pores until 40% of the pore space has been filled. As the larger pores begin to fill however, K increases until it reaches the absolute intrinsic permeability (K) of the material at S_{100}.

2.8.1 From Constitutive Relationship Models (PTF)

K_r is easily calculated from the A&P model. The contribution to flow from each family of pores (q_i) is summed up to the given S_w from smallest to largest (see Section 2.7.1.1). As S_w decreases the contributions from the largest pores are removed (Arya and Paris, 1981).

2.8.2 Image Based

Relative permeability calculations are also made on the 225 x 216^3 discrete blocks from the 3D image using the LB method. Using the phase distribu-

tions defined by the CRT, multiple calculations of water K_r are made for each block at various S_w. Boundaries between the wetting and non wetting phases are treated as non slip boundaries, as are the solid phase boundaries (Inamuro et al., 1995; Arns et al., 2004).

Part II

Results

Chapter 3

Ottawa Sand

3.1 Description

In this section the analysis of two model sand packs is described. $20cm^3$ of unground silica was obtained from the U.S. Silica Co® (product specifications are given in Figure 3.1). This material was split into 2 samples and each was packed in a separate $17mm$ diameter Al tube, each with a volume of $7.39cm^3$. These 2 packs are named OSC and OSC2. From the product data (Figure 3.1) we note that the constituent particles are primarily quartz in the size range 200-600μm (diameter).

X-ray tomographic data was obtained for both samples as described in (Section (2.2.3.2)). Details of the acquisition parameters and the sample dimensions for both samples are summarised in Tables 3.1(a) and (b). 2D slices through the 2048^3 tomographic datasets OSC and OSC2 are shown in Figures 3.2(a)(b) and 3.3(a)(b) respectively.

The x-ray attenuation histograms (Figures 3.2(c) and 3.3(c)) are very clean and little filtering or edge enhancement was required for accurate phase separation of either sample. A sub volume of the full 3D dataset, defined as the fiducial volume, is chosen for direct analysis of the sand structure and properties. The fiducial volumes are cylindrical subsets 1904 voxels in length with radii of 830 voxels. These subvolumes were chosen to exclude the aluminium sample tube and the first 2-3 grains from the tube grain interface. An example of the fiducial subvolume is given in 3.2(a). A cross section

through the segmented fiducial subsets obtained from the original tomograms are presented in Figures 3.2(d) and 3.3(d). All analysis is undertaken on these volumes.

Upon initial visual inspection of the 2D slices we note that these samples appear to consist of well sorted, well rounded particles. Irregularities in the packing process appears to have created faint laminations of more tightly packed particles more obvious in OSC (Figure 3.2(b)) than OSC2 (Figure 3.3(b)).

U.S. SILICA®

Sands of Time

PRODUCT DATA

CRYSTAL

UNGROUND SILICA

PLANT: OTTAWA, ILLINOIS

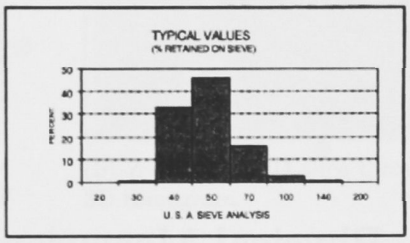

USA STD SIEVE SIZE		TYPICAL VALUES		
		% RETAINED		% PASSING
MESH	MILLIMETERS	INDIVIDUAL	CUMULATIVE	CUMULATIVE
20	0.850	0.0	0.0	100.0
30	0.600	1.0	1.0	99.0
40	0.425	33.0	34.0	66.0
50	0.300	46.0	80.0	20.0
70	0.212	16.0	96.0	4.0
100	0.150	3.0	99.0	1.0
140	0.106	1.0	100.0	0.0
200	0.075	0.0		

TYPICAL PHYSICAL PROPERTIES

AFS[1] ACID DEMAND (@pH 7)	<1.0	MELTING POINT (Degrees F)	3100
AFS GRAIN FINENESS	40	MINERAL	QUARTZ
COLOR	WHITE	MOISTURE CONTENT (%)	<0.05
GRAIN SHAPE	ROUND	pH	7
HARDNESS (Mohs)	7	SPECIFIC GRAVITY	2.65

(1) AMERICAN FOUNDRYMEN'S SOCIETY

TYPICAL CHEMICAL ANALYSIS, %

SiO_2 (Silicon Dioxide)	99.8	MgO (Magnesium Oxide)	<0.01
Fe_2O_3 (Iron Oxide)	0.019	Na_2O (Sodium Oxide)	<0.01
Al_2O_3 (Aluminum Oxide)	0.05	K_2O (Potassium Oxide)	<0.01
TiO_2 (Titanium Dioxide)	0.01	LOI (Loss On Ignition)	0.1
CaO (Calcium Oxide)	<0.01		

December 15, 1997

Figure 3.1: Specifications for Crystal type, Ottawa sand. Data reproduced from the product specifications received with the sample (U.S. Silica Co. Ottawa. Illinois).

(a) Aquisition parameters	
sample distance	$410mm$
camera length	$1500mm$
voltage	80kV
beam current	$200\mu A$
exposure time	21 sec
filter	$3mm$ silica

(b) Sample dimensions		volume
tube height	$35mm$	$7.39cm^3$
tube inner radius	$8.2mm$	
image	2048^3 voxels	$6.56cm^3$
fiducial radius	830 voxels	
fiducial height	1904 voxels	$3.19cm^3$
voxel size	$9.18\mu m$	$774\mu m^3$

Table 3.1: (a) Tomogram aquisition parameters for both subsamples; OSC and OSC2. (b) Sample size and image specifications.

3.2 Physical Measurements

3.2.1 Density and Porosity

Density (ρ) and porosity (ϕ) were calculated from measurements of weight and volume. The sample was dried at 105^0 C for 24 hrs and dislodged from the Al tube as a loose grain pack. The sample weighed 12.0383g. The particle volume as measured by He displacement was $4.5469cc$. Particle density is therefore $2.648g/cc$. This value is reasonable; sufficiently close to quartz ($2.65g/cc$), which accounted for up 99.8% of the grains (Figure 3.1(b)).

From the tube volume ($7.39cm^3$), the porosity and bulk density within the tube are found to be 38.47% and $1.625g/cc$ respectively. Porosity was also calculated directly from the segmented 3D image on the fiducial subsets illustrated in Figures 3.2(d) and 3.3(d). Porosity from this method was 36.6% for OSC and 36.1% for OSC2. These are realistic values for unconsolidated sand packs (Domenico and Schwartz, 1998). The porosity value obtained from the measurement of tube volume is slightly higher than that obtained from direct measurement on the image. This is due to edge effects created by irregular particles packing against the smooth tube wall (see Figures 3.2(a)

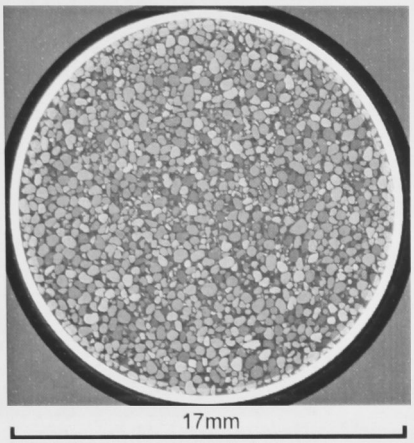

(a) 2D xy slice through the x-ray intensity map perpendicular to the cylindrical (z) axis.

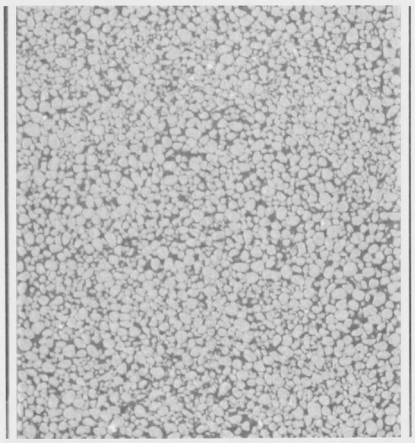

(b) Z direction 2D slice through the 3D tomogram.

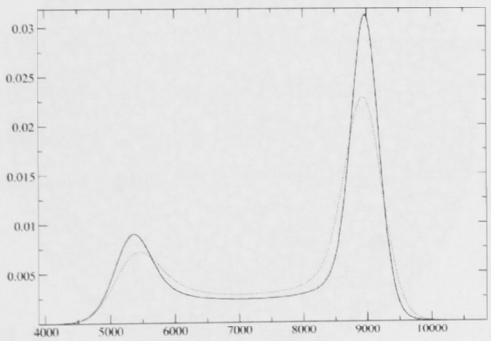

(c) X-ray intensity histogram. Dotted line is original data solid line is the filtered data.

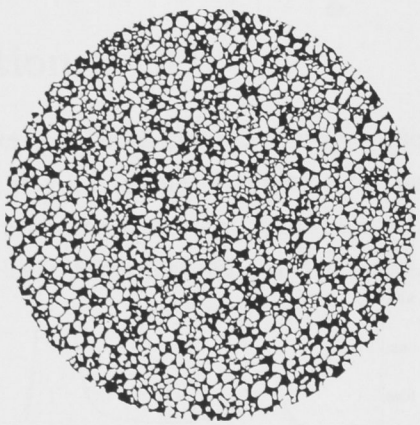

(d) The xy slice through the segmented fiducial volume.

Figure 3.2: Fiducial and segmentation for sample OSC.

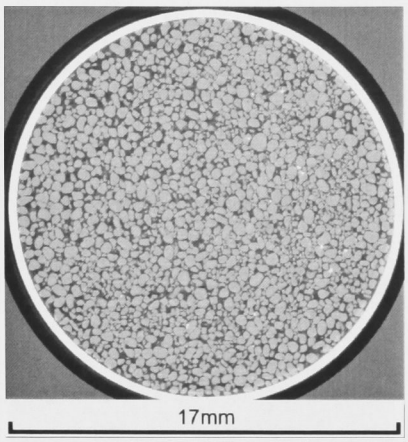

(a) 2D xy slice through the x-ray intensity map perpendicular to the cylindrical (z) axis.

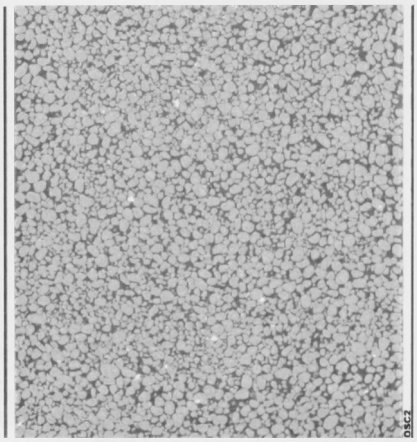

(b) Z direction slice through the 3D tomogram.

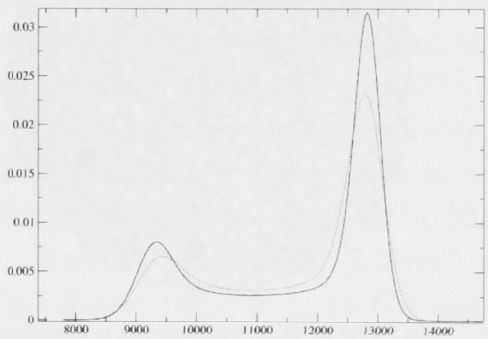

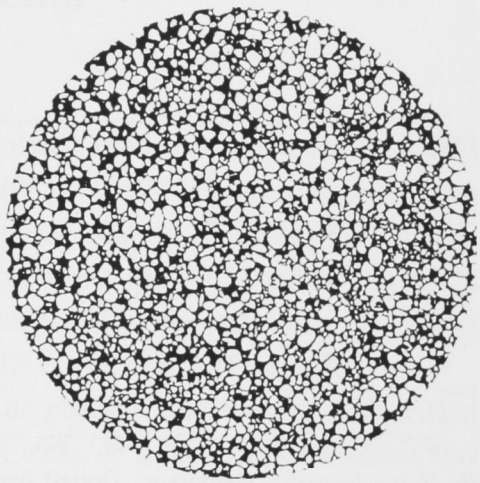

(c) X-ray intensity histogram. Dotted line is original data solid line is the filtered data.

(d) The xy slice through the segmented fiducial volume.

Figure 3.3: Fiducial and segmentation for sample OSC2.

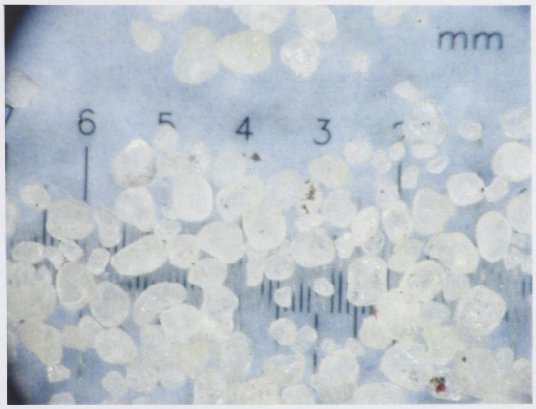

Figure 3.4: Grain morphology and size from microscope. The scale is in $1mm$ major increments.

and (b) and 3.3(a) and (b)) which leads to an artificially high porosity value in the region of the tube wall. Very small pores not resolved due to voxel size also contributes to this effect. It is believed the image based porosity is the more representative value for a grain pack.

3.3 Particle Size Distribution (PSD)

The PSD of the sample was computed directly on both the 3D tomographic datasets. It was also measured by sieving and LLS. Visual inspection of the particles using a microscope indicates most are fairly spherical, well rounded, and very well sorted (Figure 3.4) with particles in the $\approx$200-600μm size range.

3.3.1 Sieve

Sieve results as provided by the U.S. Silica Co. are presented in Figure 3.1 and 3.5(a). From these Figures we see 99% of the particles have a diameter greater than 150μm. This sample is therefore classified as a sand. The largest particles in the distribution do not exceed 850μm. The average volume weighted particle size is 324μm. The median is 376μm and the mode falls in the 300-425μm range (see Table 3.2). The sample size was very large.

For comparison of the PSD across methods we use the Udden-Wentworth (log2) scale; this is presented in Figure 3.5(b). The rebinning of the data resulted in almost 80% of the volume being reclassified into the 250-500μm range.

3.3.2 Laser Light Scattering (LLS)

After imaging the samples were split into equal halves and one half of each sample was sent to the the Particle and Surface Sciences laboratory for LLS particle size analysis. 3cc of material was used for OSC and 2.86cc of material was used for the OSC2 analysis. Figures 3.5(c) and (d) show the PSD based on the Udden-Wentworth scale. Mean volume weighted particle diameter was 489μm for OSC and 483μm for OSC2. A significantly larger number of particles with a diameter >500μm were identified using this technique than reported via sieve analysis. A comparison is given in Table 3.2.

3.3.3 3D Image Analysis

PSD obtained from the respective 3D images was derived using the process outlined in Section 2.3.4; 127,830 and 146,460 individual particles from OSC and OSC2 respectively are labelled. Examples of the identification process from 2D slices through the 3D dataset are presented in Figures 3.6. As the 3D datasets have voxel sizes of 9μm, only particles of the order $\approx$20μm and larger can be resolved. This is not problematic since according to the U.S. Silica Co. all particles in this sample are greater than 75μm (see Figure 3.1).

Analysis of the 3D image allows measurements to be made on every individually identified particle. The PSD generated from these labelled datasets are presented in the cumulative volume frequency traces in Figure 3.5(e) and (f). Analysis of these datasets yielded a volume weighted particle size distribution for OSC with an average of 410μm, and for OSC2 401μm (Table 3.2).

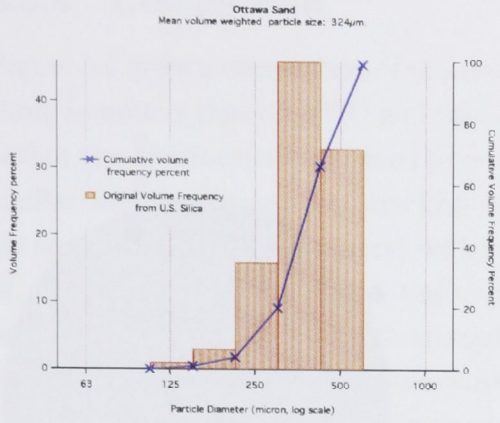

(a) PSD from the U.S Silica Co.

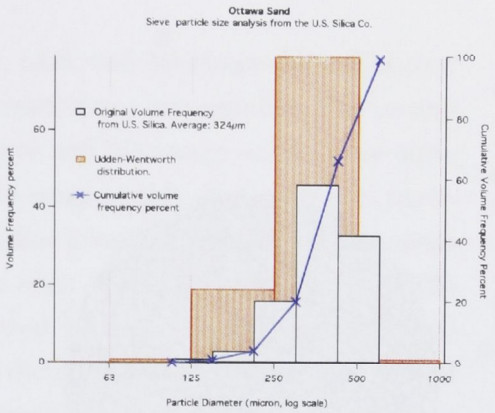

(b) PSD from U.S Silica Co. binned to reflect the Wentworth scale.

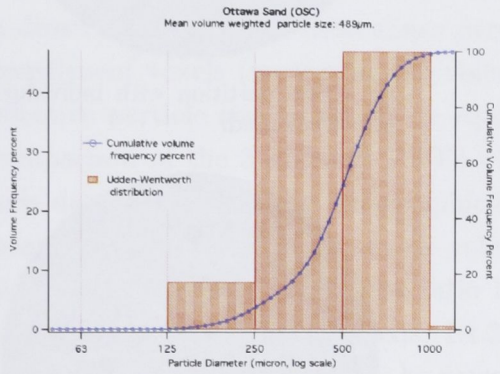

(c) PSD from LLS for OSC.

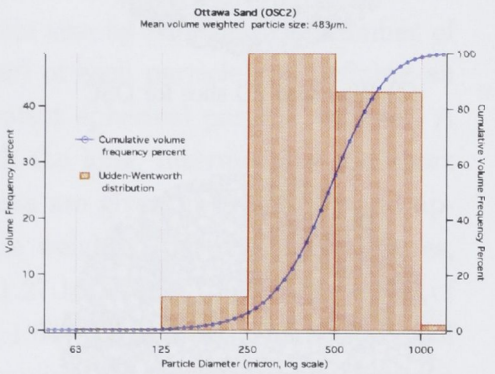

(d) PSD from LLS for OSC2.

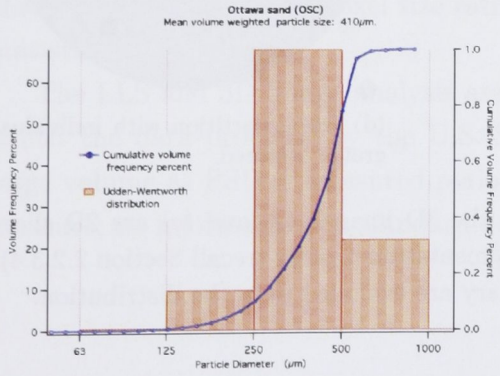

(e) PSD from 3D image for OSC.

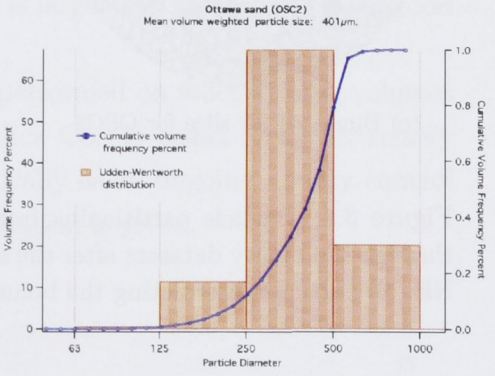

(f) PSD from 3D image for OSC2.

Figure 3.5: Particle size distribution for OSC and OSC2.

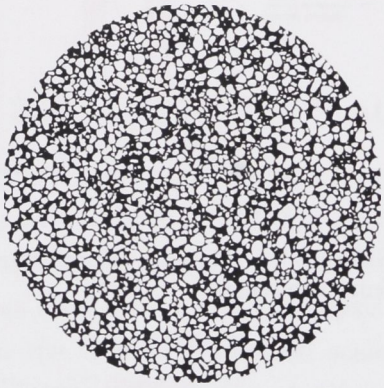

(a) Binarised 2D slice for OSC

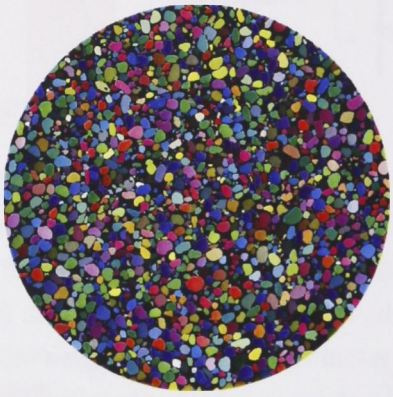

(b) Grain partition with individual grains coloured.

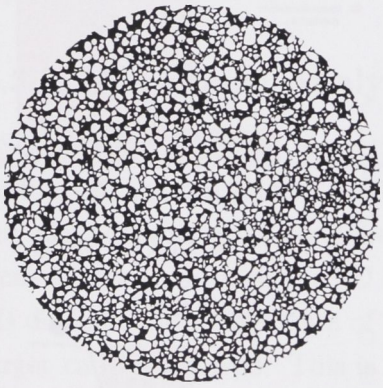

(c) Binarised 2D slice for OSC2

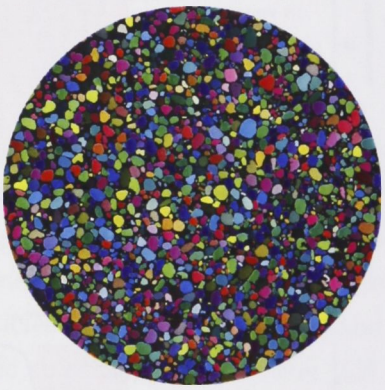

(d) Grain partition with individual grains coloured.

Figure 3.6: Particle partitioning from the 3D image. (a) and (c) are 2D slices through the binary datasets after the segmentation process (recall Section 2.2.3.4). NB. all particles intersecting the boundary are excluded from the distribution.

3.3.4 Comparison

Figure 3.7 gives a comparison of the sieve, LLS, and 3D image data. The first thing to note is that the OSC and OSC2 results are very similar. The second is that the distributions obtained from sieve and 3D image analysis are quite similar, and that in contrast, the LLS data considerably over estimates particle size. This result is consistent with studies investigating the measurement of particle size using the LLS technique such as Xu and Di Guida (2003) and Campbell (2003) who both showed that LLS often overestimates particle size by heavily skewing any measured distribution toward the long axis of the constituent particles. Sieving in contrast would favour the short axis as this is the dimension that will determine whether or not a particle will pass through a certain aperture. Analysis of the tomogram on the other hand is a direct measure. One determines particle size by counting the number of constituent voxels (measuring the volume) of each particle and defining an effective particle size based on an equivalent spherical particle volume. A comparison of the 3 different PSD's with the long, intermediate and short axis data given from the tomographic data are given in Figure 3.8 and appears to confirm this. The mean volume weighted particle size measures, sieve $<$ 3D image $<$ LLS in the ratio 1:1.27:1.51 (OSC) mirror the ratio of short intermediate and long axis; 1:1.31:1.64 (Table 3.3). The accuracy of these measures can potentially be compromised by the quality of the image and voxel size relative to particle size. In this study the image quality is very sharp and the particle to voxel size ratio is large, and we expect to see good statistics.

The LLS and 3D image analysis are performed on $\approx 3cc$ sample volumes whilst the data provided by the U.S. Silica Co. is based on an extremely large volume as PSD is measured periodically as an ongoing quality control measure; no information on standard deviation is given.

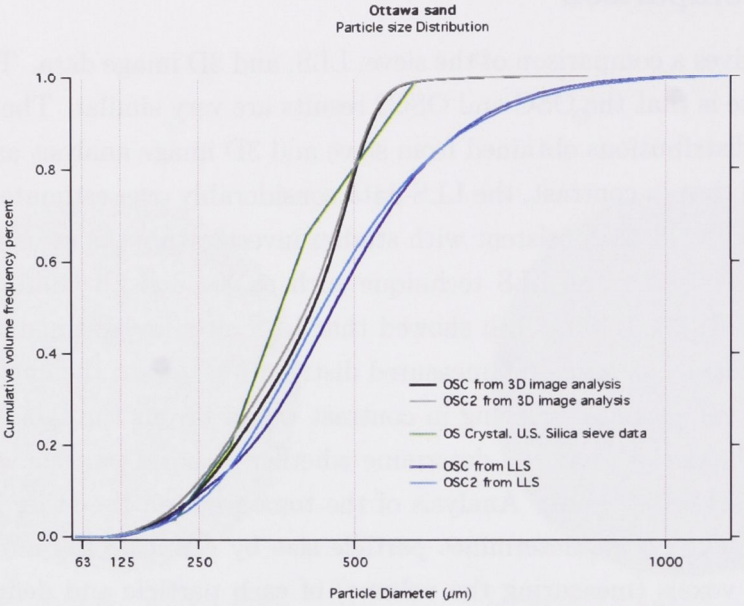

(a)

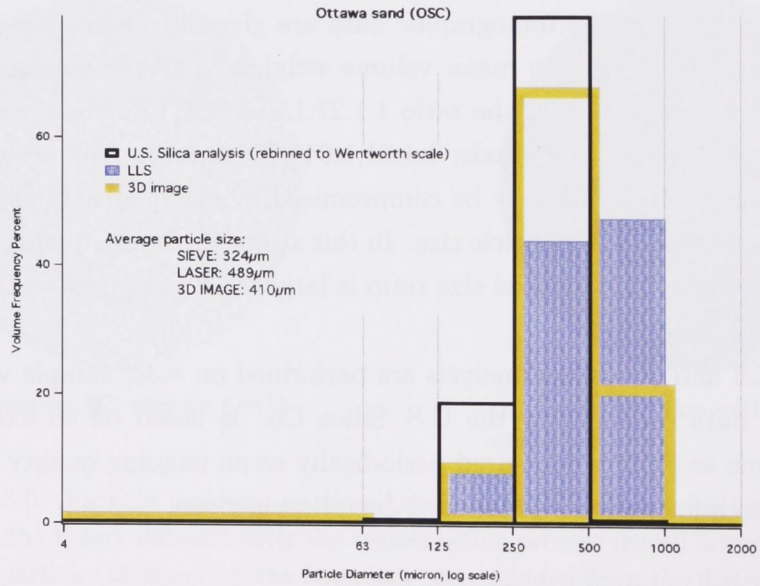

(b)

Figure 3.7: (a) Comparison of the 3 methods used to determine PSD. Sieve (U.S. Silica), LLS and 3D image analysis (b) PSD for OSC binned according to the Wentworth scale.

					Volume weighted μm		
Method	cm^3	% clay	% silt	% sand	Mean	Med.	Mode
Sieve	∞	0	0	100	324	376	300-425
Laser	3.0 & 2.86	0	0	100	489 & 483	480 & 462	503 & 475
X-ray CT*	3.19	0	0	100	410 & 401	467 & 449	347 & 365

Table 3.2: Particle size distribution from the 3 different analytical techniques. NB. Where 2 values are reported they refer to OSC and OSC2 respectively.
** no data on individual particles less than ≈20μm in diameter.*

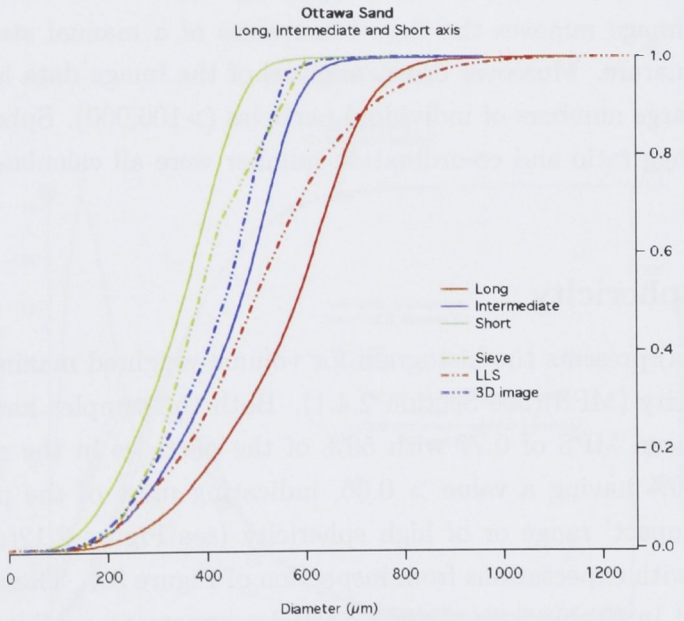

(a)

Figure 3.8: Comparison of the 3 methods used to determine PSD with the long, intermediate and short axis measured from 3D image (results presented for OSC only).

Mean volume weighted measures (μm)				
Axis	Short	Intermediate	Long	ratio
OSC	341	447	558	1:1.31:1.64
OSC2	335	440	549	1:1.31:1.64
PSD	Sieve	3D image	LLS	ratio
OSC	324	410	489	1:1.27:1.51
OSC2	324	401	483	1:1.24:1.49

Table 3.3: Mean volume weighted particle size from the 3 different analytical techniques compared to the long intermediate an short axis dimensions.

3.4 Textural Analysis / Shape Parameters

Textural analysis and fabric measures are traditionally obtained by petrographers via analysis of 2D microscope images. Direct numerical analysis of the 3D image removes the time constraints of a manual study and it's subjective nature. Moreover direct analysis of the image data is capable of analysing large numbers of individual particles (>100,000). Sphericity, sorting, the Zingg ratio and co-ordination number were all calculated from the 3D images.

3.4.1 Sphericity

Figure 3.9(a) presents the histogram for volume weighted maximum projection sphericity (MPS)(See Section 2.4.1). Both the samples have a volume weighted mean MPS of 0.77 with 50% of the particles in the range 0.7 to 0.83 and 90% having a value $>$ 0.66, indicating most of the particles are in the 'Compact' range or of high sphericity (see Figure 2.12(c)). This is consistent with expectations from inspection of Figure 3.4. These results are summarised in (Table 3.4). Larger particles appear to exhibit slightly increased sphericity as the number weighted average is slightly lower than the volume weighted average at 0.75. This is not consistent with the findings of Sneed and Folk (1958) who showed that larger pebbles had lower sphericity. Sneed and Folk (1958) however, investigated the shape of particles in the 32-64mm size range.

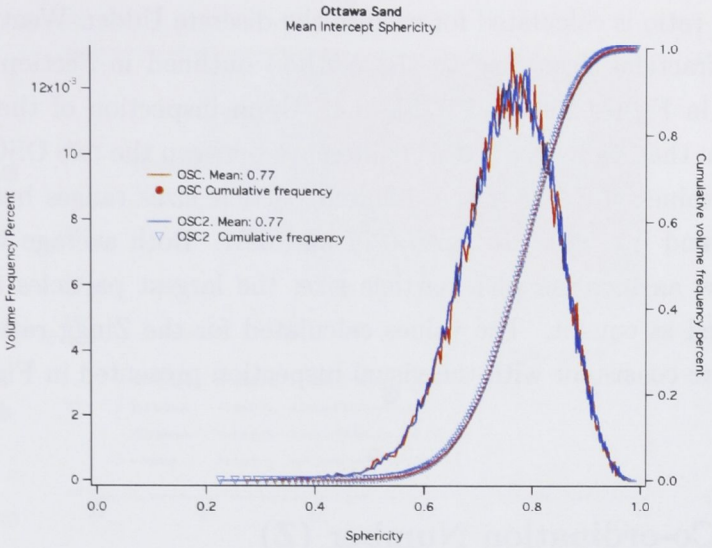

(a) Sphericity.

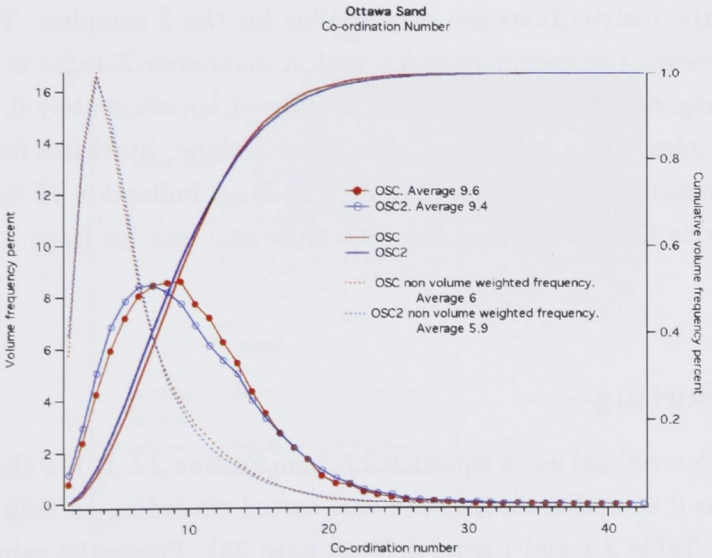

(b) Co-ordination number. Number and volume weighted calculations.

Figure 3.9: Mean intercept sphericity and co-ordination number calculated on over 100,000 individual partices for OSC and OSC2.

3.4.2 Zingg

The Zingg ratio is calculated for each of the discrete Udden-Wentworth particle size fractions according to the method outlined in Section 2.4.2 and presented in Figure 3.10 and Table 3.4. Upon inspection of these plots it can be seen that there is very little difference between the two OSC datasets. Averaged values of S/I over the different particle sizes ranges between 0.72 and 0.79, and I/L varies between 0.77 and 0.81. Both average values generally show an increase with particle size; the largest particles are almost all classified as equant. The values calculated for the Zingg ratio on these datasets are consistent with the visual inspection presented in Figure 3.4.

3.4.3 Co-ordination Number (Z)

Figure 3.9(b) gives co-ordination number distribution calculated for all the particles; the distributions are very similar for the 2 samples. The volume weighted mean is approximately 9.5 with a maximum Z value of 42.5. The number weighted distribution has an average of approximately 6, indicating larger particles have a larger Z. This is a low Z value. Statistics for this analysis are presented in Table 3.4. Figure 3.11 is an indication of the topology of the sample illustrating the uniform nature and lack for large Z values.

3.4.4 Sorting

Sorting is determined using equation 2.5 from Section 2.5.1. For the 2 samples sorting was 0.43 and 0.46; they are well sorted according to Folk and Ward (1957)(see Table 2.1 and Figure 2.13 on page 36). Percentile values used to calculate the sorting coefficient can be found in Table 3.4.

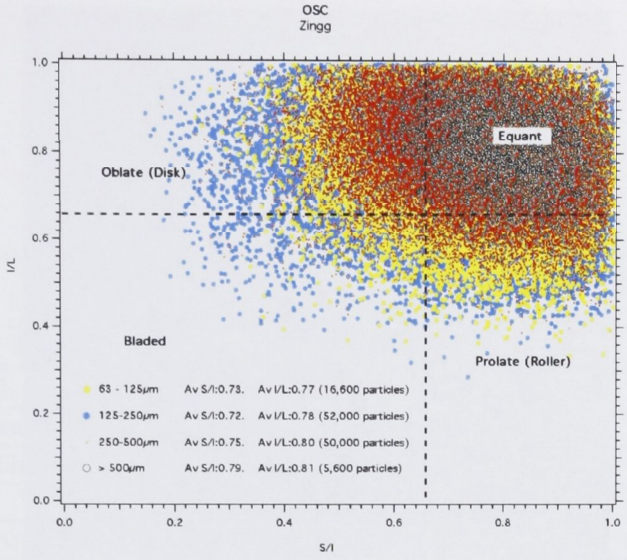

(a) Zingg ratio for OSC.

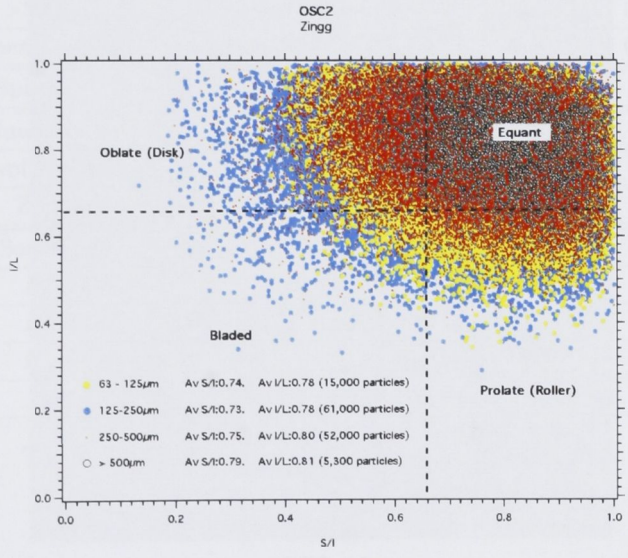

(b) Zingg ratio for OSC2.

Figure 3.10: The Zingg ratio of long, intermediate and short axis of individual particles measured on individual particles identified in the 3D tomogram. Colour is associated with particle size.

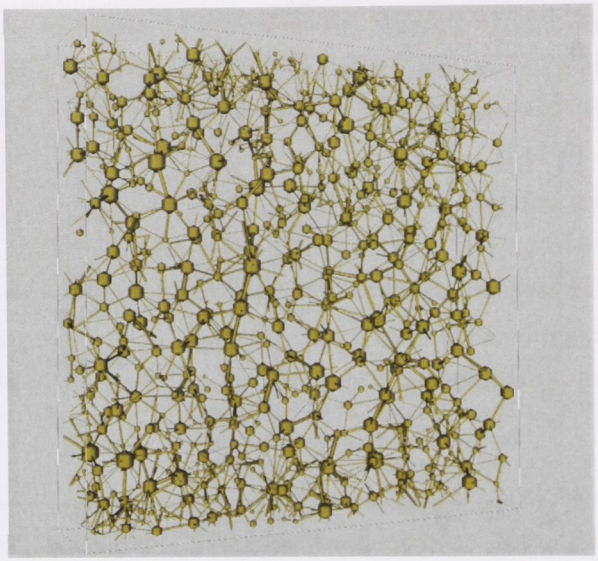

(a) OSC

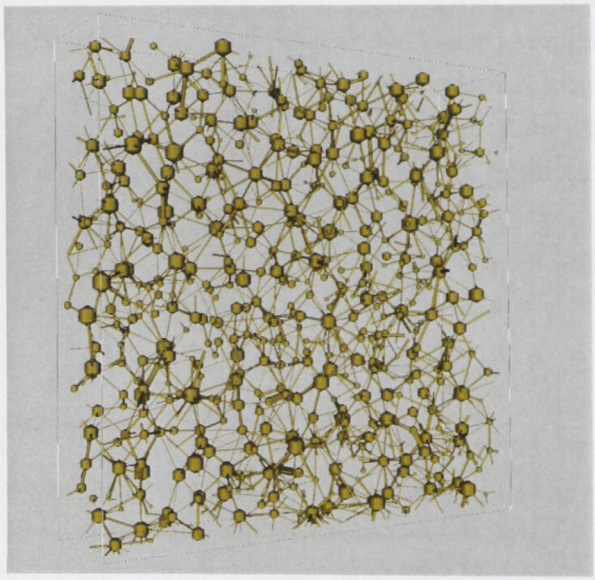

(b) OSC2

Figure 3.11: Network for the particle phase of the sample illustrating the topology of the grain pack. Spheres are the grain centres and their size is directly correlated to the size of the particle represented. Contacts are represented by sticks.

	Number of particles		Mean			
Zingg	OSC	OSC2	OSC		OSC2	
Long μm	124,557	135,196	558		549	
Intermediate μm	124,557	135,196	447		440	
Short μm	124,557	135,196	341		335	
			S/I	I/L	S/I	I/L
63-125μm	16,636	15,994	0.73	0.77	0.74	0.78
125-250μm	52,145	61,764	0.72	0.78	0.73	0.78
250-500μm	50,168	52,092	0.75	0.80	0.75	0.80
>500μm	5,608	5,346	0.79	0.81	0.79	0.81
mean Zingg	124,557	135,196	0.75	0.79	0.75	0.79
Sphericity	124,557	135,196	0.77		0.77	
Z (volume weighted)	124,557	135,196	9.6		9.4	
Z (non-volume weighted)	124,557	135,196	6		5.9	
Z max	124,557	135,196	41.5		42.5	
Sorting ϕ	124,557	135,196	0.43		0.46	
$D_{84}\phi$	124,557	135,196	1.109		1.120	
$D_{16}\phi$	124,557	135,196	1.971		2.043	
$D_{95}\phi$	124,557	135,196	1.012		1.015	
$D_5\phi$	124,557	135,196	2.450		2.522	

Table 3.4: Summary values for textural measures.

3.5 Pore-Size Distribution

In this section we compare a number of pore size descriptors for these samples. PSD is converted to pore-size distribution using the A&P model (recall Section 2.6). Pore-size distribution is also calculated directly from the 3D images using the covering sphere transform (CRT) (see Section 2.3.3.1), via a simulated MICP experiment (see Section 2.6.2.1), and based on a calculation of pore network descriptions (see Section 2.6.2.2). These distributions are then compared.

3.5.1 Arya and Paris Model (A&P) from Grains to Pores

The A&P algorithm was applied to PSD obtained from sieve, LLS and 3D image analysis (recall section 2.6.1.1). The porosity value used for the calculation was 36.6% for OSC and 36.1% for OSC2 as measured on the respective tomograms. Parameters used in the calculation were $a = 2.478$, $b = 1.490$ (from Table 2 in Figure 2.15), $\log c = 2.507$ and $x = 4.471$ (from Table 3 in Figure 2.15). a and b are defined according to the textural class of the sample, which was sand. The $\log c$ and x parameters chosen are the values from Figure 2.15 corresponding to the highest percentage sand and lowest percentage clay as no clay was identified in either sample. The PTF is performed on all the data from sieve, LLS and image for illustration.

3.5.1.1 Pore-Size Distribution from Sieve

The pore-size distribution was first calculated from the PSD data provided by the U.S. Silica Co. Illinois (Figure 3.1(a)). Figure 3.12(a) shows the results of this calculation and the relevant PSD. For the smaller pores and particles the pore and PSD distribution curves track each other with the relative pore size at the same volume frequency approximately 5 times smaller than the PSD. The last 2 points; ie. the biggest particles and biggest pores are of equivalent magnitude and for the largest particles a 1:1 ratio is seen. Pores in this distribution range between 12 and $350\mu m$. Average pore size was calculated to be $37.27\mu m$.

3.5.1.2 Pore-Size Distribution from LLS

PSD from LLS was used to compute the pore-size distributions presented in Figure 3.12(b). The PSD for the 2 OSC samples were very similar the resultant pore-size distributions were also very similar. The distributions ranged from $0.5\mu m$ to $3000\mu m$. Average pore radius was $132\mu m$.

For the smaller features the pore to particle size ratio is approximately 3:1. This ratio decreases with particle size. For the largest particles the pore radius is greater than the particle size from which it was derived; pores with a radius $>600\mu m$ are predicted (see Figure 3.12(b)). This aphysical result is due to the extreme values for α_i that are derived using the A&P methodology. One obtains strongly varying values as the bins contain a smaller number or fraction of particles (recall Section 2.6.1.1.

3.5.1.3 Pore-Size Distribution derived from x-ray Tomogram

The pore-size distribution calculated via A&P from the 3D image is shown in Figure 3.12(c). Generally the pore-size distribution follows the PSD data but is approximately 5 times smaller. The radius of the biggest 5% of the pores are very large relative to the rest of the distribution. Average pore size was approximately $63\mu m$.

3.5.2 Direct calculation of pore size from 3D Image

3.5.2.1 Covering Sphere Transform (CRT)

This technique for defining the pore size of a 3D image is outlined in Section 2.3.3.1 on page 29. Figure 3.13 shows that the results for the two individual samples are very similar. The distributions cover the range from 11 to $160\mu m$. 90% of this volume is found in the 13 to $89\mu m$ range. The distribution is quite broad; significant volume is attributed to pores of all size ranges. The average pore radius for OSC is $45.4\mu m$ and for OSC2 $40.8\mu m$.

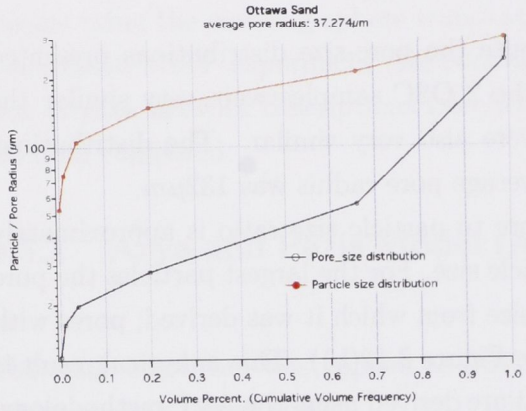

(a) Pore size distribution converted from U.S.Silica (sieve) PSD.

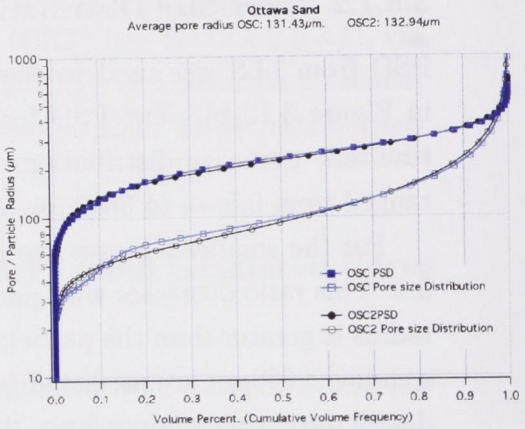

(b) Pore size distribution converted from LLS data.

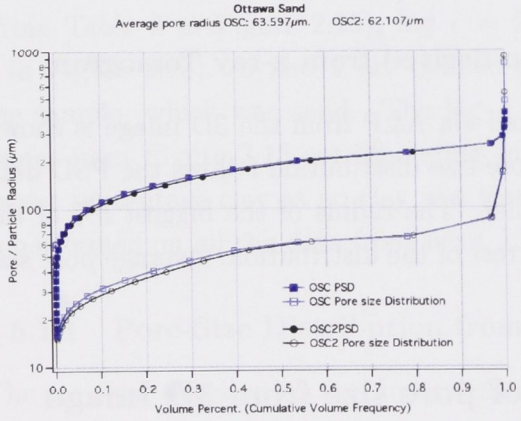

(c) Pore size distribution converted from 3D image PSD.

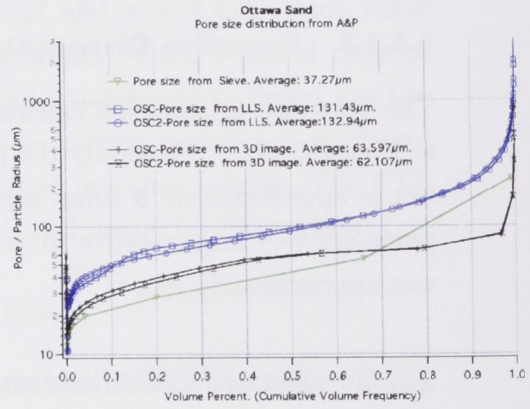

(d) Comparison of the pore size distribution converted from PSD.

Figure 3.12: Pore-size distributions converted from PSD using the Arya and Paris Model.

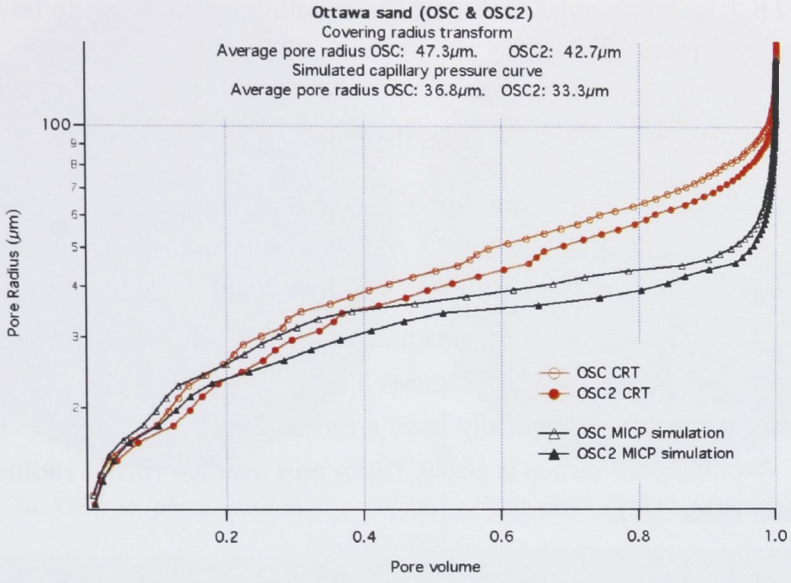

Figure 3.13: Pore-size distribution of OSC and OSC2 calculated from the 3D data sets as a covering sphere transform and a simulated capillary pressure curve.

3.5.2.2 Simulated MICP (Capillary pressure)

Figure 3.13 also shows the results of the numerical MICP simulations with pore entry radius compared to pore volume (saturation). The distributions cover the range 11 to 147μm. Less than 1% of the pore volume however has a radius greater than 63μm and 90% of the pore volume falls in the range 13 to 60μm. The distribution flattens out within this range as a result of smaller entry pores shielding larger pore volumes during the Hg injection process (recall Figure 2.16(c) on page 42). Hg enters a pore through a particular constriction and all pore volume accessible to the invading Hg after entry is associated with that particular entry radius. This leads to the relatively smooth and flat distribution which contrasts with the data from CRT. This difference is visible in Figure 3.13 as a divergence of the two curves at about 25μm. The average pore radius from the MICP simulation is 35.2μm for OSC and 31.7μm for OSC2, $\approx$10μm smaller than CRT. The l_c radius (recall

Section 2.6.2.1) was calculated during the simulation and found to be 43.9μm for OSC and 41.4μm for OSC2.

3.5.2.3 Network pore-size distribution

The process involved in partitioning of the void phase into pore and throat is outlined in Section 2.6.2.2 on page 42. 2D slices through the partitioned OSC volume are presented in Figure 3.14(a) and (b). A subsection of the partition presented as a network in 3D is shown in Figures 3.14(c)(d). Analysis of the partitioned data is presented in Figures 3.14 (e) and (f). From this analysis it can be seen that pores typically have a radius a factor of 2 larger than the throats. Average pore radius is about 70μm and average throat radius about 35μm (see Table 3.5).

3.5.3 Comparison of the techniques used to obtain pore-size distribution

All the techniques used here to measure the pore-size distribution agree reasonably well; all identify a pore size range between 10-100μm for most pores (Figure 3.15). Average pore radius is given in Table 3.5 and is between 30 and 60μm. l_c falls in this range and approximates the mean value from CRT.

The distribution from A&P closely approximates the pore size from other measures except for the largest 5% where A&P predicts the presence of pores with radius greater than 2mm; this is not observed in any of the direct measures of pore-size distribution nor can it be inferred from visual inspection of the 3D images.

Figure 3.15 reveals that the pore and throat network analysis provide upper and lower bounds on the other distributions.

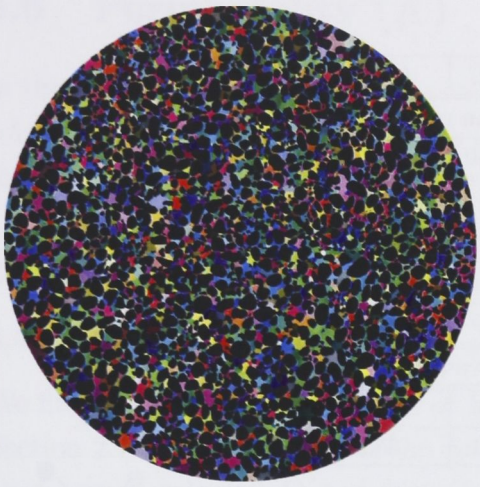

(a) OSC all pores labelled.

(b) OSC all throats labelled.

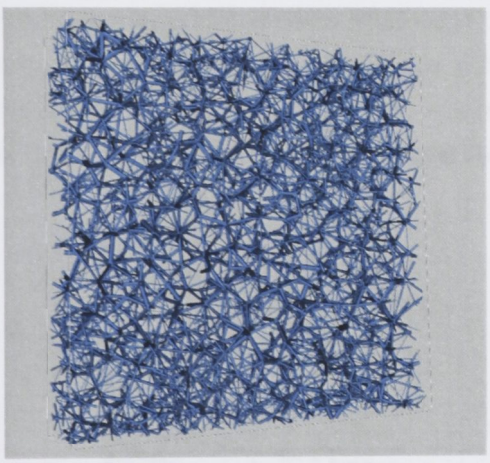

(c) 3D network representation of the pore size distribution for sample OSC. This subset is 110x500x500 voxels. This network represents less than 2 percent of the total image volume.

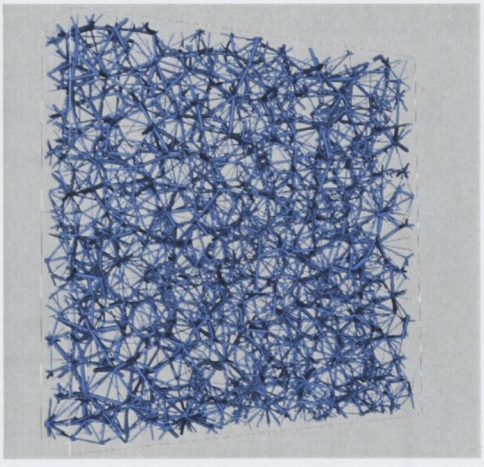

(d) 3D network representation of the pore size distribution for sample OSC2. This subset is 110x500x500 voxels. This network represents less than 2 percent of the total image volume.

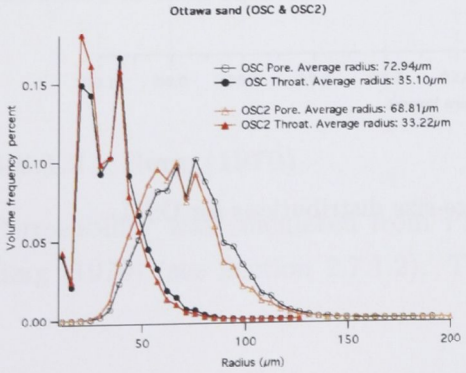

(e) Frequency percent of pore and throat radii volume weighted

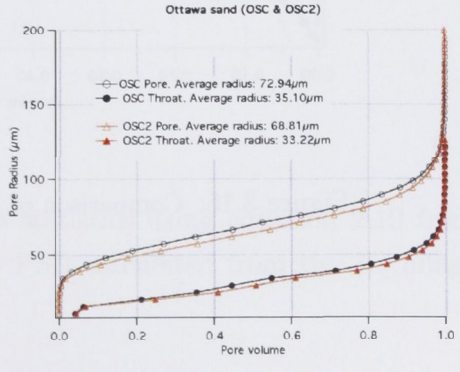

(f) Cumulative frequency percent of pore and throat radii volume weighted

Figure 3.14: Network analysis.

	OSC	OSC2
Method	Mean radius (μm)	
A&P	63.60	62.12
Image Analysis*		
CRT	45.4	40.8
cp	35.2	31.7
l_c	43.9	41.4
Network		
Pore	72.9	68.8
Throat	35.1	33.2

Table 3.5: Pore-size distribution from the different analytical techniques.
** no data for pore radius less than image resolution.*

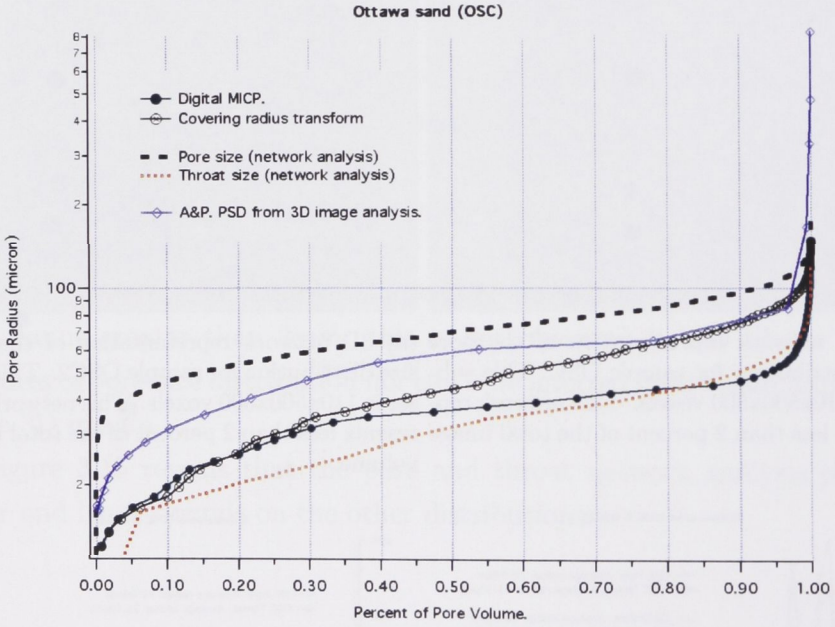

Figure 3.15: Comparison of pore-size distributions for OSC.

3.6 Permeability (K)

In this section permeability (K) is calculated indirectly from PSD using the A&P pedo-transfer model. It is also calculated directly on the 3D image of the samples.

3.6.1 Empirical correlations

3.6.1.1 Arya and Paris

We first consider the calculations of K from A&P, equation 2.8.
Section 2.7.1.1 on page 46 has the detailed description of the algorithm used here to calculate Q_i and then K. The input parameters required for the equation are given in Table 3.6(a). The results of the application of the A&P model to the various PSD statistics are presented in Table 3.6(b). We note that $K_{sieve} < K_{image} < K_{LLS}$. From this data we see that a small difference in PSD translates into a large difference in K. The variation in K from the 3 PSD measures ranges over 4000%.

(a)

ρB	$1.625 g/cm^2$
ρP	$2.6476 g/cm/^2$
ϕ	0.366 & 0.361
a	-2.478
b	1.49
b	321.37
x	4.471
e	0.62929

(b)

	OSC	OSC2
Input PSD	K Darcies	
Sieve	0.09	
LLS	2.88	3.47
3D image	0.32	0.30

Table 3.6: (a) PSD statistics for the A&P calculation of K. (b) Comparison of calculated K from PSD obtained by sieve, LLS and 3D image analysis.

3.6.1.2 Berg (1970)

Permeability was calculated from PSD statistics using equation 2.10 from Berg (1970) (see Section 2.7.1.2). The PSD calculated from the 3D image

analysis was used to obtain the necessary statistics (see Table 3.7). Permeability was found to be 33.58 and 27.95 Darcies.

	OSC	OSC2
D	$0.387mm$	$0.377mm$
ϕ	36.6%	36.1%
d_{10}	2.172	2.252
d_{90}	1.056	1.063
p	0.558	0.594
K	33.6	28.0

Table 3.7: PSD statistics for the calculation of K by Berg (1970).

3.6.1.3 Panda and Lake (1994)

In this section equation 2.15 developed by Panda and Lake (1994) to estimate K in terms of the PSD statistics and bulk properties of a material is applied (see Section 2.7.1.3). The PSD statistics and bulk property input parameters are given in Table 3.8. The equation predicts permeabilities of 77.1 and 68.3 Darcies for OSC and OSC2 respectively. τ was initially taken to be 3 as recommended by Panda and Lake (1994). τ was also calculated from the 3D image and found to be 1.62 and 1.63 (see Figure 3.16). When these values were used K increased to 142.82 and 126.01 Darcies (see Table (3.8)).

	OSC	OSC2
$\overline{D}p$	$257.29\mu m$	$244.51\mu m$
ϕ	36.6%	36.1%
τ	3 & 1.6194	3 & 1.6255
γ	0.652	0.776
C_{Dp}	0.482	0.491
σ	123.97	120.16
K in Darcies	77.1 & 142.8	68.3 & 126.0

Table 3.8: Parameters for the P&L calculation of permeability. The two values for K reflect different values of τ.

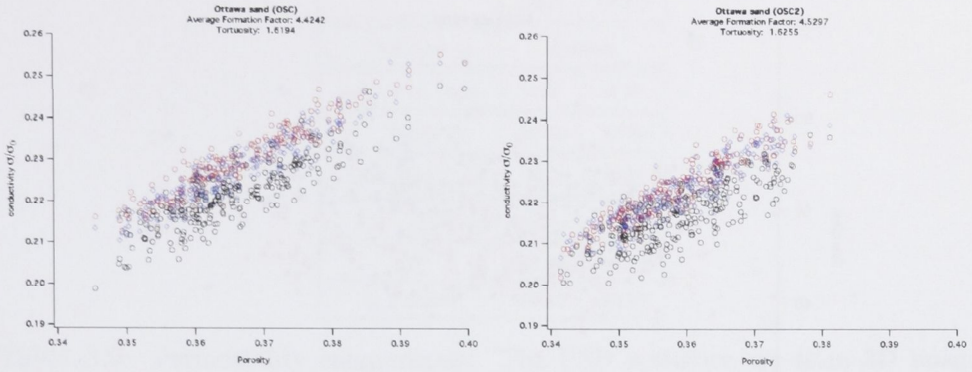

(a) (b)

Figure 3.16: F calculated on 225 discrete 216^3 blocks.

3.6.1.4 MICP Simulation (Capillary Pressure)

Permeability is calculated via equation 2.16 from Section 2.7.2. For OSC l_c was calculated from the image and found to be $43.9\mu m$. τ was measured from the image according to the method outlined in Section 2.7.2 and found to be 1.62, (Figure 3.16(a)) where $F = \frac{1}{\sigma/\sigma_0} = \tau/\phi$ (recall Section 2.7.2); this gives a permeability of 69.69 Darcies.

For OSC2 $l_c = 41.4\mu m$. $\tau = 1.63$ (Figure 3.16(b)), giving $K = 60.57$ Darcies.

3.6.2 3D Image Analysis

3.6.2.1 Lattice-Boltzmann method (LB).

Permeability for OSC and OSC2 was also calculated from the 3D image using the LB algorithm (see Section 2.7.3.1) on 225 subsets per image; the data is plotted as a function of ϕ (Figure 3.17).

K was 62.9 Darcies for OSC and 52.1 for OSC2. Average ϕ and K are slightly higher for OSC than that for OSC2. Porosity varies between 34 and

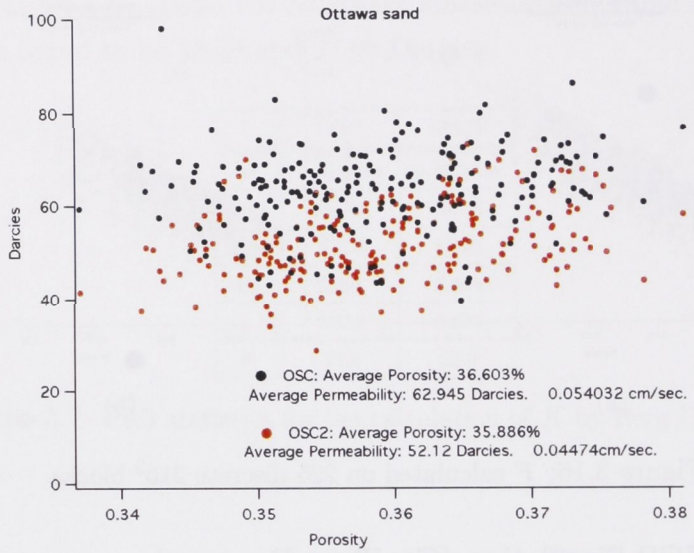

Figure 3.17: Absolute K and corresponding ϕ values for 225, 216^3 discrete blocks calculated using LB.

38%. Despite the small range of ϕ values (4%) a small increase in K with ϕ is discernible.

3.6.3 Comparison of permeability

A comparison of the results calculated from the different methods based on 3D image data are presented in (Table 3.9). From these results we see K values generated by the A&P model are approximately a factor of 100 lower than the other methods. This underprediction is despite the pore-size distribution from A&P exhibiting some very large pores and being based on a parallel tube geometry. This result is due to the empirical nature of the equation (see Table 3.6). K from Berg is a factor of 2 lower than direct image calculations. Using the conventional τ=3 with P&L, it and l_c calculations both give predictions in good agreement with direct simulation.

	OSC	OSC2
Method	Darcies	
Arya and Paris	0.32	0.30
Berg	33.58	27.95
Panda and Lake	77.1	68.3
3D image analysis		
LB*	62.95	52.12
l_c : $44\mu m$	69.69	60.57

Table 3.9: Permeability comparisons. The PSD statistics are from 3D image analysis. * denotes an average value calculated over 225 x 216^3 discrete blocks.

3.7 Relative Permeability (K_r)

3.7.1 Arya and Paris

Inspection of the K_r curves calculated by A&P given in Figure 3.18(a) shows that the K_r in the A&P model exhibits a more significant contribution from the pores with large radius; this in turn is due to the direct conversion of large particles to large pores. The sample begins to conduct at about the 10% saturation level, increases slowly till approximately 95% saturation then K becomes dominated by the few large pores and increases much more rapidly. Less than 5% of the pore volume contributes more than 55% of the overall permeability and 40% of the total permeability is contributed by 1% of the pore volume.

3.7.2 Lattice-Boltzmann method (LB) (3D image analysis).

The K_r curve generated by calculating K using the LB algorithm (see Section 2.8.2) is also presented in Figure 3.18(a). From this Figure we see that the largest 70% of pores contribute most to absolute K with pores in all size ranges except the smallest 30% contributing significantly.

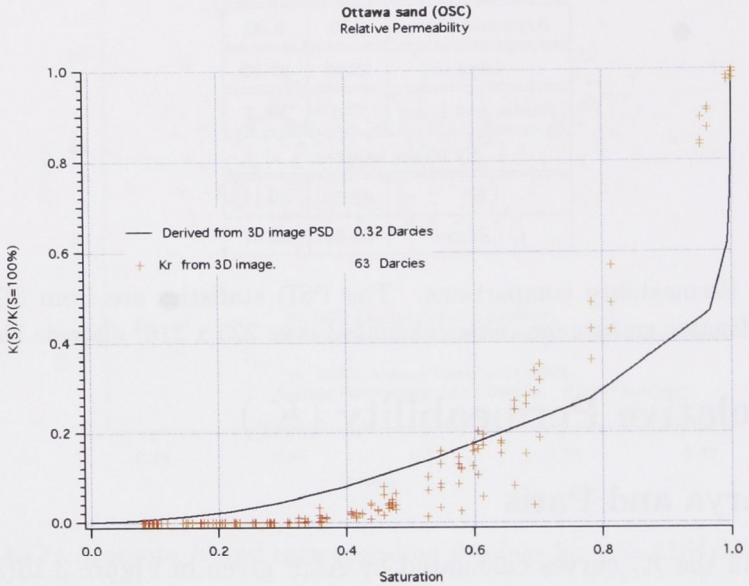

(a) Relative permeability from Arya and Paris, and 3D image analysis.

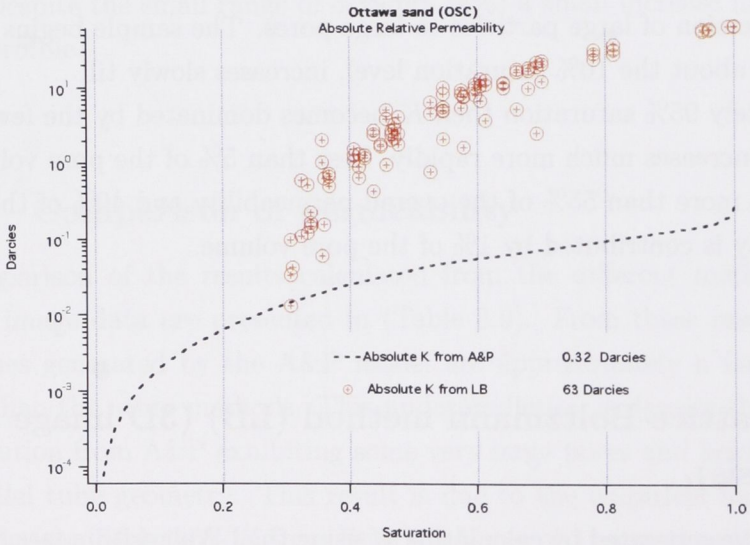

(b) Absolute relative permeability comparison from A and P, and LB calculation.

Figure 3.18: Relative permeability.

3.7.3 Comparison of K_r

The major difference between the A&P derived K_r curves and the lattice Boltzman calculation is the contribution to K at the higher saturation ranges (contribution of largest pores). The A&P curve predicts the 5% of larger pores contributes more than 70% of K. As reported in Section 3.6.3 and presented in Figure 3.18(b), absolute differences in K are significant therefore the permeability of the A&P model at all saturations is in poor agreement with direct calculations (Figure 3.18(b).

Chapter 4

LRC

4.1 Description

In this chapter we describe the analysis of a fluvial river sediment removed from an active riverbed using a vibro-core system mounted on a barge (2.2-2.5m depth interval) (See Section 2.1.2 (Tan et al., 2006). Retrieval using the vibro-core method was employed because the saturated unconsolidated nature of the material meant the drill could be slowly vibrated into the river bed with very little physical disturbance thus maintaining the natural structure and bulk density of the material. The retrieved $65mm$ diameter core was then extruded into a plastic sleeve using compressed air and stored (Figure 4.1(a)). A subsample was acquired from the $65mm$ core by pushing a $17mm$ diameter, $35mm$ long aluminium tube into the larger core (Figure 4.1(b)). Details of the sampling procedures and figures illustrating the methods are given in Section 2.1.4. The sample was then left to dry at ambient conditions for 2 weeks before imaging. Initial visual examination of the sample identified it as a clean homogenous quartz sand (Figure 4.1). This was confirmed by x-ray diffraction which identified the mineralogy as 80-95% quartz with up to 10% muscovite and $<2\%$ feldspar (Tan et al., 2006). Inspection of the particles under a microscope also appeared to confirm this (Figure 4.2).

After drying, x-ray tomographic imaging was undertaken on the sample. 3000 2D projections at 2048^2 were acquired for the tomogram. Details of the acquisition parameters and sample dimensions are summarised in Tables

4.1(a) and (b). A 2D slice through the tomogram is shown in Figure 4.3(a). The x-ray attenuation histogram (Figure 4.3(b)) is very clean and little filtering or edge enhancement is required for accurate phase separation. Upon close examination of Figures 4.1 and 4.3(a) it is clear that the subsampling of the core leads to a higher ϕ around the outside of the sample due to loosening of the material at the tube interface. To minimise these artefacts and allow for investigation of the 'undisturbed' regions of the sample, a subset of the image is chosen which lies 2-3 grains inside the tube volume (grey centre in Figure 4.3(a)). The resultant dataset defined as the fiducial volume is a cylindrical subset 1860 voxels in length with a radius of 700 voxels. Figure 4.3(c) shows the cross section through this subset. All calculations of pore/grain structure and flow properties performed on the image in the remainder of this chapter are undertaken on this volume.

Segmentation of the tomograhic dataset into 2 discrete phases, void and solid was undertaken on the fiducial volume. From an inspection of Figure 4.3(b) it can be seen that the dataset shows a very clean, easily binarised distribution of values with 2 peaks, one corresponding to the void phase (peak at approximately 4,700) and one corresponding to the solid phase (peak at approximately 8,200). The resulting binary dataset obtained from the grey scale image (Figure 4.3(c)) is given in Figure 4.3(d). Upon initial visual inspection of the 2D slice (Figure 4.3(d)) we note that this sample consists of moderately to poorly sorted, sometimes elongated particles. The distribution of grains is generally homogenous; larger particles appear to be distributed randomly throughout the FOV and there are no obvious aggregates of smaller or larger grains.

(a) Acquisition parameters	
sample distance	$410mm$
camera length	$1500mm$
voltage	80kV
beam current	$200\mu A$
exposure time	20 sec
filter	$3mm$ silica

(b) dimensions		volume
tube height	$35mm$	$7.39cm^3$
tube inner radius	$8.2mm$	
image volume	2048^3 voxels	$6.56cm^3$
fiducial radius	700 voxels	
fiducial height	1860 voxels	$2.22cm^3$
voxel size	$(9.18\mu m)^3$	

Table 4.1: (a) Tomogram acquisition parameters. (b) Sample size and image specifications. (see Figures 4.1 and 4.3)

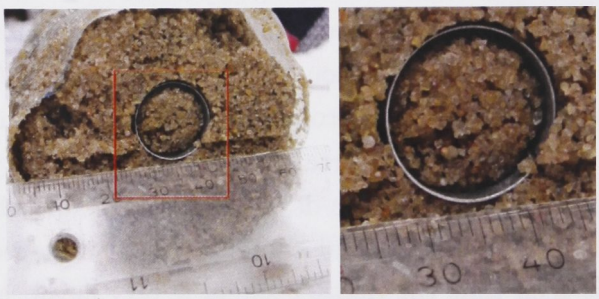

(a) (b)

Figure 4.1: LRC regolith sample from a depth of 2m in an active riverbed. (a) Subsampling the core sample by inserting an Al tube into the larger core. (b) Inset from (a) showing tube volume unfilled with sample leading to an increased porosity value.

4.2 Physical Measurements

4.2.1 Density and Porosity

After imaging of the sample, density (ρ) and porosity (ϕ) were calculated from measurements of weight and volume. The sample was dislodged from the Al tube as a loose grain pack and dried at 105^0C for 24hrs. The sample then weighed 8.8354g. The particle volume as measured by He displacement was 3.3469cc. Particle density is therefore 2.6399g/cc. This value is reasonable; sufficiently close to the quartz (2.65g/cc), which accounted for up 80-95% of the grains, the remaining 10-15% of the sample, muscovite and feldspars, have densities of 2.76-3.1g/cc and 2-2.4g/cc respectively (Berkman, 1995).

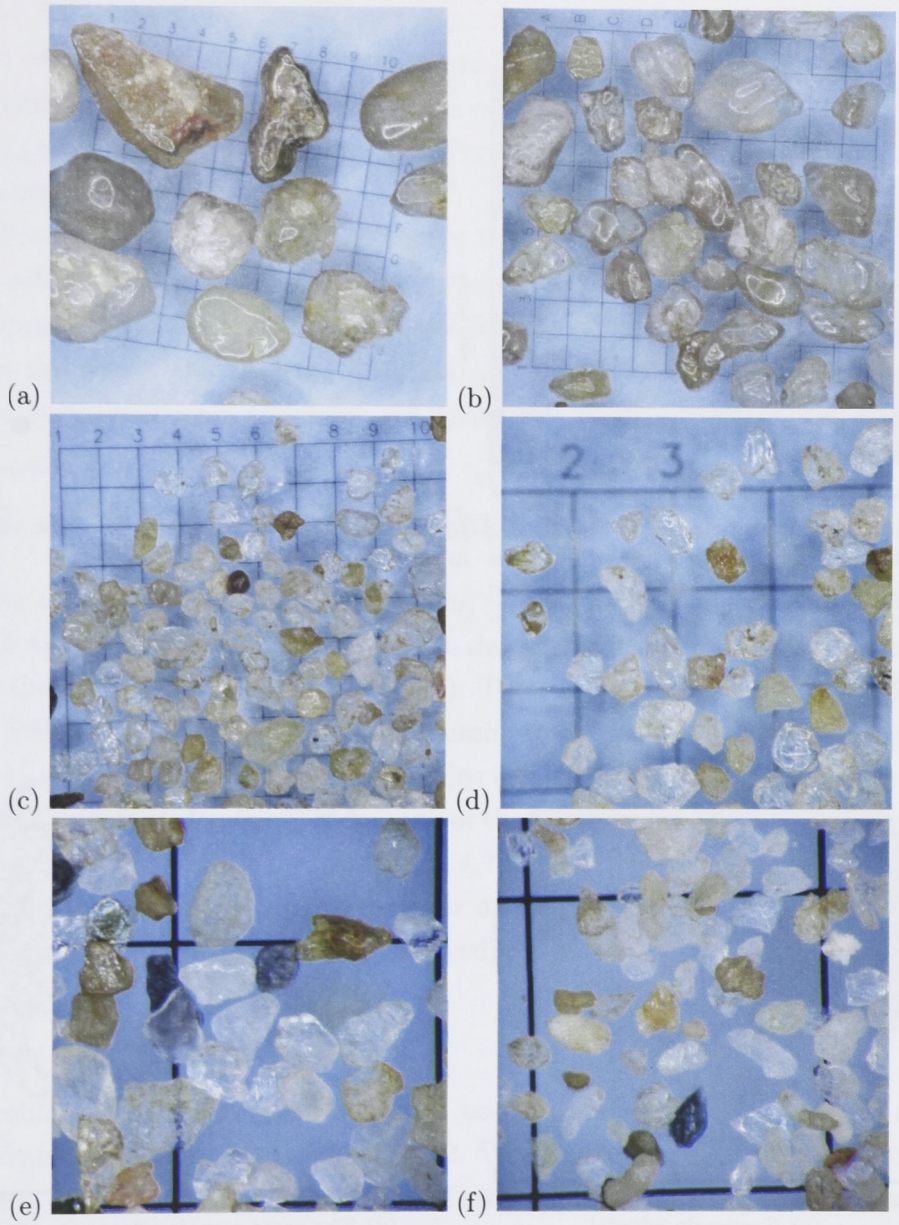

Figure 4.2: Grain morphology and size from microscope. (a) $2mm$ grain fraction. (b) $1mm$ grain fraction. (c) $0.5mm$ grain fraction. (d) $0.250mm$ grain fraction. (e) $0.125mm$ grain fraction. (f) $0.063mm$ grain fraction. The grid is $1cm^2$, the numbered small squares are $1mm^2$.

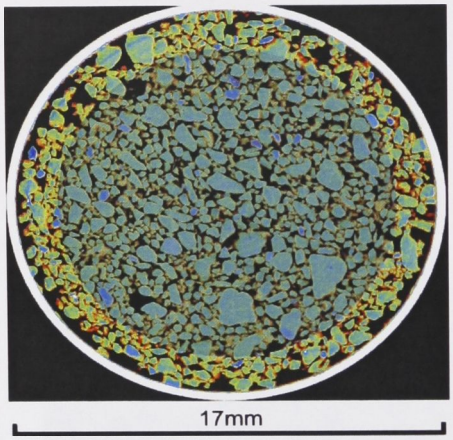

(a) X-ray intensity map of the sample with the fiducial section greyed out.This fiducial region is chosen 2-3 grains inside the Al tube volume to minimise the artefacts associated with loose particles at the boundary.

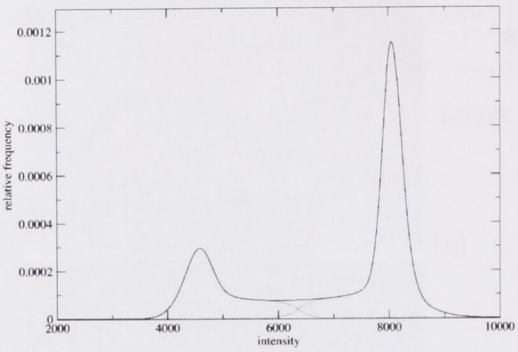

(b) X-ray attenuation histogram of the voxels in the fiducial volume.

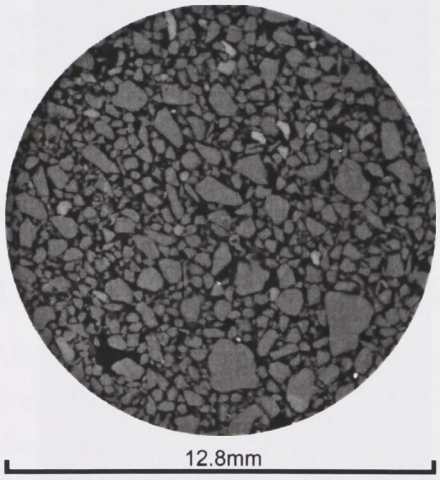

(c) Greyscale fiducial

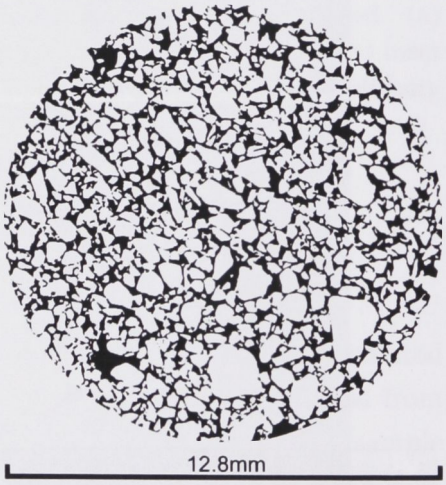

(d) The same sample after segmentation into void and granular phases

Figure 4.3: Fiducial and segmentation.

From the tube volume ($7.39cm^3$), the porosity and bulk density are found to be 54% and 1.198g/cc respectively. As described previously these are poor estimates as they are compromised by the subsampling method which introduces void space at the ends and along the edges of the subsampling tube (recall Figures 4.1 and 4.3(a)). This additional pore space leads to an overestimation of porosity.

Porosity was also calculated directly from the 3D image. Use of the fiducial subset illustrated in Figure 4.3 minimises the edge and end effects which compromise the porosity based on the full tube volume. Porosity obtained from the image was 36.69%. This is a realistic value for an unconsolidated sand pack (Domenico and Schwartz, 1998).

4.3 Particle Size Distribution (PSD)

Sister core material obtained according to the method outlined in Section 2.1.4 was used to obtain PSD using the sieve/hydrometer (see Section 2.3.1), and the LLS method (see Section 2.3.2). These distributions are compared to the PSD obtained directly from measurement on the 3D image (see Section 2.3.4). A visual examination of particles using a microscope was performed on small subsets of particles from each of the sieves used in the sieve analysis. These subsets are presented in Figure 4.2. Visual inspection of these particles indicates most are slightly angular and somewhat elongated. Particles ranging from $63\mu m$ to $2mm$ are observed.

4.3.1 Sieve / hydrometer

A volume of approximately 36cc was used for sieve analysis. Results are presented in Figure 4.5(a) and Table 4.2. We observe that 99% of the particles have a diameter greater than $63\mu m$. This sample is therefore classified as a sand. The average volume weighted particle size is $410\mu m$. The median was $430\mu m$ and the mode fell in the 250-500μm range.

4.3.2 Laser Light Scattering (LLS)

0.49cc of material was used for the LLS analysis. PSD data was obtained from the Particle and Surface Sciences laboratory (Figure 4.5(b)). The sample was found to be 0.5% clay, 2.1% silt and 97.4% sand, with an average volume weighted particle diameter of $711\mu m$. It is therefore classified as a sand. A summary of the distribution is given in Table 4.2.

4.3.3 3D Image Analysis

PSD from the 3D image was based on the phase separated image of the fiducial volume presented in Figure 4.3(d). Using the process outlined in Section 2.3.4, 92,327 individual particles in the binary dataset are labelled. A 2D slice through the labelled 3D dataset is presented in Figure 4.6. As the 3D dataset has a voxel size of $9\mu m$, we only measure particles on the order $\geq 20\mu m$ and cannot resolve the small percentage (<3%) of silt/clay observed in the sieve and LLS distributions. This particle volume is not lost; the smallest particles remain unresolved as discrete entities but are incorporated into the solid phase as surface roughness on larger particles (see Figure 4.4).

PSD calculated from the 3D image allows a measurement of every individually identified particle in the imaged volume. This entire dataset is presented in the cumulative volume frequency trace of Figure 4.5(c). This data was rebinned to reflect the Udden-Wentworth scale. Analysis of this data yielded a volume weighted particle size distribution with a mean of $573\mu m$, and median and mode of $456\mu m$ and 354-$398\mu m$ respectively. The largest particle in the distribution was found to be $1873\mu m$ in diameter.

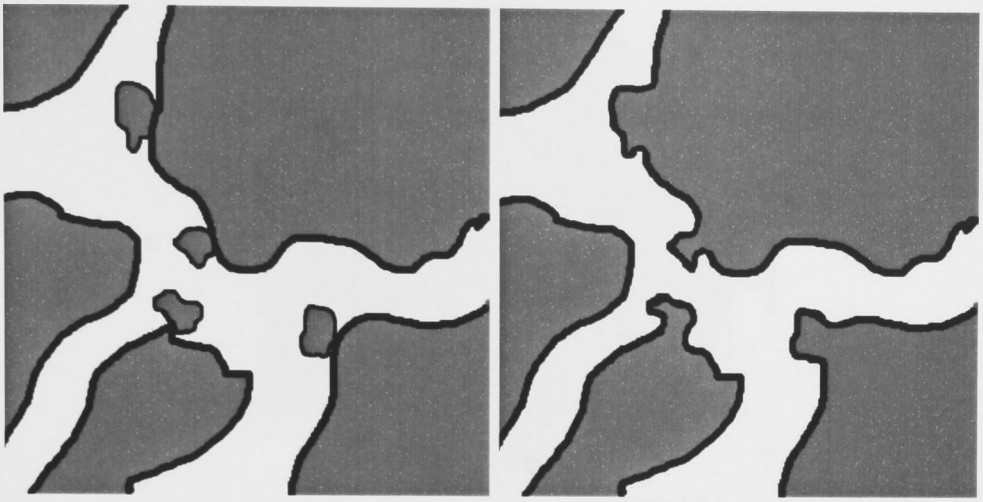

(a) (b)

Figure 4.4: Inability to characterise small particles; (a) shows an image of 5 large and 4 small discrete particles. (b) shows how the 4 smallest particles, too small to be resolved as discrete entities, are incorporated into the solid phase as surface roughness on larger particles.

Method	cm^3	% clay	% silt	% sand	Volume weighted diameter μm		
	Sample	<4	4-63	>63	Mean	Med.	Mode
Sieve	≈36.55	0	.5	99.5	410	430	250-500
Laser	0.49	0.5	2.1	97.4	711	630	1265-1788
X-ray CT*	2.22	0	<1	>99	573	456	354-398

Table 4.2: Particle size distribution from 3 different analytical techniques. ** no data on individual particles less than ≈30μm in diameter due to voxel size of 9.18μm.*

4.3.4 Comparison

Figure 4.7 compares the PSD from sieve, LLS, and 3D image analysis. The sieve and 3D image data are in very good agreement. Relative to the other

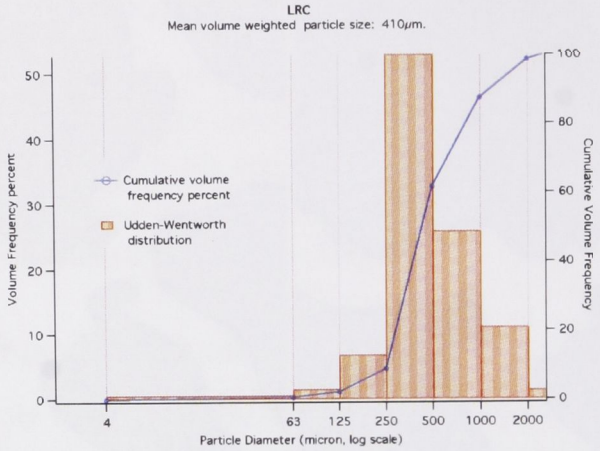

(a) PSD from sieve/hydrometer analysis.

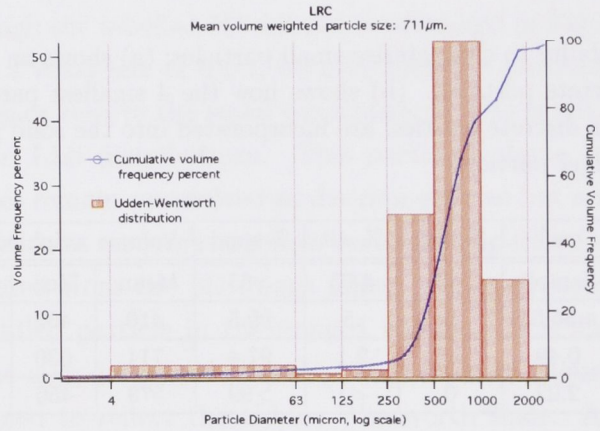

(b) PSD from Saturn Digisizer 5200 LLS analysis.

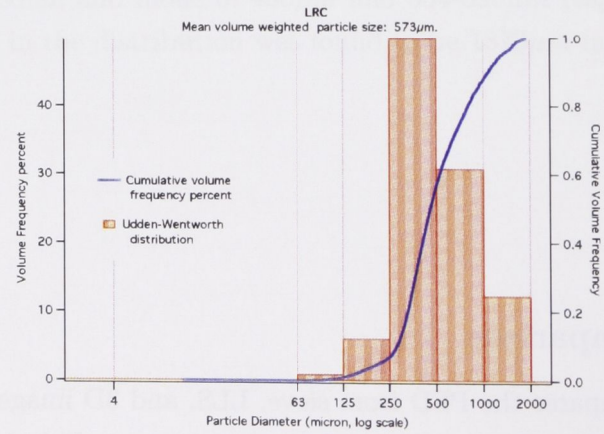

(c) PSD from analysis of the 3D image.

Figure 4.5: Distribution of grain sizes as measured by the sieve/hydrometer method, LLS and 3D image analysis.

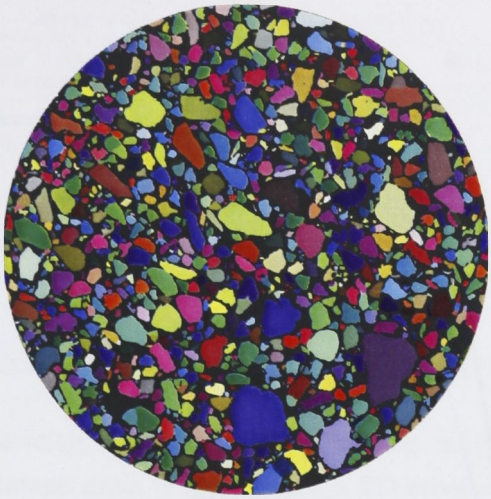

Figure 4.6: Individual particle partitioning of the 2D slice presented in Figure 4.3(d). Individually identified particles are colour coded. NB. all particles intersecting the boundary are excluded from the distribution.

measures, the LLS distribution overestimates particle size by around 30%. This result, as discussed in Section 3.3.4, is to be expected, particularly for samples where particles deviate from a spherical shape as they do in this case. A comparison of mean particle size as previously discussed in Section 3.3.4 we see $PSD_{sieve} < PSD_{3Dimage} < PSD_{LLS}$. This ratio; 1:1.39:1.73 is similar to that obtained for the Ottawa datasets and is again a good approximation of the long, intermediate and short axis (the Zingg ratio) as measured on the 3D image (see Section 4.4.2)(Table 4.3). The mean values of the short and long axis from the image data do not directly correspond to sieve and LLS data respectively but slightly underestimate the corresponding experimental data. This may be due to different sampling. The image data does not include particle sizes $>2mm$ which are noted in the sieve and LLS data.

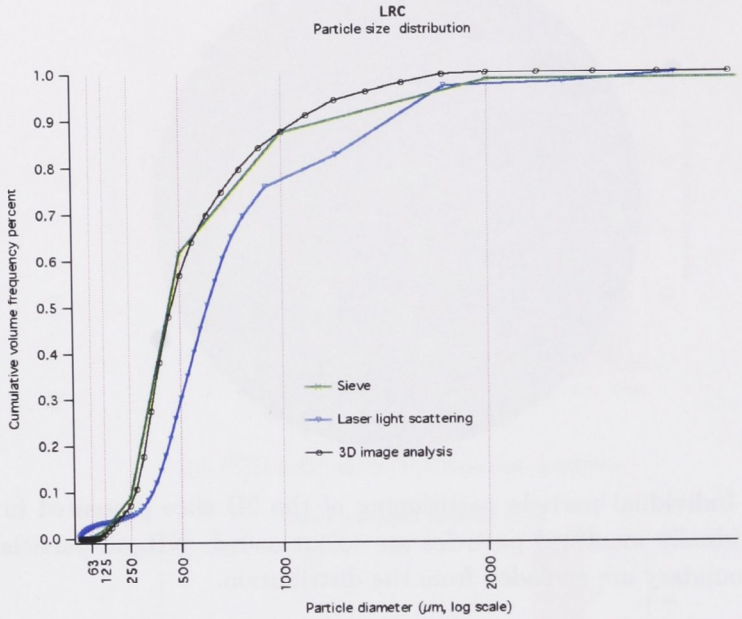

(a) PSD from 3D image, LLS and sieve analysis.

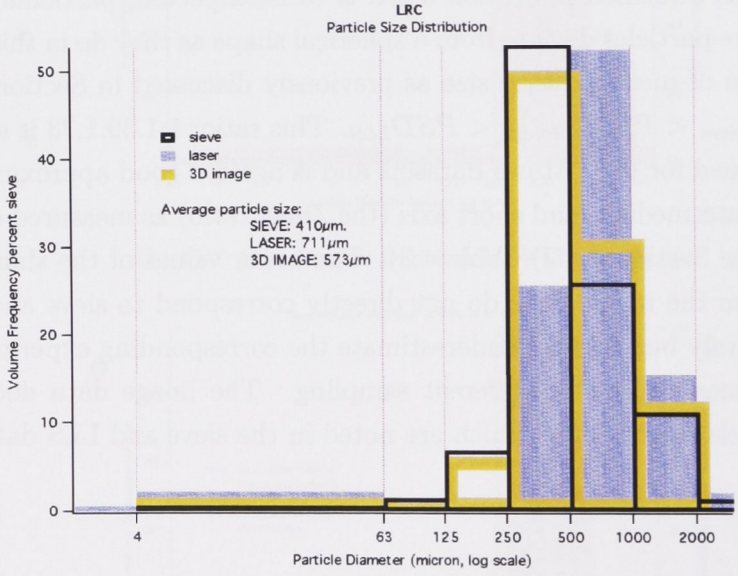

(b) Data binned to reflect the Udden-Wentworth scale.

Figure 4.7: Comparison of the 3 methods used to determine particle size distribution.

Mean volume weighted measures (μm)				
Axis	Short	Intermediate	Long	ratio
	520	710	912	1:1.37:1.75
PSD	Sieve	3D image	LLS	ratio
	410	573	711	1:1.40:1.73

Table 4.3: Mean volume weighted particle size from the 3 different analytical techniques compared to the long intermediate an short axis dimensions.

4.4 Textural Analysis / Shape Parameters

In this Section sphericity, Zingg, and co-ordination number were all calculated from the 3D image data. Figure 4.6 is a 2D cross section through the 3D dataset showing some of the individual particles which were examined for shape characteristics.

4.4.1 Sphericity

Figure 4.8(a) presents the histogram for volume weighted MPS (see Section (2.4.1)). From this plot it can be seen the distribution has a volume weighted mean MPS of 0.75 with 50% of the particles in the range 0.7 and 0.82, indicating most of the particles are in the 'Compact' range; relatively high sphericity (see Figure 2.12(c))(Table 4.4). There is no dependence upon particle volume; the number weighted average sphericity is the same as the volume weighted average. Examination of Figure 4.2 would appear to indicate a sphericity value lower than the reported 0.75.

4.4.2 Zingg

The Zingg ratio is calculated for all particle sizes and for each of the discrete Udden-Wentworth particle size fractions according to the method outlined in Section (2.4.2) and presented in Figure 4.8(b). Averaged over all particles we obtain mean I/L = 0.78 and mean S/I = 0.76. These values indicate the majority of particles can be classified as equant. This is consistent with the sphericity analysis. In Table 4.4 and Figure 4.8(b) we show the variation

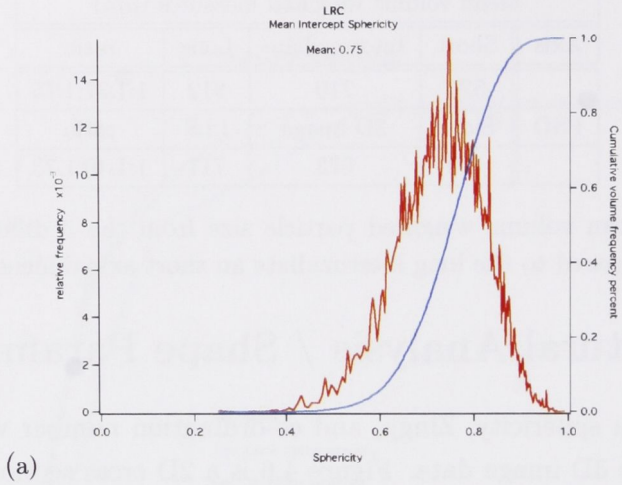

(a)

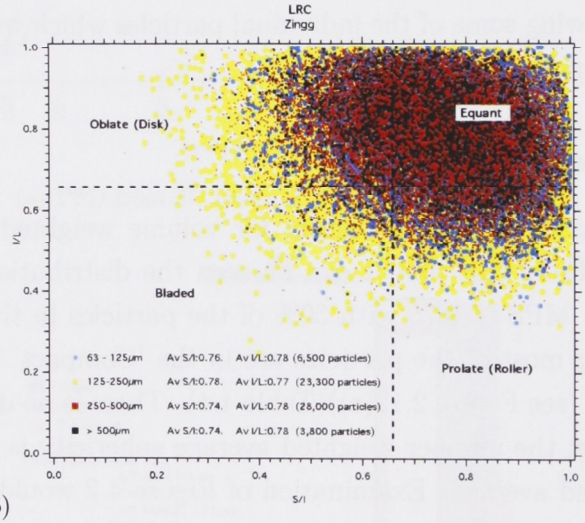

(b)

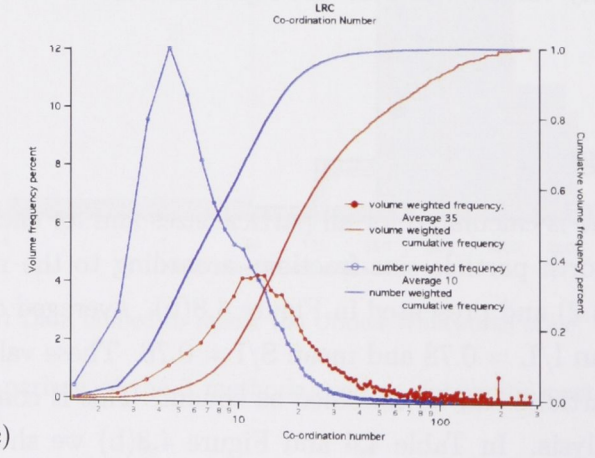

(c)

Figure 4.8: Shape parameters. (a) Mean intercept sphericity and (b) The Zingg ratio of long, intermediate and short axis of individual particles measured in the 3D tomogram. Colour is associated with particle size. (c) co-ordination number. Both the number and volume weighted datasets are presented.

of S/I and I/L values as a function of individual particle sizes. All mean values are consistent (Table 4.4). In Figure 4.8(b) we also note a broader range of particle shape for smaller particle size. Again the classification of particles as equant is perhaps surprising given the visual inspection of Figure 4.2. However, the number of particles in Figure 4.2 is small and the perceived variation may be due to sampling.

4.4.3 Co-ordination Number (Z)

Figure 4.8(c) is the volume weighted histogram for Z calculated for each individual particle. The volume weighted mean Z is 35, much larger than the number weighted mean of 10. This indicates Z significantly increases with particle volume. Large particles with a Z value of >200 are observed. This data is presented in Table 4.4. This large Z value is indicative of a more poorly sorted material (recall Figure 2.13). The characteristics of this sample contrast markedly with the Ottawa sand samples which exhibit a much tighter distribution of Z (recall Table 3.4). Figure 4.9 is a small subsection ($\approx 0.5mm^3$) of the particle contact network used to calculate Z. It shows the spatial distribution of particles as nodes and the contacts with other particles as connecting bars. The relative volume of each particle is indicated by the size of the node. It can be seen that the larger nodes exhibit a greater number of neighbouring particles. From this Figure we observe that generally the large particles are in contact with many smaller surrounding particles and these larger highly connected particles are not adjacent to other highly connected larger particles.

4.4.4 Sorting

Sorting is determined using equation 2.5 from Section 2.5.1. Percentile values used to calculate the sorting coefficient can be found in Table 4.4. For this sample the calculated sorting value is $0.78\phi_u$ signifying that it is a moderately sorted sample according to the classification of Folk and Ward (1957)(see Table 2.1). In conjunction with Z, above, this sample would be described

Figure 4.9: Network for the particle phase of the sample. Spheres are the particle centres. Size is a relative indication of the size of the particle represented. Contacts are represented by sticks. This subset is 110x500x500 voxels.

as a moderately sorted grain pack. Recalling Sections 3.4.3 and 3.4.4 we see OSC, is comparatively well sorted with a very low co-ordination. It is expected that these packing characteristics should have implications for the pore size distribution.

4.5 Pore Size Distribution

In this section we compare a number of pore size descriptors. PSD is converted to a pore size distribution using the A&P model. Pore-size distribution is also calculated directly from the 3D image using the covering sphere transform (CRT), via a simulated MICP experiment, and a calculation based on pore network descriptions. These distributions are then compared.

Zingg	Number of particles	Mean	
Long μm	61,827	912	
Intermediate μm	61,827	710	
Short μm	61,827	520	
63-125μm	6,520	0.76	0.78
125-250μm	23,365	0.78	0.77
250-500μm	28,116	0.74	0.78
>500μm	3,826	0.74	0.78
mean Zingg		0.76	0.78
Sphericity	61,827	0.75	
Z (volume weighted)	61,827	35	
Z (non-volume weighted)	61,827	10	
Z max	61,827	276.5	
Sorting ϕ_u	61,827	0.78	
$D_{84}\phi_u$	61,827	0.336	
$D_{16}\phi_u$	61,827	1.867	
$D_{95}\phi_u$	61,827	-0.240	
$D_5\phi_u$	61,827	2.409	

Table 4.4: Summary values for textural measures.

4.5.1 Arya and Paris Model (A&P) from Grains to Pores

PSD from sieve, LLS and 3D image analysis was converted to pore-size distribution using the A&P model (recall Section (2.6.1.1)). The porosity value used in the calculation of these distributions was the porosity value as calculated from the 3D image: 36.69%. Parameters used in the calculation were a = 2.478, b = 1.490 (from Table 2 in Figure 2.15), log c = 2.507 and x = 4.471 (from Table 3 in Figure 2.15). a and b are defined according to the textural class of the sample, which was sand. The log c and x parameters chosen are the values from Figure 2.15 corresponding to the highest percentage sand and lowest percentage clay as almost no clay was identified in the sample. The PTF is performed on all 3 PSD data sets for illustration; sieve, LLS and 3D image. A summary of these results is presented in Table 4.5 and Figure 4.10. From sieve the distribution of pore to particle sizes in the low to intermediate particle size range is approximately 4:1. Pore sizes associated with large particles are almost equant. Inspection of Figure 4.10 shows a little more than 30% of the pores have a radius of $100\mu m$ or more. $\approx$ 5% of the pore volume has a radius greater than $1mm$. The large pores are associated with the small fraction of large particles. The volume weighted mean pore radius for this distribution is $88\mu m$.

In the LLS data for small to intermediate particle sizes the pore to particle ratio is around 2:1 and the ratio of large particle to large pore is closer to 1:1. The volume weighted mean radius was $251\mu m$. The calculated pore volume with a radius of more than $1600\mu m$ (3% by volume) is calculated from the particle with a diameter $>894\mu m$ These particle sizes collectively account for less than 3 particles (n_i) in the A&P formulation.

The conversion from the image derived PSD again shows a strong increase in pore-size with the PSD. As with the sieve data the distribution of pore to particle sizes in the low to intermediate particle size range is approximately 4:1. Pore size associated with large particle size is almost equant. The volume weighted mean radius for this distribution is $171\mu m$.

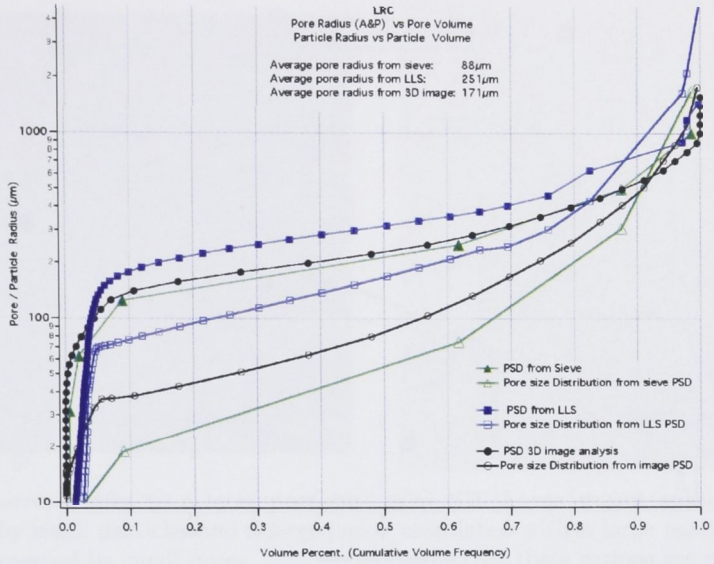

Figure 4.10: Pore size distribution converted from PSD obtained from sieve/hydrometer, LLS and 3D image analysis, using A&P.

4.5.2 Direct calculation from 3D Image Analysis

4.5.2.1 Covering Sphere Transform (CRT)

Figure 4.11 shows a pore size distribution from CRT (recall Section 2.3.3.1). Average pore radius was $46.15\mu m$, and only a small number of pores (<2%) exhibit pores sizes $>100\mu m$.

4.5.2.2 Simulated MICP (Capillary pressure)

Figure 4.11 shows the results of the simulated MICP experiment for the imaged core. This transform returned an average pore throat radius of $37\mu m$; slightly smaller than the $46.15\mu m$ returned from CRT. From the intrusion data and the subsequent shape of the curve, l_c was calculated to be $43\mu m$ (refer to Section 2.6.2.1 on page 42).

As with the Ottawa sand data a comparison of the CRT and MICP measures reveals that the larger pores present in the sample (40-$100\mu m$ range

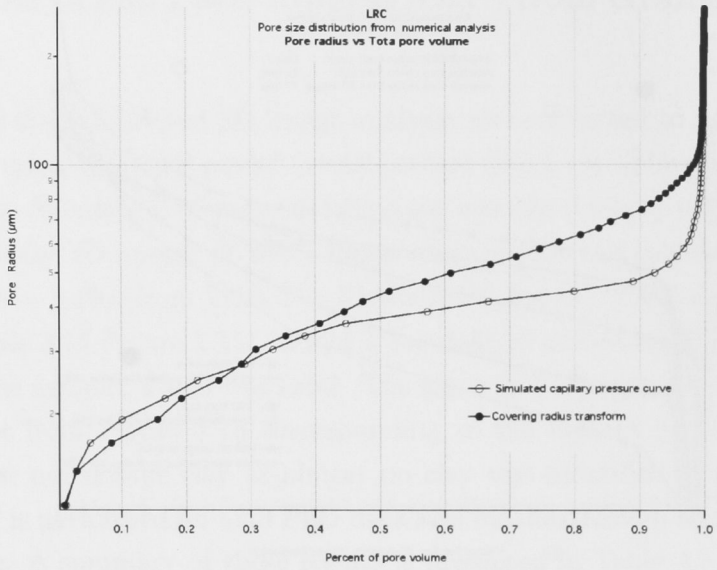

Figure 4.11: Pore size distribution from image analysis including a simulated capillary pressure curve and a covering sphere transform.

visible in the CRT data) are not captured by the MICP simulation due to smaller pores shielding larger pore volumes from Hg injection (recall Figure 2.16(c)).

4.5.2.3 Network pore-size distribution

The process involved in partitioning of the void phase into pore and throat is outlined in Section 2.6.2.2. A portion of a 2D slice through the partitioned volume is presented in Figure 4.12(a). The results of the partitioning process are presented as a small subset ($500 \times 110 \times 110$ voxels) of the 3D network in Figure 4.12(b). From this Figure we see a few randomly distributed vacant spaces presumably associated with large particles, surrounded by tightly packed networks of smaller pores. Moderate heterogeneity in the structure is obvious and notable when comparing to Figure 3.11(b) (Ottawa sand). Figure 4.12(c) and (d) give the pore and throat distribution curves. The pore to throat ratio is larger than that observed for Ottawa sand. The average pore radius is $67.5\mu m$ and the average throat radius is $24\mu m$ (see Table (4.5)).

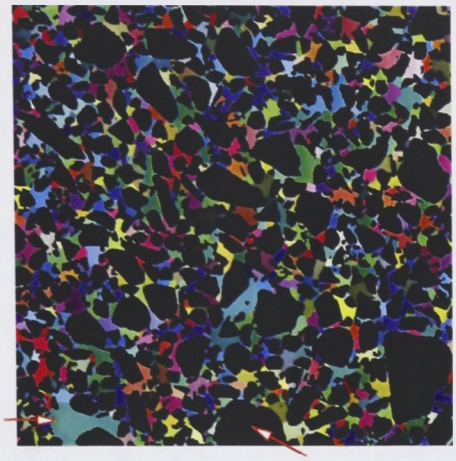

(a) Red arrows refer to a large pore surrounded by small particles and a large particle surrounded by small pores.

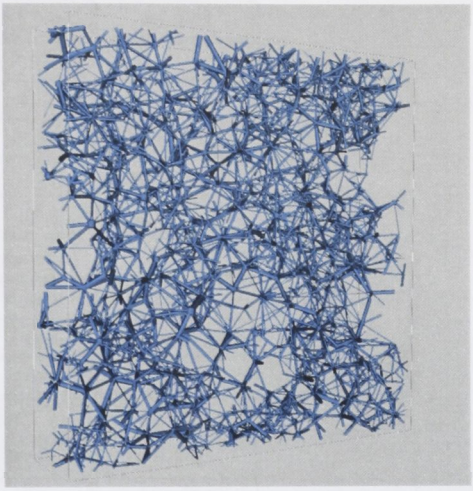

(b) NB. Large vacant spaces presumably associated with a large particles. It is notable that these regions are not adjacent to large pores.

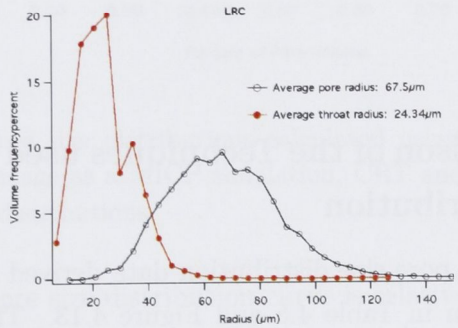

(c) Frequency percent of pore and throat radii volume weighted

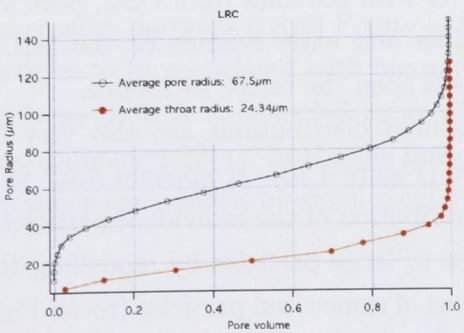

(d) Cumulative frequency percent of pore and throat radii volume weighted

Figure 4.12: Network analysis.

Method	cm^3	Volume weighted mean μm
A&P		
	Sample	Pore size
A&P Sieve	≈36.55	88.12
A&P Laser	0.49	241.09
A&P image	1.40	171.48
Image Analysis		
CRT*	1.40	44.90
Cap pressure*	1.40	36.06
l_c*	1.40	43
Network		
Pore*	1.40	67.50
Throat*	1.40	24.34

Table 4.5: Pore size distribution from all the different analytical techniques used to estimate/measure pore size used in this study.
** no data available for pore less than 9μm in diameter due to image resolution.*

4.5.3 Comparison of the Techniques used to obtain pore-size distribution

A comparison of the pore size distribution data derived from these different techniques are shown in Table 4.5 and Figure 4.13. The pore sizes calculated from A&P significantly overestimate pore radius relative to the directly measured values. A&P attribute more than 40% of the distribution to pores larger than $100\mu m$. As with the data from OSC, pore and throat from network analysis set upper and lower bounds on the MICP and CRT values. Most pores and throats span the range 10-$100\mu m$.

The directly measured distributions are also very flat in compared to the A&P distribution (Figure 4.13). It appears A&P fail to account for the disordered spatial distribution of the individual particles; the model directly attributes large pores to large particles by modelling the PSD as spatially discrete agglomerations of same sized particles (recall Figure 2.14). In reality the large pores are filled with the smaller particles. Few large pores are

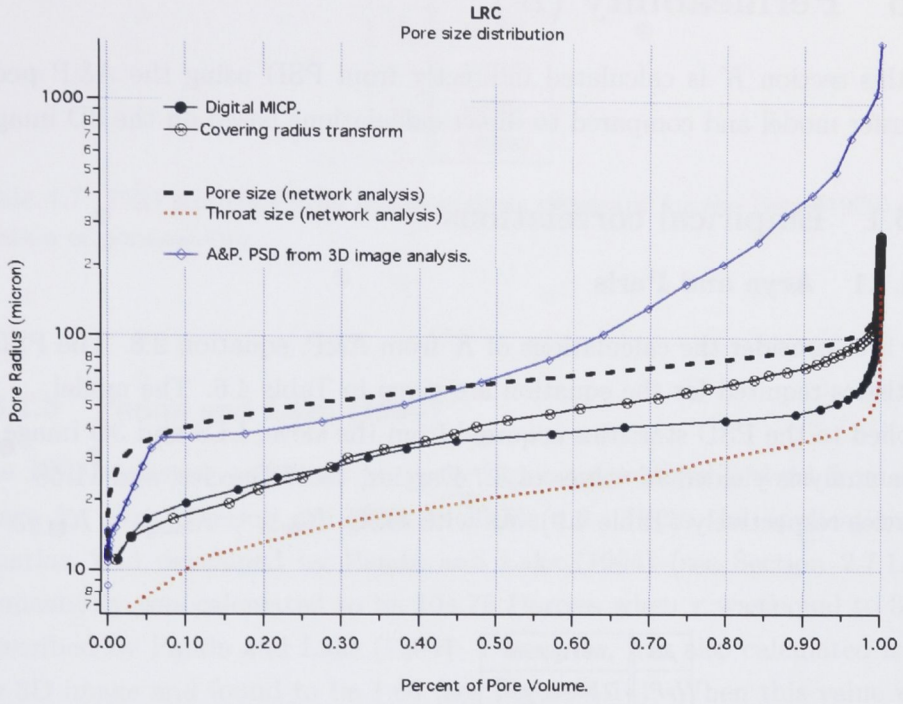

Figure 4.13: (a) Pore size distributions calculated using A&P (PSD from 3D image) and the 3D image as a MICP simulation, CRT and a network analysis of the pore and throat distributions.

observed and the pore size distribution curve is relatively flat (Figure 4.13). This effect is also illustrated by particle connectivity. In a well sorted sand particle co-ordination is ≈6 (eg. Ottawa); the value for Z is much larger for this sample. This larger value of Z is associated with the large particles being surrounded by many smaller particles (recall Figure (4.9)). This reduces the potential for big particles to be associated with big pores.

An example of a large particle surrounded by small pores can be found in the bottom centre of Figure 4.12(a). In the the bottom left of this Figure we note a large pore space surrounded by small particles.

4.6 Permeability (K)

In this section K is calculated indirectly from PSD using the A&P pedotransfer model and compared to direct calculations based on the 3D image.

4.6.1 Empirical correlations

4.6.1.1 Arya and Paris

We first consider the calculations of K from A&P, equation 2.8. The PSD statistics required for the equation are given in Table 4.6. The model applied to the PSD statistics acquired from the sieve, LLS and 3D image data analysis yielded K values of 8.7 Darcies, 45.47 Darcies, and 11.58 Darcies respectively (Table 4.9). As with OSC, $K_{\text{sieve}} < K_{\text{image}} < K_{\text{LLS}}$.

(a)

ρB	$1.671 g/cm^2$
ρP	$2.6399 g/cm^2$
ϕ	0.3669
a	-2.478
b	1.49
b	321.37
x	4.471
e	0.57983

(b)

Input PSD	K Darcies
Sieve	8.7
LLS	45.47
3D image	11.58

Table 4.6: (a) PSD statistics used for the A&P calculation of permeability. (b) Calculated K values.

4.6.1.2 Berg (1970)

K was also calculated from PSD statistics using equation 2.10 from Berg (1970) (see Section 2.7.1.2). The necessary statistics for the calculation are given in Table 4.7. K was 20.7 Darcies.

D	$0.409mm$
ϕ	36.69%
d_{10}	2.0267
d_{90}	0.0502
p	0.98825

Table 4.7: PSD statistics from image analysis necessary for the Berg (1970) calculation of permeability.

4.6.1.3 Panda and Lake (1994)

The PSD statistics and bulk property input parameters derived from the image for this equation are given in Table 4.8. From the application of equation 2.15 developed by Panda and Lake (1994) (see Section 2.7.1.3), permeability was calculated to be 104.76 Darcies when τ was equal to 3 as prescribed by Panda and Lake (1994). τ however, was also calculated from the 3D image and found to be 1.69 (see Figure 4.14). When this value was used K increased to 186.3 Darcies (see Table 4.9).

$\overline{Dp}$	$219.06\mu m$
ϕ	0.3669%
τ	3 & 1.6869
γ	1.7697
C_{Dp}	0.6490
σ	142.16
K in Darcies	104.76 & 186.3

Table 4.8: Particle size distribution statistics for the Panda and Lake (1994) calculation of permeability.

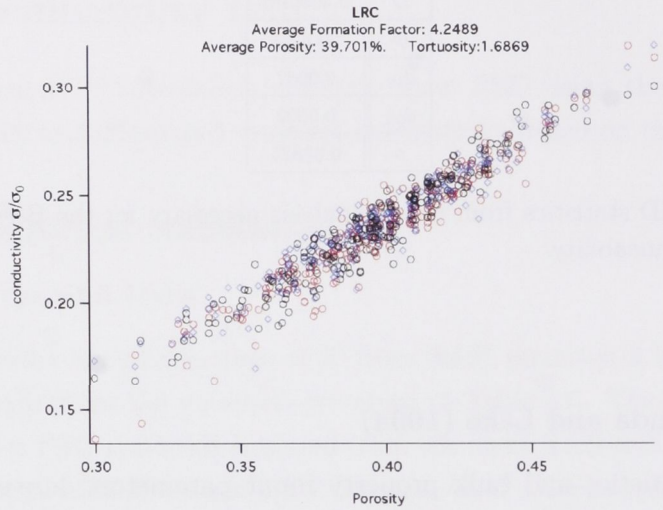

Figure 4.14: F calculated on 225 discrete 216^3 blocks. The average value is 0.23535.

4.6.2 3D Image Analysis

4.6.2.1 MICP Simulation (Capillary Pressure)

Permeability is calculated via equation 2.16 from Katz and Thompson (1986) (see Section 2.7.2). l_c is $43\mu m$ as calculated from the image (see Section 2.6.2.1), C =0.16. τ =1.6869 where $F = \frac{1}{\sigma/\sigma_0} = \tau/\phi$ from Figure 4.14(recall Section 2.7.2), and $\phi = 36.69\%$. This gives a prediction of $K = 64$ Darcies.

4.6.2.2 Lattice Boltzman

Permeability is calculated independently on 225 x 216^3 subset blocks taken from within the fiducial volume (see Section 2.7.3.1). The K and ϕ for each block is plotted in Figure 4.15. Porosity in the subsets range from 30-50% with an average permeability of 92 Darcies. K varied from 31.6 Darcies at low ϕ to 206.8 Darcies at high ϕ. The majority of values however fell within the range between 63 and 117 darcies. As the porosity range is 20% a distinct correlation between ϕ and K can be seen. The porosity range for this sample

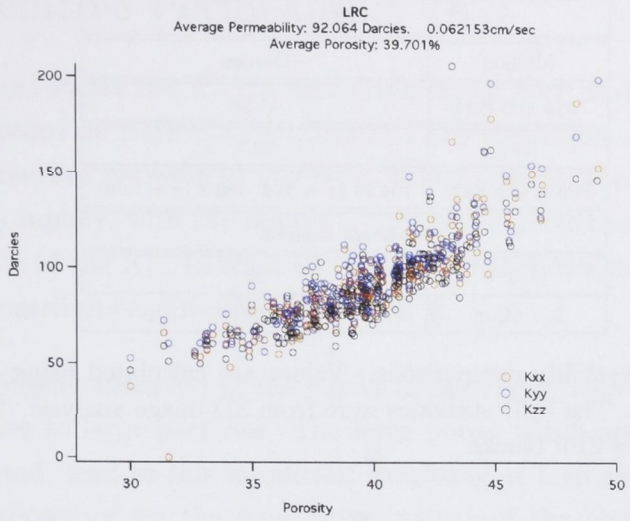

Figure 4.15: Permeability in Darcies calculated on 225 discrete 216^3 blocks using a lattice Boltzman algorithm.

is 5 times the porosity range we see OSC reflecting the heterogeneity at the grain scale.

4.6.3 Comparison of permeability

A comparison of the results calculated from the different methods based on 3D image data are presented in (Table 4.9). From these results we see that K from P&L and the calculation using l_c match the LB value within approximately 10-30%. The calculation using Berg underestimated the LB value by almost a factor of 4 and A&P underestimates by a factor of 8. This behaviour is consistent with the results we saw for the Ottawa samples where $K_{A\&P} < K_{Berg} < K_{P\&L} \approx K_{lc} \approx K_{LB}$.

LRC	
Method	Darcies
Arya and Paris	11.58
Berg	20.7
Panda and Lake	104.76 ($\tau = 3$) & 186.3 ($\tau = 1.69$)
3D image analysis	
LB*	92
l_c : $44\mu m$	64

Table 4.9: Permeability comparisons. Values are calculated using A&P, P&L, Berg, LB and l_c . The PSD statistics were from 3D image analysis. * denotes an average over 225 x 216^3 blocks.

4.7 Relative Permeability (K_r)

Figure 4.16(a) shows the K_r curves calculated by A&P and LB. The prediction based on A&P does not conduct any significant amount until saturation reaches between 70 and 90%. When saturation reaches this level K increases rapidly, with the largest 5-10% of the pores contributing as much as 95% of the K_r. In contrast data from LB shows the largest 60% of the pores contribute significantly to overall K.

The difference observed in the curves is associated with A&P weighting of large pores to large particles. The large pores, which are assumed to be well connected, lead to this significant weighting at high saturations. A&P makes no allowance for the true mixed nature of the pores and particles as illustrated in Figure 4.12(a-b). LB shows significant contribution from a range of pore sizes. Figure 4.16(b) shows the absolute value of K as a function of saturation. The error in the A&P prediction is quite large.

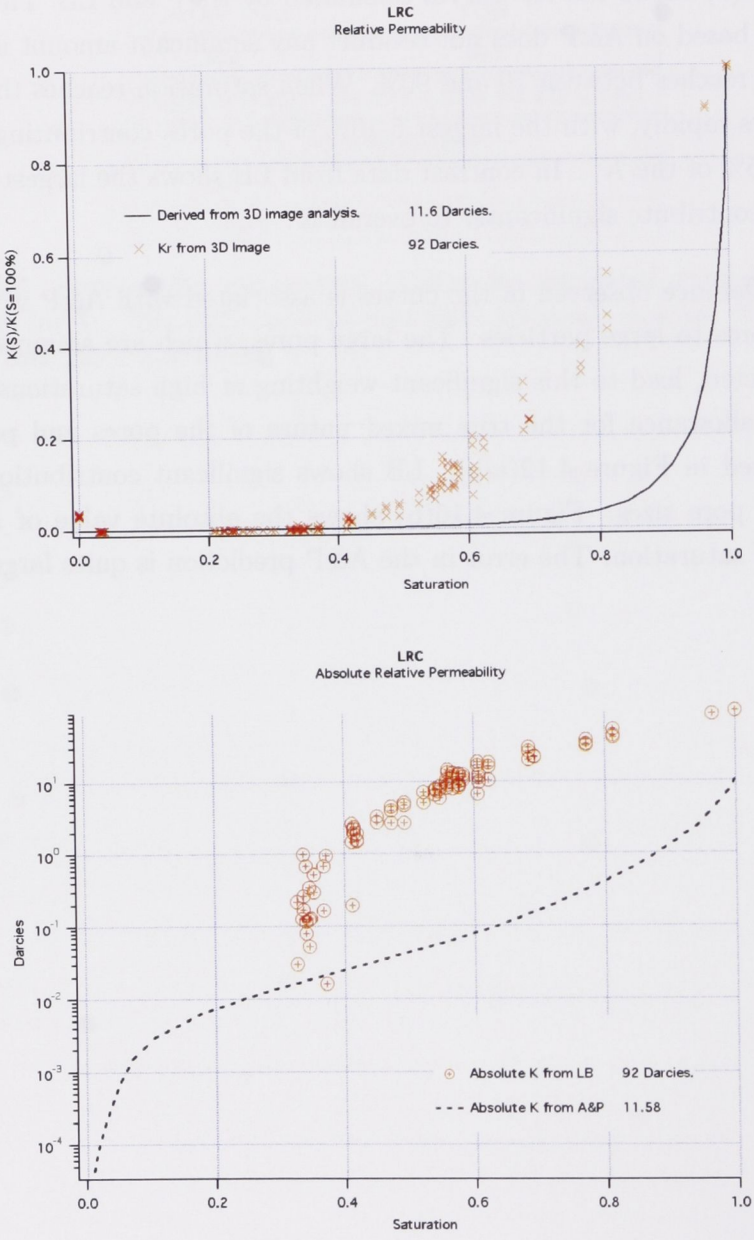

Figure 4.16: Relative permeability calculation comparisons.

Chapter 5

Rotorua

5.1 Description

In this section we describe the analysis of a coarse pumice sand from an aquifer (6.4-6.5m depth interval) in Rotorua, New Zealand obtained during a groundwater contaminant transport study. The sample was retrieved using the push tube coring method (See Section 2.1.3) because the saturated unconsolidated nature of the material meant the bit could be pushed into the ground with very little physical disturbance thus maintaining the natural structure and bulk density of the material. The retrieved $45mm$ diameter core (see Figure 5.1) was then extruded into a PVC tube and stored. A subsample was acquired by pushing a $17mm$ diameter, $35mm$ long aluminium tube into the larger core. Details of the sampling procedures are discussed in Section 2.1.4. The sample was then left to dry at ambient conditions for 2 weeks before imaging. Initial visual examination of the sample identified it as a coarse heterogeneous grain pack with various mineralogies represented (see Figures 5.1 and 5.2(a)).

Figures 5.2(b-e) are scanning electron microscope images of one of the larger particles from this sample. The particle was collected from the $2mm$ sieve after sieving. From these images we note the presence of intragranular porosity on multiple length scales. Voids on the order of $500\mu m$ to $<10\mu m$ in diameter are visible.

After the sample was dried x-ray tomographic imaging was undertaken.

3000 2D projections at 2048^2 were acquired for the tomogram. Details of the acquisition parameters and sample dimensions are summarised in Tables 5.1(a) and 5.1 (b) respectively. A 2D cross section through the tomogram is shown in Figure 5.3(a). Upon close examination of this Figure it is clear that the subsampling of the core leads to structural disturbance around the outside of the sample due to loosening of the material at the tube interface. To minimise these artefacts and allow investigation of the 'undisturbed' regions of the sample, a subvolume of the image is chosen to exclude the disturbed regions. This volume lies about 2-3 grains inside the tube volume (Figure 5.3(b)). This subvolume, defined as the fiducial volume, is a cylindrical subset 1960 voxels high with a radius of 824 voxels. All calculations performed on the image in the remainder of this chapter are undertaken on this volume.

Segmentation of the tomographic dataset into 2 discrete phases, void and solid was undertaken on this fiducial volume. The x-ray attenuation histogram (Figure 5.4) required careful visual consideration to attempt to accurately phase separate. Although 2 peaks are evident in the attenuation histogram, they are separated by a large number of voxels that are obviously neither void nor solid. The voxels may be associated with micro-porous regions as seen in Figure 5.2(b-e). The dotted lines show the chosen threshold used to segment the distribution into 2 discrete phases. Figure 5.5(a) and (b) is the fiducial volume and the resultant binary dataset respectively. Upon initial visual inspection of this Figure we note that this sample appears to be a poorly sorted grain pack. Particles of many shapes and sizes are represented. The distribution of particles is heterogeneous. From a close examination of Figure 5.5(b) we see that many of the larger intragranular voids visible in the SEM images of Figure 5.2(b-e) have been identified during the phase separation. Void space at the smaller length scales is most likely identified as solid phase due to the large voxel size and the limited image resolution. Although the resultant partitioning may underestimate the contribution of the micro-pores to the pore phase fraction, the loss of this pore space is not expected to impact on the prediction of flow properties which are dominated by the larger voids which are easily resolved.

(a) Aquisition parameters	
sample distance	$410mm$
camera length	$1500mm$
voltage	80kV
beam current	$200\mu A$
exposure time	20 sec
filter	$3mm$ silica

(b) dimensions		volume
tube height	$51mm$	$33.69cm^3$
tube inner radius	$14.5mm$	
image volume	2048^3 voxels	$37.54cm^3$
fiducial radius	666 voxels	
fiducial height	1920 voxels	$11.70cm^3$
voxel size	$16.35\mu m$	

Table 5.1: (a) Tomogram aquisition parameters. (b) Sample size and image specifications. (see Figures 5.2 and 5.5).

(a) 45mm diameter core in a PVC tube prior to subsampling.

Figure 5.1: Coarse pumice sand from Rotorua NZ.

5.2 Physical Measurements

5.2.1 Density and Porosity

Density (ρ) and porosity (ϕ) were calculated from measurements of weight and volume. A sister sample was dislodged from an Al tube as a loose grain pack and dried at 105^0 C for 24hrs. The sample weighed 32.01g. The particle volume as measured by He displacement was 13.70cc. Particle density is therefore 2.34g/cc. This value is reasonable as pumice is a natural, complex silicate containing approximately 70% silica in which other oxides (mostly (aluminium ($\approx$12%)) are dissolved (Allaby and Allaby, 1999).

From the inner tube volume ($27.08cm^3$ (height $41mm$ radius $14.5mm$)), the porosity and bulk density are found to be 49.41% and 1.18g/cc respectively. As described previously these are potentially poor estimates as they are compromised by the subsampling method which introduces void space at the tube sample interface visible in Figures 5.5(a) and (b) and Figure 5.6. It is likely that this additional pore space has lead to an overestimation of porosity.

Porosity was also calculated directly from the 3D image. Use of the

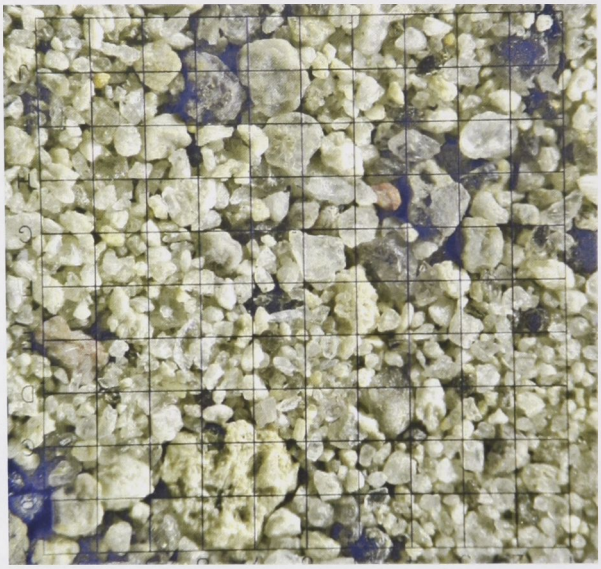

(a) Disaggregated constituent particles. Grid squares are 1mm x 1mm.

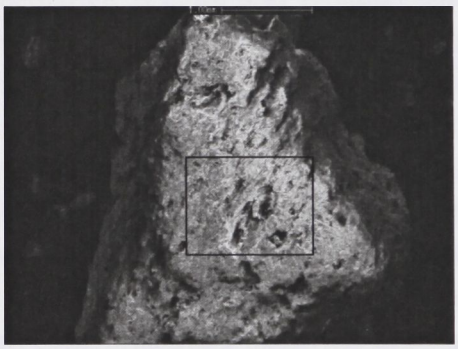

(b) SEM image of a pumice particle from the Rotorua sample. The scale bar at the top of the image is 1mm. The boxed section is enlarged in (c).

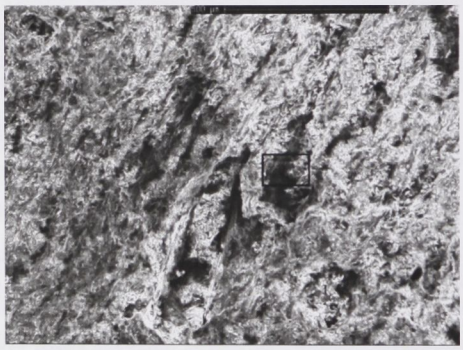

(c) The boxed section from (b). The scale bar at the top of the image is 0.5mm.

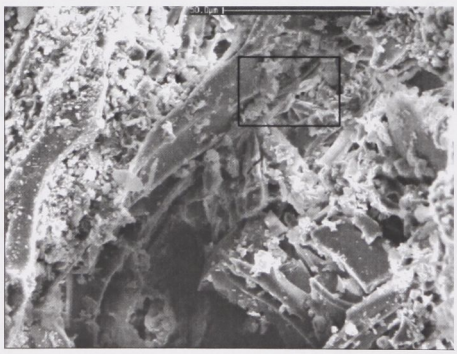

(d) The boxed section from (c). The scale bar at the top of the image is 0.05mm.

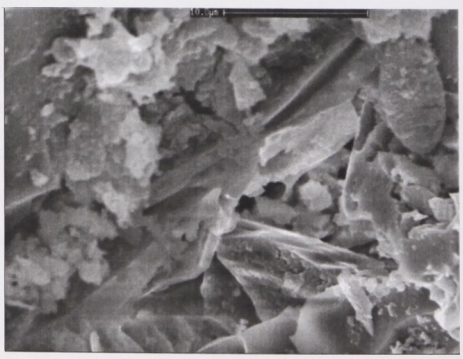

(e) The boxed section from (d). The scale bar at the top of the image is 0.01mm.

Figure 5.2: Coarse pumice sand from Rotorua NZ. (b-e) show intragranular porosity at different length scales.

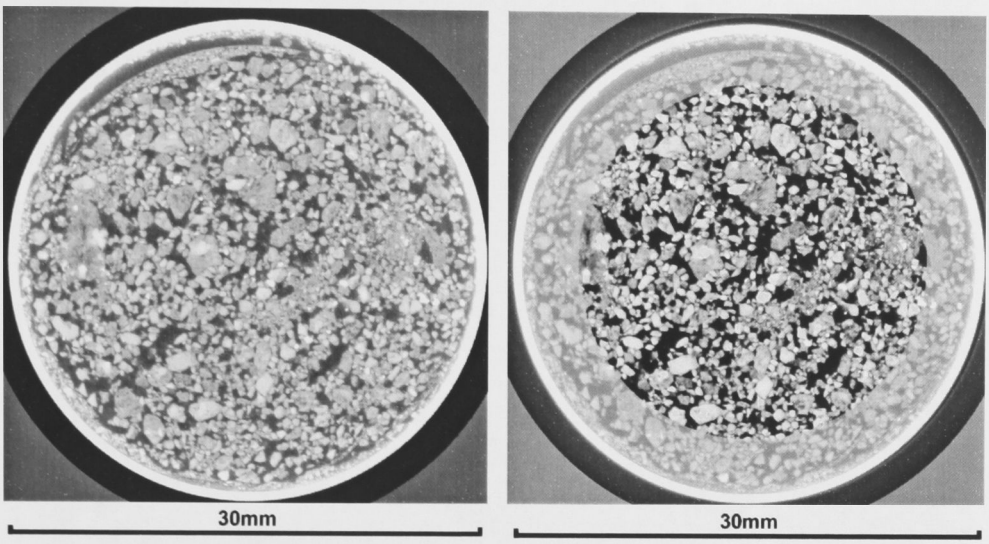

(a) 2D cross section through the cylindrical tomographic dataset.

(b) The choice of a fiducial subvolume excluding the Al tube and the outer regions where disturbance close to the tube is evident. The excluded image portion is greyed out.

Figure 5.3: Fiducial and segmentation.

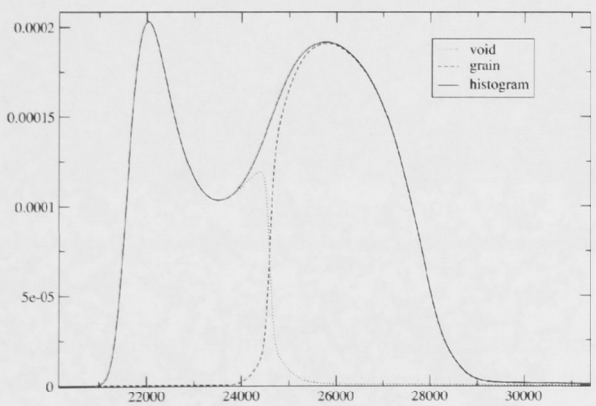

(a) X-ray attenuation histogram of the voxels in the fiducial volume.

Figure 5.4: X-ray attenuation histogram of the voxels in the fiducial volume.

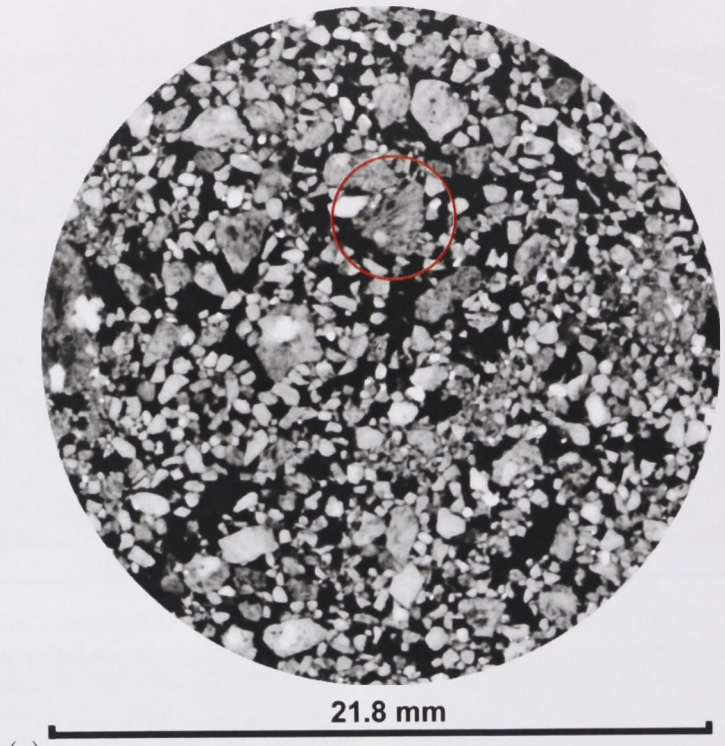

(a)

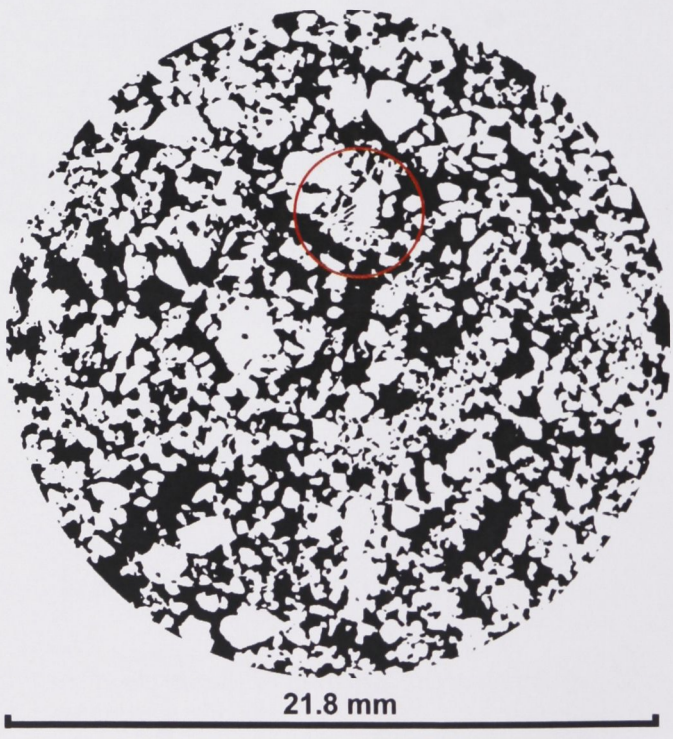

(b)

Figure 5.5: (a) 2D cross section through the fiducial volume and (b) the binarised segmentation of the fiducial volume. Note the intragranular voids visible in the particle highlighted by the red circle; the larger voids are identified in the image.

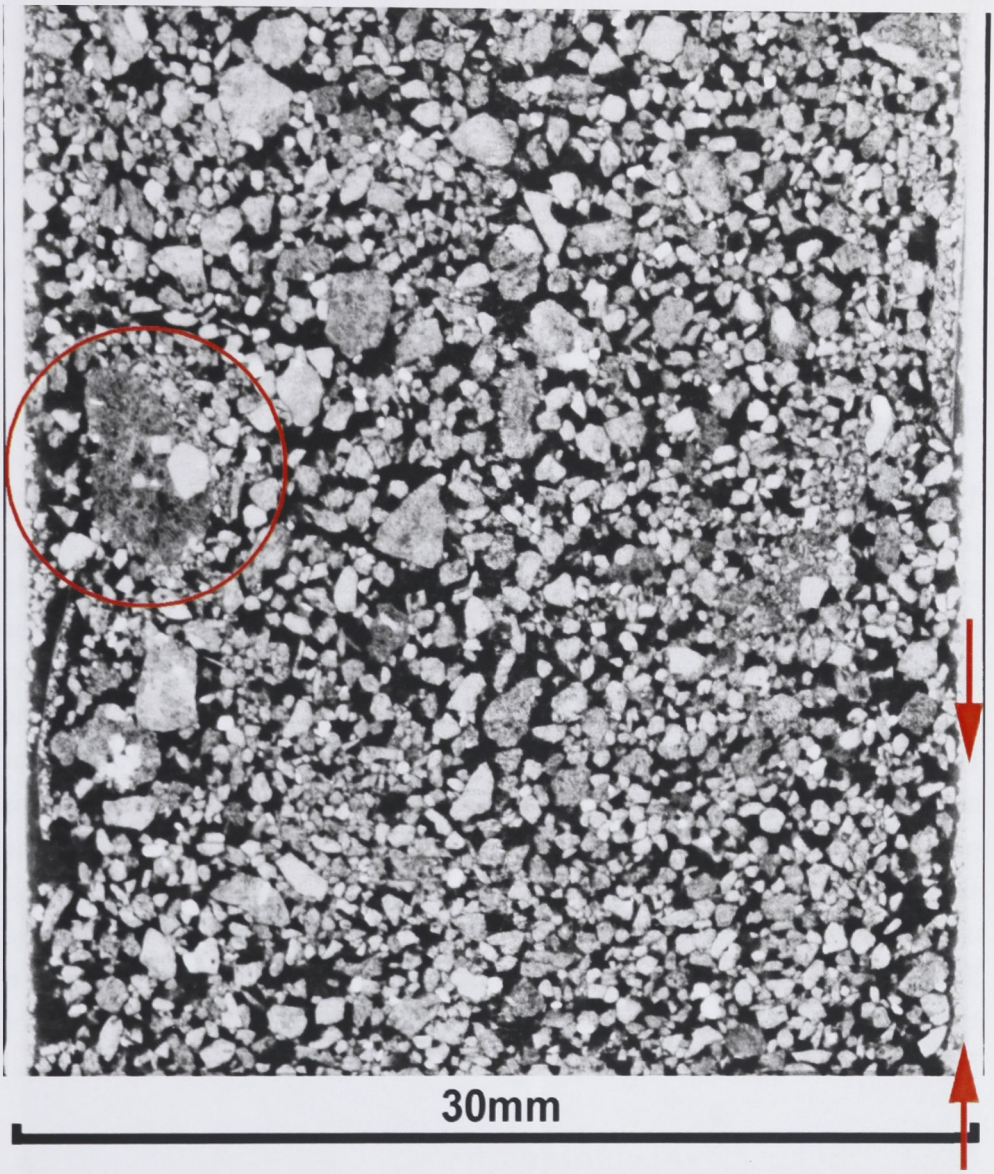

Figure 5.6: A 2D z direction slice through the unsegmented cylindrical 3D image. NB. The large particle, delineated by the red circle, contains intragranular voids indicative of pumice. This particle is also an example of a very large particle ($>5mm$) (see text on page 128). Poor sorting and strong heterogeneity is clear. Note also the presence of a layer delineated by the red arrows towards the bottom of the image that contains fewer large particles than other regions.

fiducial subset illustrated in Figure 5.5(b) minimises the edge effects which compromise the porosity based on the full tube volume. Porosity from the segmented fiducial volume was 43.6%. Due to the voxel size of the image intragranular porosity associated with pumice (see Figure 5.2 (b-e)) may not have been resolved in the tomographic data leading to an underestimation of porosity. The difference in the estimation of porosity from the image data versus the tube volume leads to reasonably tight bounds on the actual porosity.

5.3 Particle Size Distribution (PSD)

The PSD of the sample is measured directly on the 3D tomographic image (see Section 2.3.4). The sample was removed from the Al tube after imaging and analysed by LLS (see Section 2.3.2). LLS was performed on 10 subsets removed from the tube in sequential $5mm$ sections. Sister core material was used for measuring PSD using the sieve/hydrometer method (see Section 2.3.1), and a separate section taken from $50cm$ further down the core at the 7.3m depth interval was also analysed using the sieve hydrometer method for comparison. A visual examination of the particles using a microscope was performed on small subsets of particles from each of the sieves used in the sieve analysis. These subsets are presented in Figure 5.7. Visual inspection of these particles indicates most are quite angular but maintain a spheroidal like shape with more prolate particles in the smaller fractions. Particles less than $63\mu m$ and greater than $3mm$ in diameter were identified. From Figures 5.5 and 5.6 poor sorting appears to be a feature.

5.3.1 Sieve / hydrometer

A sister core volume of approximately 40cc was used for sieve analysis. Results are presented in Figure 5.8(a) and Table 5.2. A 1% clay fraction and 4.5% silt fraction was identified. 95% of the particles by volume however, are greater than $63\mu m$ (sand), and approximately 5% of the sample volume was retained on the $2mm$ sieve. From visual inspection of individual particles using a microscope particles on the order of $6mm$ in diameter were identified.

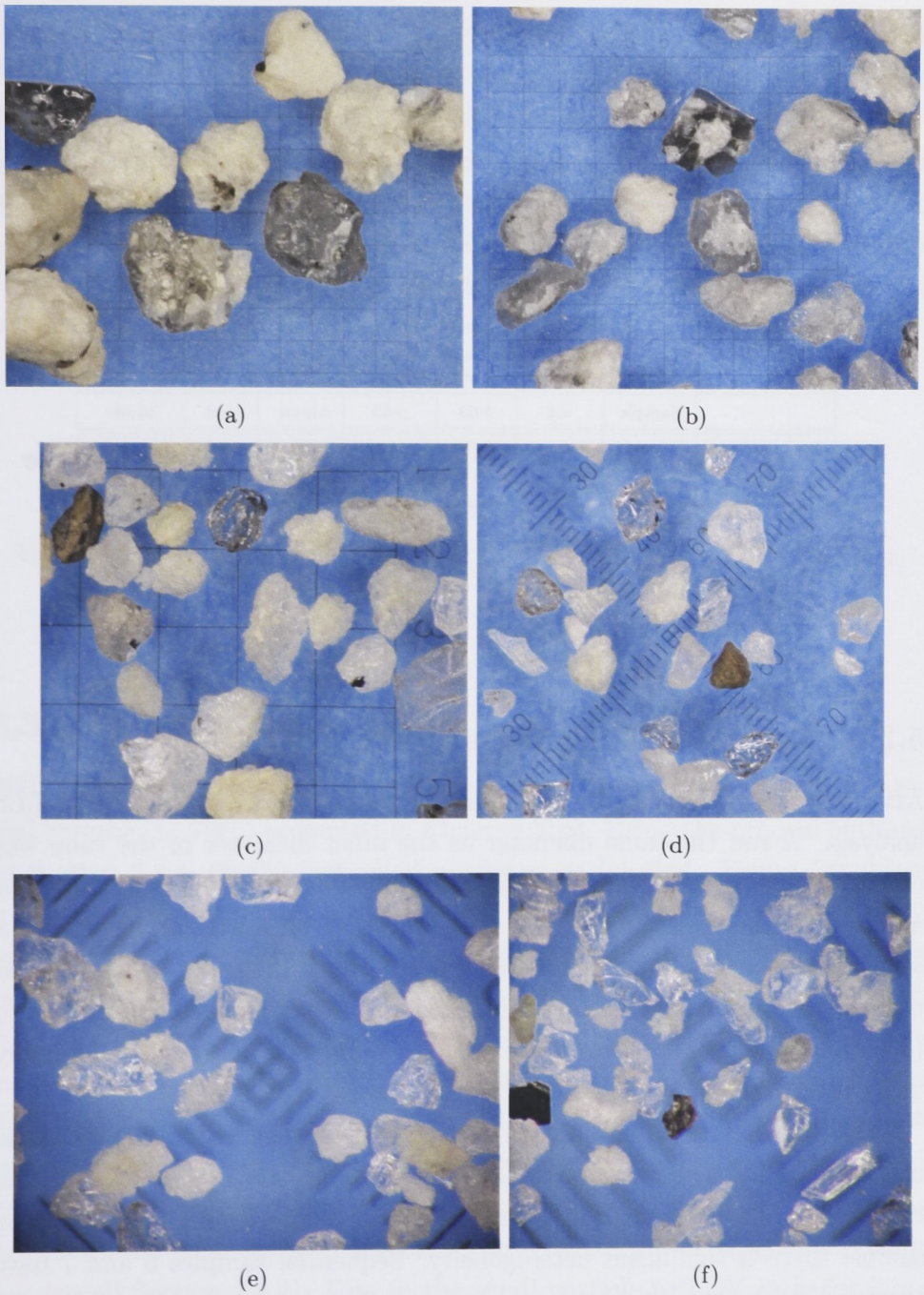

Figure 5.7: Grain morphology and size from micrscope. (a) $>2mm$ grain fraction. (b) 1-2mm grain fraction. (c) 0.5-1mm grain fraction. (d) 0.250-0.5mm grain fraction. (e) 0.125-0.25mm grain fraction. (f) 0.125-0.063mm grain fraction. Where squares are present (a,b & c) they are $1mm^2$. The scale in d, e & f have $100\mu m$ divisions.

The average volume weighted particle size is $542\mu m$. The median is $649\mu m$ and the mode fell in the 500-$1000\mu m$ range.

A separate sample from 50-$80cm$ further down the depth interval at $7.3m$ was also analysed (Figure 5.8(a) - black trace). This sample exhibited a very different distribution with a mean and median particle diameter of almost $800\mu m$ (see Table 5.2.) and more than 20% of the sample retained on the $2mm$ sieve compared to 5% for the original sample.

	cm^3	% clay	% silt	% sand	Volume weighted μm		
	Sample	<4	4-63	>63	Mean	Med.	Mode
Sieve 6.4-5m	≈250	1	4	95	542	649	500-1000
Sieve 7.3m	≈250	0	5	95	798	788	500-1000

Table 5.2: Particle size distribution from 3 different analytical techniques.

5.3.2 Laser Light Scattering (LLS)

After imaging of the sample the material was removed from the tube for LLS analysis. A rod the same diameter as the inner diameter of the tube was carefully pushed into one end a distance of $5mm$. The $5mm$ of displaced material at the other end of the tube was then sliced off and put into a separate sample container. This was repeated until the tube was empty and there were 10 individual samples (labelled 1-10) each representing one tenth ($3.3cc$) of the original $33cc$. These samples were then analysed individually using the Saturn Digisizer 5200.

The 10 subsamples exhibit a range of PSD as delineated by light blue in Figure 5.8(b) The mean particle diameters from the 10 subsets span the range $401\mu m$ to $983\mu m$ (Table 5.3) indicating that within the $50mm$ long sample there is significant heterogeneity. Sequential samples 6 and 7 have the smallest means, possibly representing a finer layer towards the lower / middle of the core (see Figure 5.6 indicated by red arrows).

These 10 datasets were combined to give an overall PSD with a mean of $633.3\mu m$ (see Figure 5.8(b), in blue. To facilitate a more realistic comparison

with the imaged portion of the sample (recall Figure 2.4(d)) the data for the first 2 and the last 2 subsections representing $10mm$ of material from either end was removed from the analysis and the remaining central 6 datasets ($19.8cc$ of material) were combined. This data is in red in Figure 5.8(b) and is used for all subsequent comparisons. The mean for this portion of the sample was $577.6\mu m$ with 2% clay, 7% silt and 91% sand, and is therefore classified as a sand. Particles in the range 5470-6330μm were identified and almost 10% of the material by volume is silt; $<63\mu m$. A summary of the distribution is given in Table 5.4.

1	2	3	4	5	6	7	8	9	10	Total	Mid 6
642	612	639	612	674	401	519	621	629	983	633	578

Table 5.3: LLS mean particle diameter (μm) for the 10 analysed subsections.

5.3.3 3D Image Analysis

PSD from the 3D image was based on the phase separated image of the fiducial volume (11.70cc) presented in Figure 5.5(d). Using the process outlined in Section 2.3.4, 66,870 individual particles are labelled. Figure 5.9 shows a 2D cross section through the fiducial volume before and after labelling of the individually identified particles. As the 3D dataset has a voxel size of $16.35\mu m$, only particles on the order $\geq 40\mu m$ are likely to be resolved. The smallest particles identified were $70\mu m$ in equivalent diameter. The largest particles identified using this technique (8 in number) were between 1512-1857μm in diameter. Inspection of the 2D slice presented in Figure 5.6 however, clearly shows at least 1 particle with a diameter $>5mm$ (in the red circle). This particle, due to it's proximity to the edge of the field of view has been removed from the distribution because it intersects the fiducial boundary (recall Section 2.3.4). Due to the small particle to FOV ratio for large particles they are more likely to intersect a fiducial boundary than smaller particles and may skew the distribution away from larger particles. Moreover the particle partitioning algorithm, which works on the basis of seeds at

maximal distances to pore edges can partition one large mico-porous particle with internal porosity into several smaller particles. The arrows in the 2 images in Figure 5.9 indicate an example of this.

The results of the particle size analysis are presented in Figure 5.8(c). The volume weighted mean was $513\mu m$, and a median and mode of $443\mu m$ and 398-$446\mu m$ respectively.

5.3.4 Comparison

Figures 5.10 (a) and (b) compare the PSD obtained from sieve, LLS, and 3D image analysis. One immediately notices the individual datasets from LLS cover a very broad range indicating a high level of sample heterogeneity. The sieve data falls well within the range established by LLS and both identify material in the sub $63\mu m$, silt range, and in the greater than $2000\mu m$ range (Figure 5.10 (b)). LLS analysis identified particles in the range 5470-$6330\mu m$ as did visual inspection with a microscope. In contrast the image analysis did not identify material in either of these ranges. Image resolution, limited FOV compared to particle size and the partitioning algorithm may all have contributed to the discrepancies. The lack of particles in the clay/silt size range is a result of the $16.35\mu m$ voxel size meaning only particles on the order $\geq 40\mu m$ are likely to be resolved as discrete entities.

Also, when comparing these datasets it should be noted that the sample size used for the sieve distribution was large ($\approx$40cc) compared to the 19.8cc for the LLS analysis, and the 11.70cc image volume. Additionally the sieve analysis was not undertaken on the same sample, but a sister sample as explained in Section 2.1.4. From this analysis we see that the PSD in heterogeneous material such as this sample is very sensitive to the size and spatial location of the subsample to be analysed, and the techniques utilised to measure it.

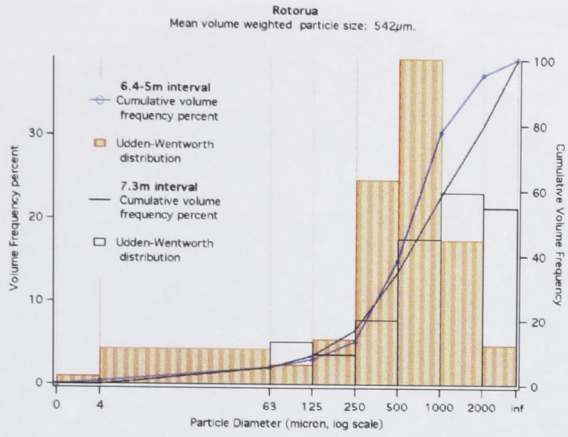

(a) PSD from sieve/hydrometer analysis.

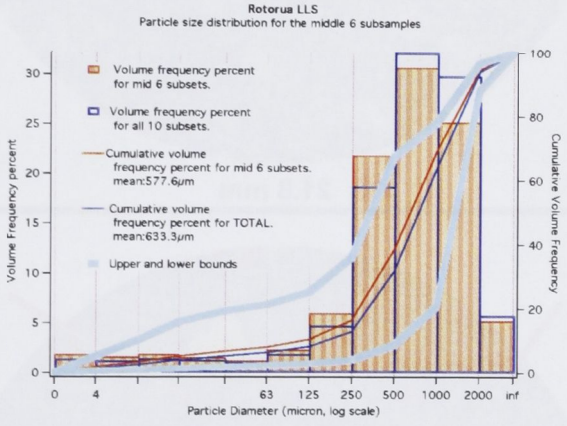

(b) PSD from LLS analysis.

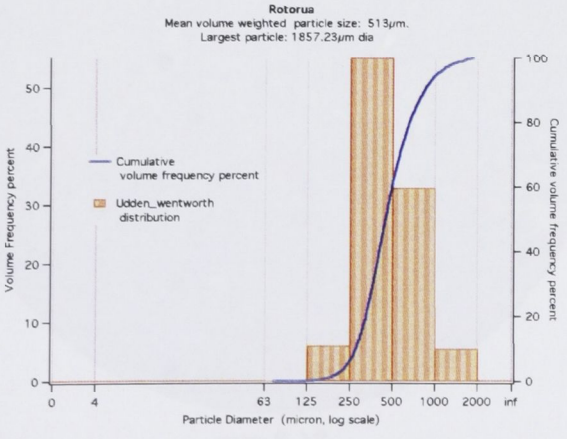

(c) PSD from analysis of the 3D image.

Figure 5.8: Distribution of particle size as measured by the sieve/hydrometer method, LLS and 3D image analysis.

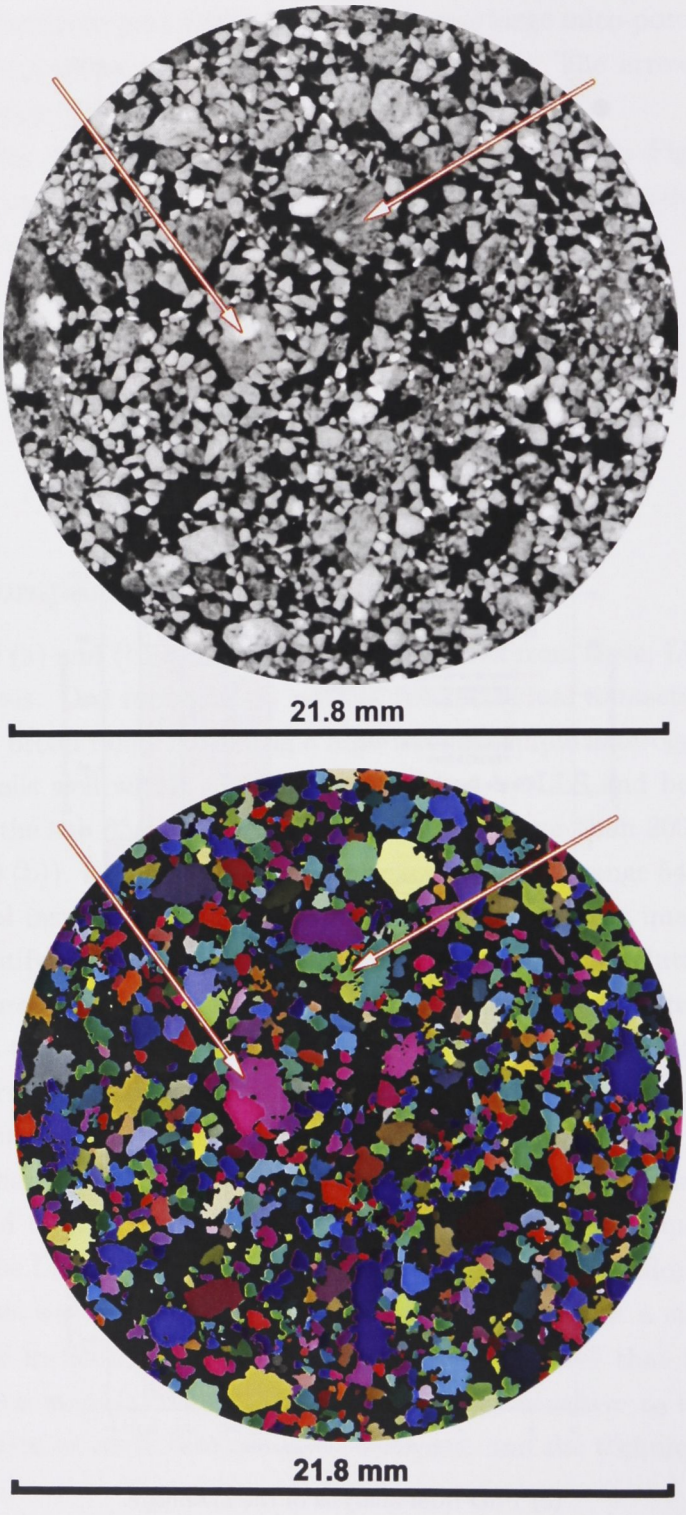

Figure 5.9: Grain partitioning of binarised 3D image into individual grains. All particles intersecting the image boundary are excluded from the data set. Arrows indicate large microporous particles partitioned into multiple smaller particles (see text on page 129)

Method	cm^3	% clay	% silt	% sand	Volume weighted μm		
	Sample	<4	4-63	>63	Mean	Med.	Mode
Sieve 6.4-5m	≈250	1	4	95	542	649	500-1000
Sieve 7.3m	≈250	0	5	95	798	788	500-1000
LLS (mid 6)	19.8	2	7	91	577.6	646	500-1000
LLS (total)	33.7	1	5	94	633.3	738	500-1000
X-ray CT*	11.70	0	0	100	513	443	398-446

Table 5.4: Particle size distribution from 3 different analytical techniques.
**no data on individual particles less than approximately 40μm in diameter.*

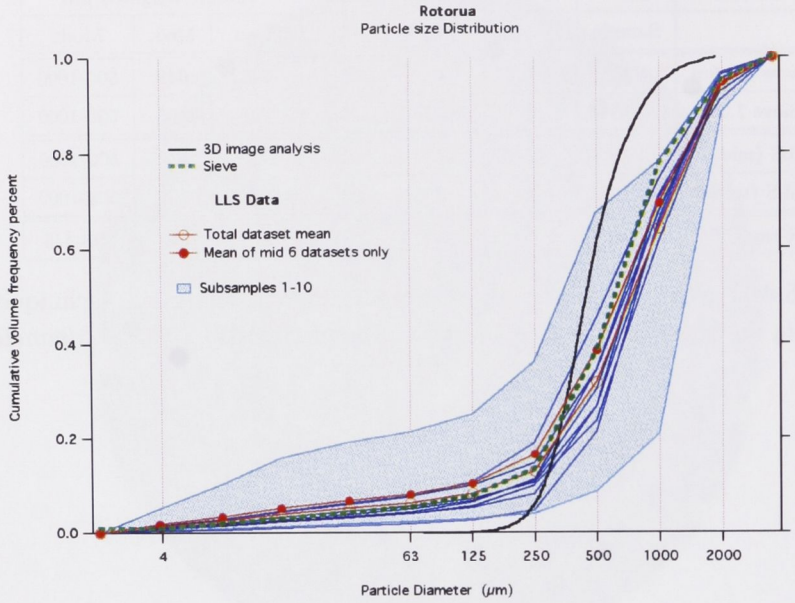

(a) PSD from 3D image, LLS and sieve analysis on x axis log scale. The blue shaded area delineates the 10 separate LLS datasets.

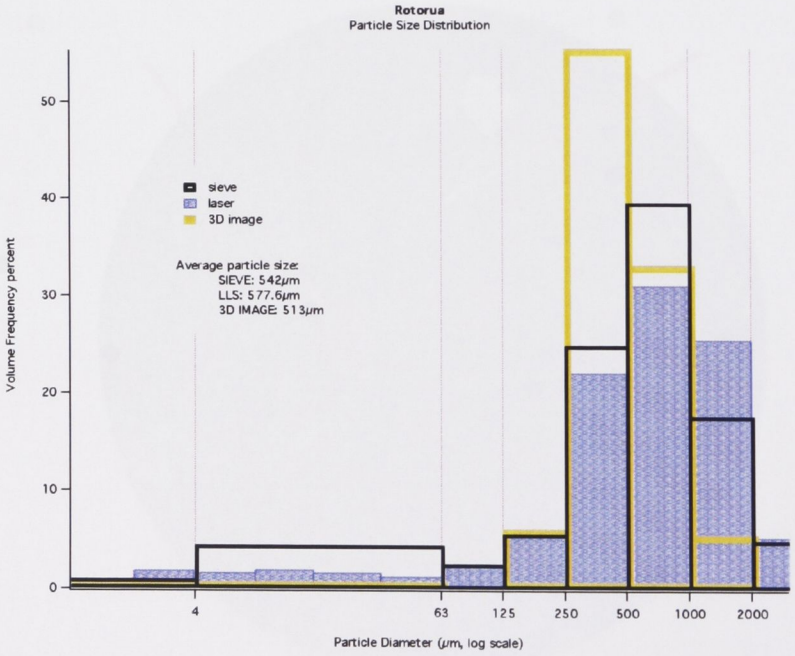

(b) Data binned to reflect the Udden-Wentworth scale.

Figure 5.10: Comparison of the 3 methods used to determine particle size distribution.

5.4 Textural Analysis / Shape Parameters

Due to the inability of the image analysis to resolve the extensive clay and silt portions of the sample and problems defining the larger particles, one would expect the textural analysis from image data to be error prone. However, for completeness and for comparison to the cleaner Ottawa sand samples we report the textural data in this section. More than 60,000 individual particles are identified from within the fiducial image volume.

5.4.1 Sphericity

Figure 5.11(a) and Table 5.5 presents data for volume weighted MPS (See Section (2.4.1)). The mean value was 0.77, little dependence upon particle size is noted. The value measures does indicate a sphericity slightly higher than the visual inspection of Figure 5.9 would suggest with most of the particles occurring in the 'Compact' range of Sneed and Folks sphericity-form diagram (see Figure 2.12(c)).

5.4.2 Zingg

The Zingg ratio is presented in Figure 5.11(b). Upon inspection of the plot it can be seen that the mean value for this measure lies between 0.76 and 0.8, an indication of a high level of sphericity with mostly equant shaped particles. One does notice some scatter into the prolate, oblate and bladed parts of the plot in the smaller particle size ranges. Again visual inspection of the particles presented in Figure 5.7 appears to indicate a larger non spherical fraction. Figure 5.7 also seems to show smaller S/I, I/L for smaller particles, but not seen in the data; sampling of a small number of particles and/or poor resolution of small particles are plausible explanations.

5.4.3 Co-ordination Number (Z)

Figure 5.11(c) and Table 5.5 give both the volume weighted and number weighted histograms for the Z value calculated for every individual particle. The average volume weighted Z value is 23. This contrasts markedly with

the number weighted value of 9.6 indicating Z significantly increases with particle volume. Again this is in contrast to the Ottawa sand sample which has volume weighted and number weighed means <10, and again reflects the much less heterogeneous nature of the PSD for Ottawa sand. Figure 5.12 is a small subsection of the particle contact network used to calculate Z. This Figure illustrates larger particles have more connections to neighbouring particles.

5.4.4 Sorting

Sorting is given in Table 5.5. For the imaged sample, the calculated sorting coefficient is $0.63\phi_u$ signifying that it is a moderately well sorted sample according to Folk and Ward (1957)(see Table 2.1). However, the 3D image statistics exhibit a much tighter PSD range than either the sieve or the LLS data; thus the result is underestimated. Visual inspection of Figures 5.2 and 5.9 would suggest a less well sorted sample.

The sorting coefficient calculated from the LLS and sieve data return a value of $1.78\phi_u$ and $1.37\phi_u$ respectively. These values indicate a poorly sorted sample.

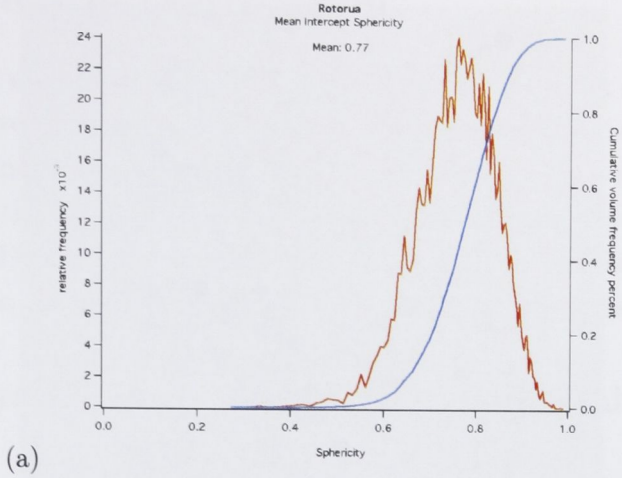

(a)

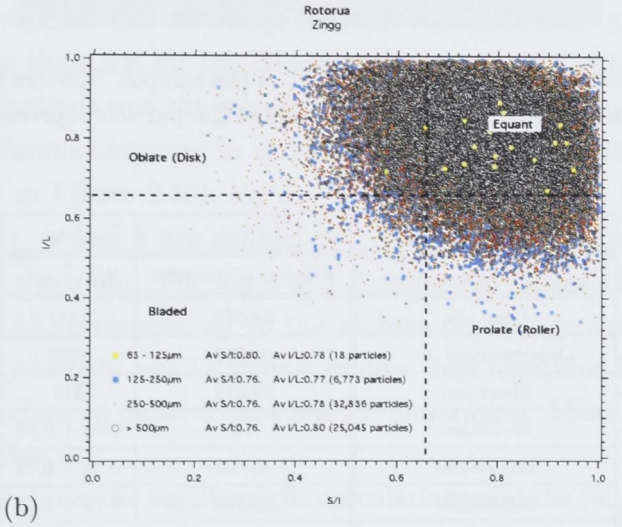

(b)

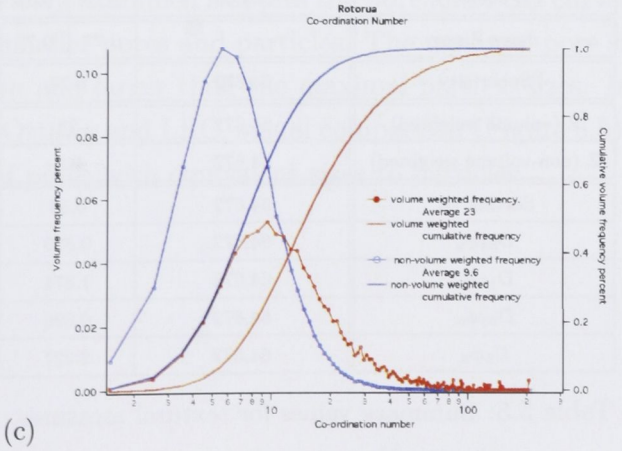

(c)

Figure 5.11: Shape parameters. (a) Mean intercept sphericity and (b) The Zingg ratio of long, intermediate and short axis of individual particles measured in the 3D tomogram. Colour is associated with particle size. (c) Number and volume weighted co-ordination number calculated on over 60,000 individual partices.

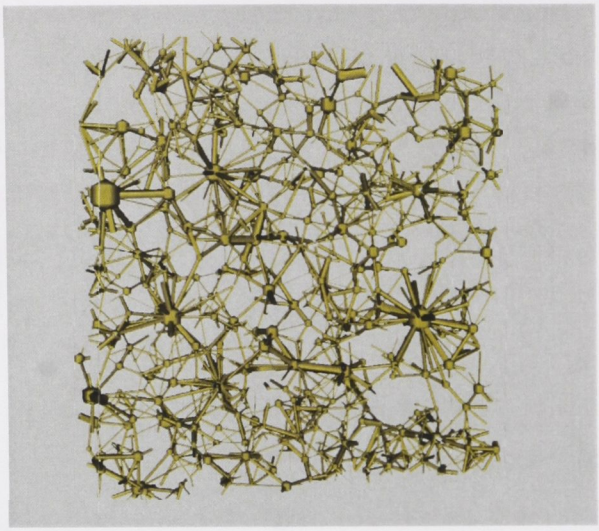

Figure 5.12: Network for the particle phase of the sample. Spheres are the particle centres. Size is a relative indication of the size of the particle represented. Contacts are represented by sticks.

		Mean	
Zingg	Number of particles	S/I	I/L
Long μm	64,672	1351	
Intermediate μm	64,672	1079	
Short μm	64,672	819	
63-125μm	18	0.80	0.78
125-250μm	6,773	0.76	0.77
250-500μm	32,836	0.76	0.78
>500μm	25,045	0.76	0.80
mean Zingg		0.77	0.78
Sphericity	64,672	0.77	
Z (volume weighted)	64,672	23	
Z (non-volume weighted)	64,672	9.6	
Sorting ϕ_u	64,672	0.63	
$D_{84}\phi_u$	64,672	0.630	
$D_{16}\phi_u$	64,672	1.874	
$D_{95}\phi_u$	64,672	0.096	
$D_5\phi_u$	64,672	2.227	

Table 5.5: Summary values for textural measures.

5.5 Pore Size Distribution

In this section we compare a number of pore size descriptors for these samples. PSD from sieve, LLS and image data is converted to pore size distribution via the A&P model (see Section 2.6). Pore-size distribution is also calculated directly from the 3D image using the covering sphere transform (CRT) (see Section 2.3.3.1), also via a simulated MICP experiment (see Section 2.6.2.1), and based on a calculation of pore network descriptions (see Section 2.6.2.2).

5.5.1 Arya and Paris Model (A&P) from Grains to Pores

PSD from sieve, LLS and 3D image analysis was converted to pore-size distribution using the A&P model. The porosity value used in the calculation of these distributions was the porosity value as calculated from the 3D image: 43.6%. Parameters used in the calculation were $a = 2.478$, $b = 1.490$ (from Table 2 in Figure 2.15), $\log c = 2.507$ and $x = 4.471$ (from Table 3 in Figure 2.15). a and b are defined according to the textural class of the sample, which was sand. The $\log c$ and x parameters chosen are the values from Figure 2.15 corresponding to the highest percentage sand and lowest percentage clay as only small amounts of clay were identified in the sample. The PTF is performed on all 3 data sets for illustration. Mean pore sizes are reported in Table 5.6.

Figure 5.13 shows the results of the calculations and the relevant PSD. As with the previously examined samples the pore and PSD curves are a similar shape for the smaller pores and particles. The maximal pore sizes are of the order of 2-3mm and larger than the maximal particle sizes. In this sample, in contrast to Ottawa and LRC, visual comparison (Figure 5.5) does indicate the presence of pores with equivalent sizes to particles.

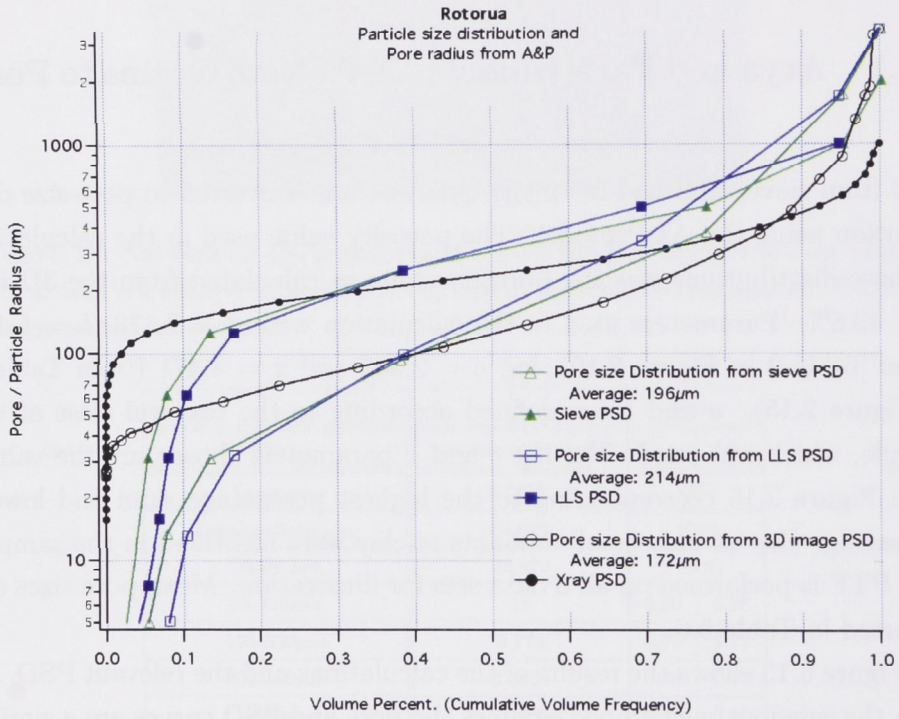

Figure 5.13: Pore size distribution converted from sieve /hydrometer, LLS and 3D image analysis PSD data using the A&P algorithm.

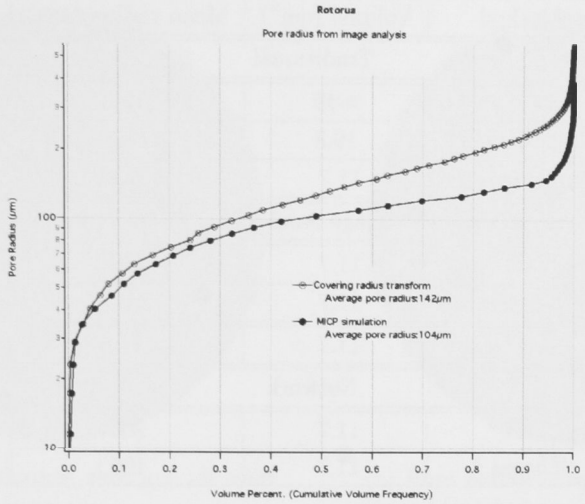

(a) Pore size distribution from CRT calculation.

Figure 5.14: Pore size distribution from analysis of the 3D image as a CRT and simulated capillary pressure curve from 3D image analysis.

5.5.2 Direct calculation from 3D Image Analysis.

Figure 5.14 reveals a pore size distribution calculated from CRT spanning the range $6\mu m$ to $572\mu m$, with an average of $142\mu m$. Table 5.6 contains a summary of these results. Figure 5.14 also shows the results of the simulated MICP experiment as a capillary pressure curve. Compared to the CRT data this distribution has smaller pores and a smaller range of pore sizes. Average pore radius is $104.41\mu m$. As discussed previously the distribution is flatter with less large pores due to pore shielding in the MICP process. l_c was calculated from the image and found to be $141.58\mu m$.

5.5.2.1 Network pore-size distribution

A 2D slice through the partitioned volume is presented in Figure 5.15(a) and (b). From these Figures we do observe some correlation in the pore sizes; the pore partitioning illustrates many large pores adjacent to other large pores. Pore to throat aspect ratio are of the order of 2:1. Figures 5.15(c)

Method	Volume (cm^3)	Mean radius (μm)
Traditional		
A&P Sieve	≈40	196
A&P Laser	19.8	214.54
A&P image	11.7	172.92
Image Analysis		
CRT*	11.7	142
Cap pressure*	11.7	104
l_c*	11.7	141.6
Network		
Pore*	11.7	206
Throat *	11.7	106

Table 5.6:
Pore size distribution from all the different analytical techniques used to estimate/measure pore size used in this study.
** no data available for pore radius less than approximately 20μm radius due to image resolution.*

and (d) show these distributions; the average pore radius was 206.22μm and the average throat radius was 106.24μm.

While the 2D slice in Figure 5.15(a) appears to show pore to pore correlations with large pores connected across the sample, there does not appear to be any spatial correlation between large particles and large pores. From Figure 5.15(e) we also see in 3D some clustering of large and small pores with a backbone of connected large pores.

5.5.3 Comparison of the Techniques used to obtain pore-size distribution

In Figure 5.16 the different pore size distributions are compared; those derived from the image are very flat in contrast to the A&P model. The

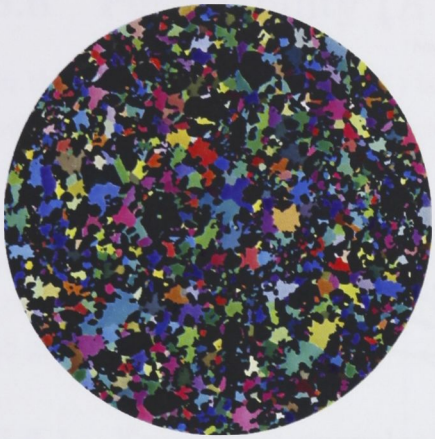

(a) Pore partitioning showing all void space classified pore.

(b) Pore partitioning showing only void space identified as throat.

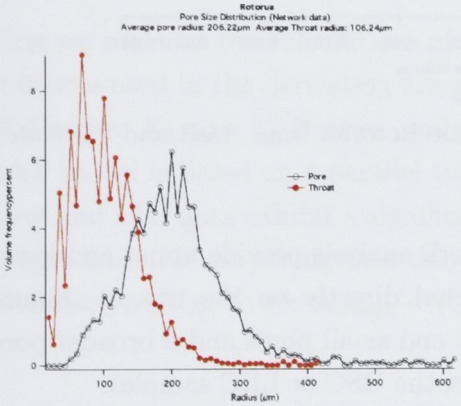

(c) Frequency percent of pore and throat radii volume weighted

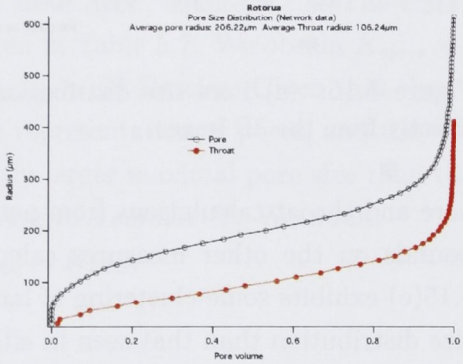

(d) Cumulative frequency percent of pore and throat radii volume weighted

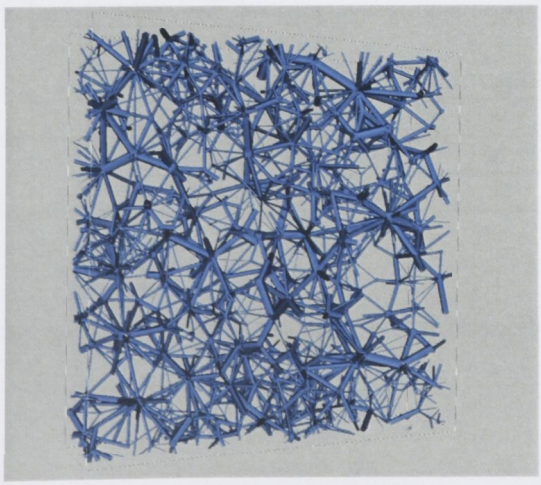

(e) Pore throat network. Throat size is indicated by the relative size of the sticks joining pore bodies (balls). NB. The backbone of larger pores.

Figure 5.15: Network analysis.

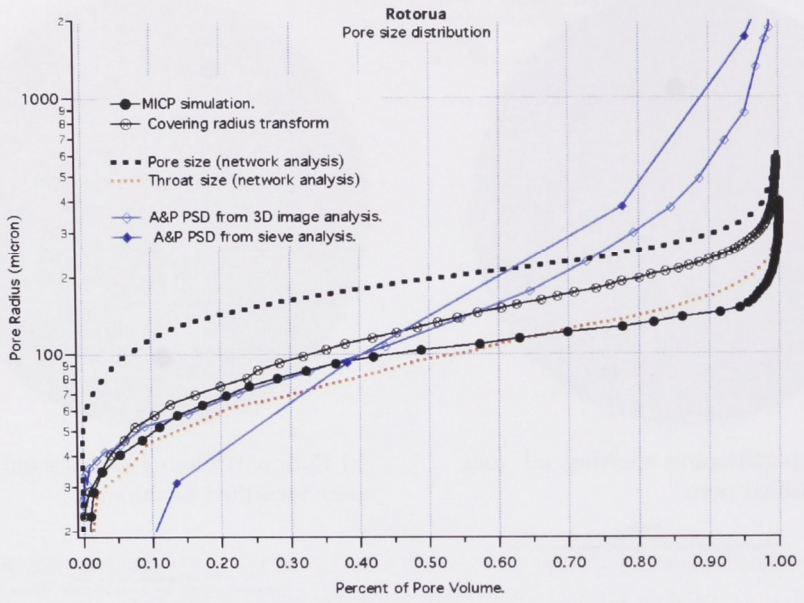

Figure 5.16: (a) Pore size distribution for Rotorua from A&P and calculated directly from the 3D image.

pore and throat calculations from network analysis provide upper and lower bounds on the other measures calculated directly on the image. Figure 5.15(e) exhibits some clustering of large and small pores and a broader pore size distribution than that seen in either the OSC or LRC samples.

5.6 Permeability (K)

In this section permeability (K) is calculated indirectly from the PSD using pedo-transfer functions which convert PSD to K. Previously this has been performed on the PSD from the 3D image only. For this sample, given the poor PSD estimate obtained from the image data, we also report for comparison K calculated from the PSD obtained by sieve. As the larger connected pores are well identified direct simulation of K from LB is expected to give good estimates.

5.6.1 Empirical correlations

5.6.1.1 Arya and Paris

First we consider the calculations of K from A&P, equation 2.8. The PSD statistics used in the derivation are given in Table 5.7. We obtain $K_{sieve} =$ 36 Darcies, $K_{LLS} = 37$ Darcies, and $K_{image} = 24$ Darcies. Given that the A&P model is based on a parallel tube representation of pores, and the sieve and LLS data exhibit a significantly larger maximal pore size than the image data, it is surprising that they all give a similar K. We would reasonably expect to see $K_{image} < K_{sieve} \approx K_{LLS}$.

(a)

ρB	$1.198 g/cm^2$
ρP	$2.381 g/cm/^2$
ϕ	0.436
a	-2.478
b	1.49
b	321.37
x	4.471
e	0.98748

(b)

Input PSD	K Darcies
Sieve	36
LLS	37
3D image	24

Table 5.7: (a) Parameters for the A&P calculation of permeability. (b) Calculated K.

5.6.1.2 Berg (1970)

Permeability was also calculated from the PSD statistics obtained from the 3D image analysis (see Table 5.8(a)) using equation 2.10 (Berg, 1970)(see Section 2.7.1.2). K was found to be 74 Darcies. As the PSD data is less accurate K has also been calculated using the PSD from sieve. This calculation gave 49 Darcies (Table 5.8(b)). The results are similar; the PSD from sieve data is more poorly sorted (larger p) but also exhibits a larger mean particle size; these 2 differences offset.

(a)

PSD from 3D image	
D	$0.444mm$
ϕ	43.6%
d_{10}	2.035
d_{90}	0.3955
p	0.8196
$K(D)$	74

(b)

PSD from sieve	
D	$0.649mm$
ϕ	43.6%
d_{10}	2.625
d_{90}	-0.699
p	1.663
$K(D)$	49

Table 5.8: Parameters for the Berg (1970) calculation of permeability. (a) PSD statistics from the 3D image analysis, and (b), from sieve.

5.6.1.3 Panda and Lake (1994)

From equation 2.15 permeability was calculated to be 214 Darcies when τ was equal to 3. τ was also calculated directly from the 3D image and found to be 2.00 (see Figure 5.17). When this value was used K was found to be 321 Darcies. The PSD statistics and bulk property input parameters are given in Table 5.9.

	3D image analysis	
$\overline{Dp}$	$303.51\mu m$	
ϕ	0.436%	
γ	1.58	
C_{Dp}	0.414	
σ	125.78	
τ	$\tau = 3$	$\tau = 2$
K in Darcies	214	321

Table 5.9: Parameters for the Panda and Lake (1994) calculation of permeability.

5.6.1.4 MICP Simulation (Capillary Pressure)

Permeability, calculated as a product of equation 2.16, was 698 Darcies (Table 5.11). Input parameters to the equation are given in Table 5.10. $\tau = 2$ where $F = \frac{1}{\sigma/\sigma_0} = \tau/\phi$ from Figure 5.17)(recall Section 2.7.2).w

	3D image analysis
l_c	$141.58\mu m$
C	0.16
τ	$\tau = 2$

Table 5.10: Parameters for the calculation of permeability by Katz and Thompson (1986).

5.6.2 3D Image Analysis

Permeability is calculated independently on 225 x 216^3 subset blocks from within the fiducial volume, each subset is 1080x1080x1944 voxels with a volume of $9.9cm^3$ (Figure 5.18). The K and ϕ for each block is plotted in Figure 5.18. Porosity averaged over all the blocks was 46.5% and the average permeability value was 490.68 Darcies. This value does not account for the

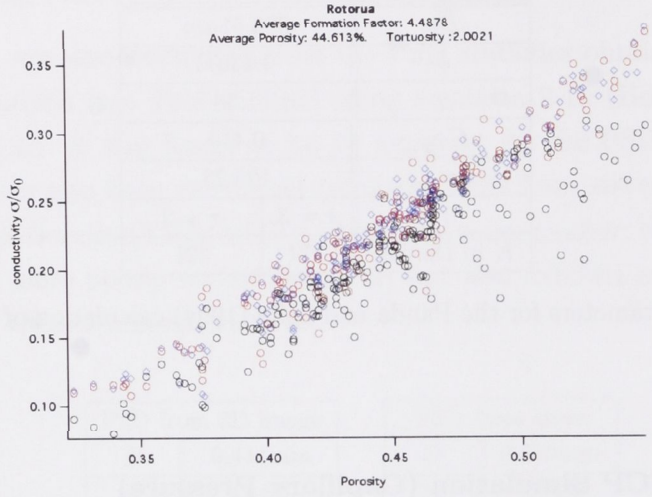

Figure 5.17: F calculated on 225 discrete 216^3 blocks.

fact that each individual block may or may not be well enough connected for the average figure to be an accurate representation of the sample at larger length scales, it does however set an upper bound on the permeability of this sample.

5.6.3 Comparison of permeability

A comparison of the results calculated from the different methods are presented in Table 5.11. From these results we see that as with the previously examined samples, $K_{A\&P}$ and K_{Berg} is much lower than the other values. K from $K_{A\&P} < K_{Berg} < K_{P\&L} < K_{LB} < K_{lc}$. Very large K from the image based calculations is due to the large connected porosity which is evident in Figure 5.15(e).

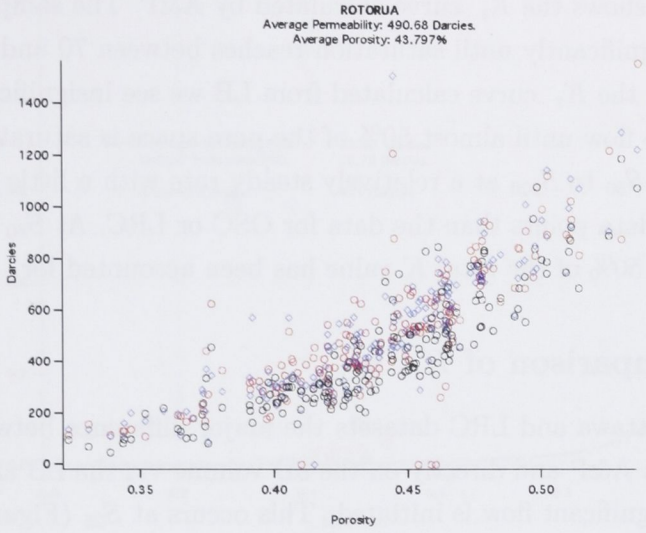

Figure 5.18: Permeability in Darcies calculated and averaged over 225 discrete 216^3 blocks using a lattice Boltzman algorithm.

Rotorua		
	PSD from image	PSD from sieve
Method	Darcies	
Arya and Paris	23.52	35.71
Berg	74.24	49.29
Panda and Lake	214.4 ($\tau = 3$)	321.3 ($\tau = 2$)
	3D image analysis	
LB*	491	
l_c : 141.58μm	698	

Table 5.11: Permeability comparisons. Values are calculated using A&P, P&L, Berg, the lattice Boltzman equation and l_c .

** denotes an average over 225 x 216^3 blocks.*

5.7 Relative Permeability (K_r)

Figure 5.19(a) shows the K_r curve calculated by A&P. The sample does not conduct significantly until saturation reaches between 70 and 90% (S_{70-90}). From the K_r curve calculated from LB we see insignificant contribution to flow until almost 50% of the pore space is saturated. K increases from S_{50} to S_{100} at a relatively steady rate with a little more scatter in the data points than the data for OSC or LRC. At S_{80} approximately 50% of the total K value has been accounted for.

5.7.1 Comparison of K_r

As with the Ottawa and LRC datasets the major difference between calculating K_r from A&P and directly on the 3D volume via the LB algorithm is S_w at which significant flow is initiated. This occurs at S_{25} (Figure 5.19(b)) when calculated from the image. In contrast A&P assume that only the largest 30% of the voids are associated with flow (Figure 5.19(a)). This is consistent with the A&P model assumption that pore radii is directly proportional to an associated particle radii and pores are present as equivalent capillary parallel tubes. Again, as with the previous analysis, the absolute K from A&P is much lower than that calculated from the image (Figure 5.19(b)).

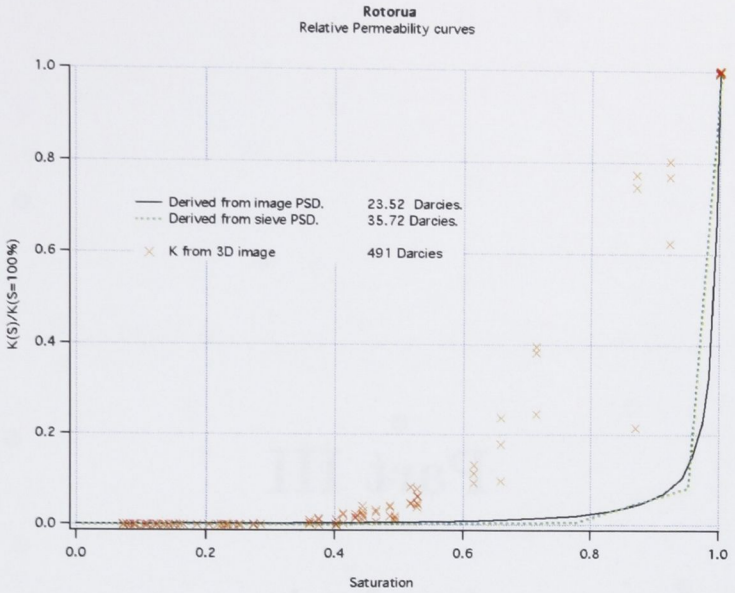

(a)

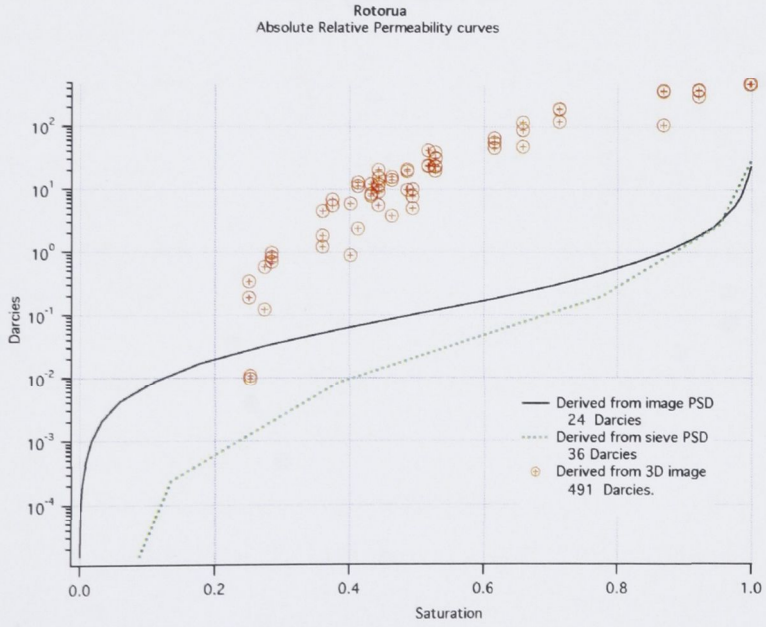

(b)

Figure 5.19: Relative permeability from LB and A&P using the PSD from image and sieve. (a) Relative Permeability comparison. (b) Absolute permeability comparison.

Part III

Analysis

Chapter 6

Discussion and Conclusions

Accurately characterizing hydraulic properties in real porous materials is crucial to a range of applications in the soil sciences; in Australia alone, understanding salt and contaminant migration in soils is crucial to the implementation of groundwater remediation strategies and addressing the problem of dryland salinity and deteriorating water quality. The ability to understand the fluid flow properties will enhance our ability to predict the transport of salts and contaminants and hence our understanding of these problems. One of the main obstacles to real progress in predicting properties of unconsolidated porous materials for the soil sciences has been the need to accurately characterise pore and particle scale structure in 3D and thereby be able to predict properties of these complex materials. In this thesis I have illustrated an ability to study unconsolidated soil materials via micro-CT imaging. In particular, I have undertaken an imaging study of 4 unconsolidated soil samples ranging from model sands to complex regolith. I have used image reconstruction, phase identification, 3D visualization and pore and particle structural characterization methods to comprehensively describe the image data. Pore and particle characterizations have been generated in great detail and compared with conventional measurements with good agreement. Prediction of the hydraulic properties derived from image data have been directly compared to conventional methods for predicting hydraulic properties of soils. A number of conclusions can be made from this work and outlines for future research in this area can be given; these are outlined in the remaining

sections of this Chapter:

6.1 High Quality 3D Micro-X-ray CT Data of unconsolidated sediment samples.

A high-resolution and large-field X-ray micro-CT facility has been used to obtain the 3D structure of the four samples. Three of the four images, two Ottawa sand samples and the fluvial river system (LRC), can be considered of high image quality. In these three samples the x-ray attenuation data allowed unambiguous phase separation of the pore and mineral phase peaks (eg. Figure 6.1(a)). This enabled one to analyse the structure of the pores and particles in detail. The fourth sample, Rotorua, was more difficult to analyze quantitatively. The sample exhibited the presence of varying mineralogy and particularly the presence of low density porous inclusions (e.g., microporosity in porous pumice particles). This leads to a spread in the low density signal making it difficult to unambiguously differentiate the pore from the microporous and solid mineral phases (Figure 6.1(b)). In addition to the complex mineralogy in the Rotorua sample, it also exhibits particles ranging in size over three orders of magnitude in length scale (see Figure 5.10(a)). The sample also exhibited extreme heterogeneity. The particle size distribution for 10 sister samples, each of $3.3cc$ in volume, exhibited more than 100% variation in mean particle diameter (recall Figure 5.10(a)). Figure 6.1(b-f) shows the difference between the easily resolvable data returned for LRC compared to the more problematic Rotorua sample. While the analysis of the mineral phase and particle sizes is difficult for the Rotorua sample, the most dominant part of the connected pore phase is easily identified and it is believed that the hydraulic properties derived on the image data from tomography are realistic.

The difficulties noted in the examination of the Rotorua sample do highlight current limitations on the quantitative analysis of the 3D structure of granular materials with micro-CT and leads to proposed future directions for improved imaging methods of these more complex samples. The Rotorua sample highlights a limitation associated with the need for balance between

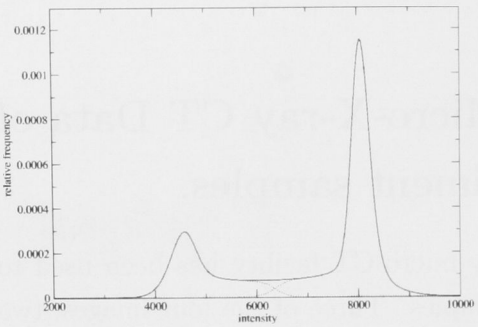

(a) LRC X-ray attenuation histogram.

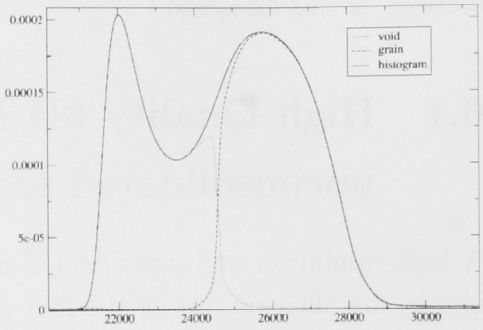

(b) Rotorua X-ray attenuation histogram.

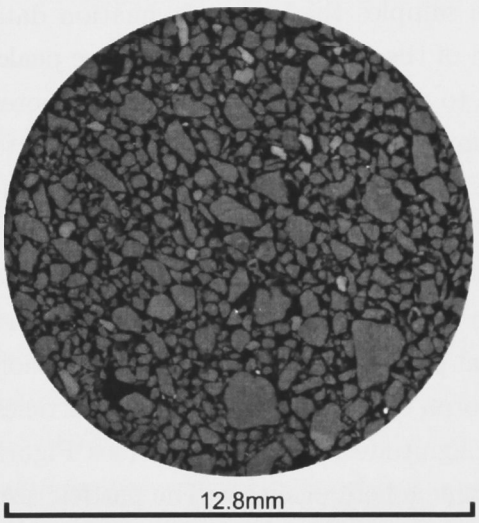

(c) LRC 2D greyscale slice.

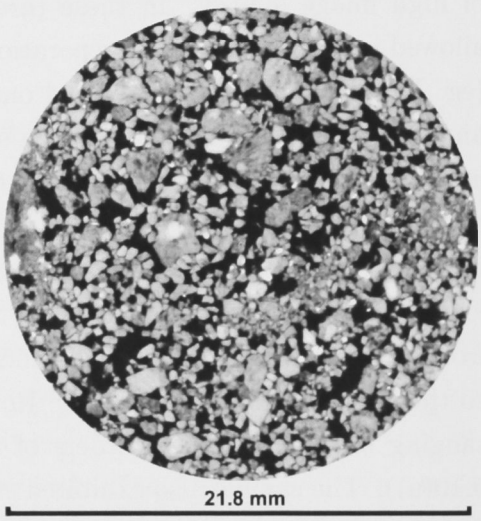

(d) Rotorua 2D greyscale slice.

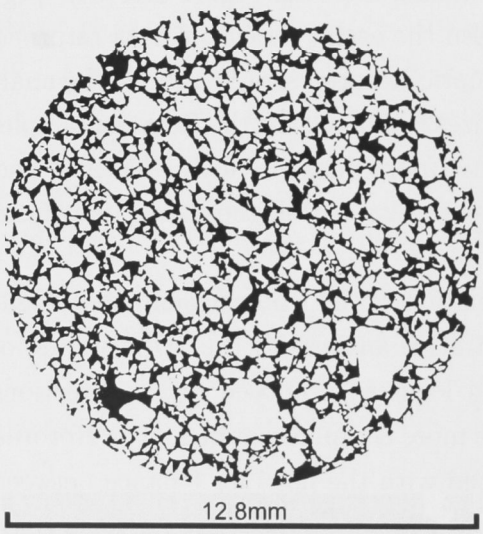

(e) LRC segmentation into void and granular phases.

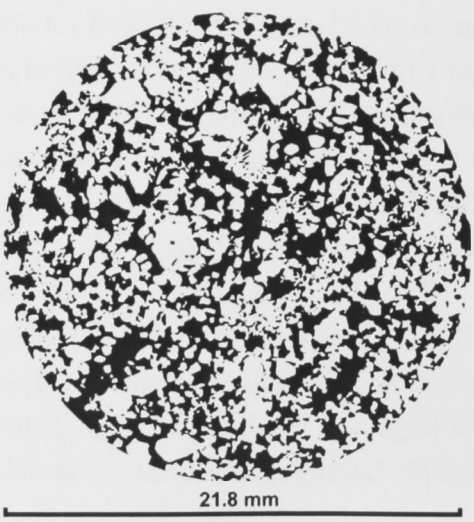

(f) Rotorua segmentation into void and granular phases.

Figure 6.1: Attenuation histograms, greyscale slice and resultant segmented datasets for LRC and Rotorua.

sample size and sample resolution. With the current micro-CT setup there is a natural limitation that the voxel resolution of the sample is 1/2000 of the sample size; the sample always sits within the camera field of view. The heterogeneous nature of the Rotorua sample implies one should maximize the sample size to obtain representative data; the current sample size ($30cc$) may be optimal. Smaller volumes would be difficult to consider due to the friable nature of the samples; subsampling would be problematic as one must consider an undisturbed subvolume of the image. Recall that the image volume for consideration lies about 2-3 particles inside the tube volume (recall Figure 5.3(b)). This limits the voxel size to $16\mu m$; from the particle analysis data (Figure 5.8) we observe a significant presence ($\approx$10%) of particles at and below this scale. It would therefore be difficult to characterize these particle and pore characteristics at a smaller length scale. An exciting future direction for imaging of unconsolidated samples would involve Region-of-Interest (ROI) scanning; in this method one overcomes the trade-off between object size and spatial resolution by imaging a subset of the full image volume. Here one can focus on a subset of a larger sample and analyse the structure in 3D at higher resolution. This does not require recutting of the sample to a smaller physical size; one focuses in on a region of a sample smaller than the full sample size. In Figure 6.2 we show an example of this ROI analysis on an unconsolidated sand; the quality of the image reconstruction should allow for accurate segmentation. This work currently being undertaken by the Applied Maths group, will assist in the analysis of more complex sands.

A second area that would greatly improve the predictive ability of the imaging method is to integrate micro-CT with other microscopy techniques. This in particular will allow one to analyse the mineralogy of the sample and to potentially undertake more accurate phase separation of the sample volume. This requires undertaking thin section acquisition of samples from within the tomogram field of view and undertaking backscatter scanning electron microscopy (BSEM) and optical microscopy studies of the resultant sample. This further requires sample registration of the two images. Registration is a process in which the two images are optimally superposed. The ANU group is implementing an optimization scheme to do rigid registration on different images of materials (Sheppard, in preparation). From

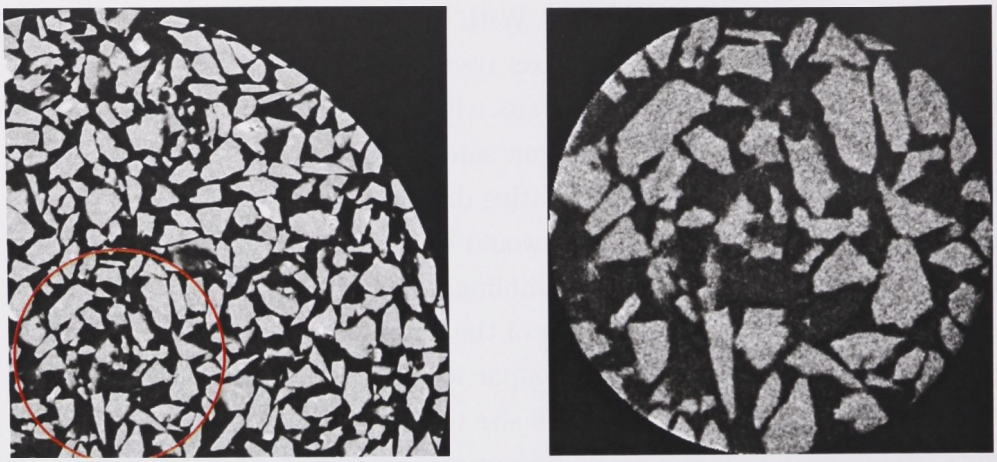

Figure 6.2: (a) An example of ROI scanning of an unconsolidated sandstone. The image on the left is the full volume of a 2048 cubed image. (b) the image on the right gives a 512 cubed image generated from the same projection data. While the image in (b) is grainier, one could perform phase separation on this. At higher resolutions the phase boundaries would be clearer. This is one possible method to probe finer length scales on the same image volume.

this superposed map of rock space, mineralogy and pore space more realistic descriptions of the sample volume can be obtained. An example of a co-registered BSEM and micro-CT image of a consolidated sample are shown in Figure 6.3.

6.2 Direct enumeration of the particle size statistics of the three samples in 3D.

6.2.1 Particle Size

In the thesis we have analysed the particle fabric and texture from 3D digital images of the four samples. Again, the analysis on the three more homogeneous samples (two Ottawa and LRC) are considered high quality data sets. As described above, the Rotorua sample exhibited too broad a distribution to allow quantitative comparison with experimental data. Digital analysis of the 50,000+ individually identified particles within each of the datasets

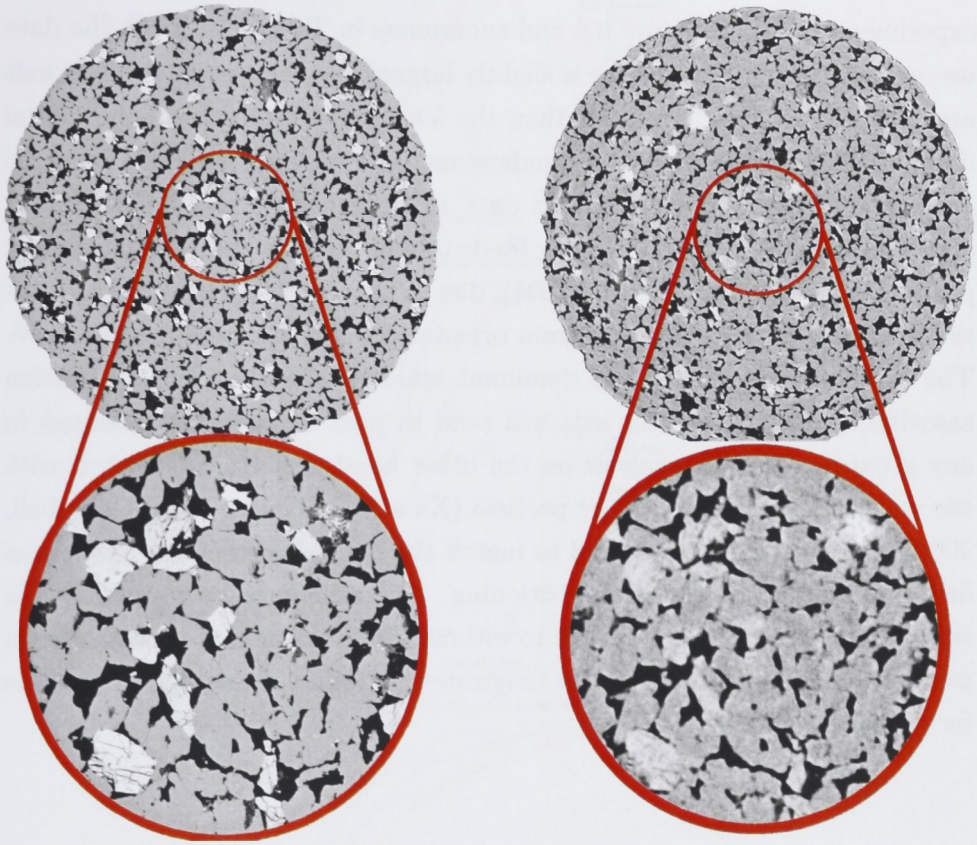

Figure 6.3: The left hand image is a BSEM image of a sandstone sample; the right hand image shows the same slice of the sample generated by tomography; the information obtained from BSEM (higher spatial resolution, mineralogy) allows more accurate characterisation of tomographic samples. This will allow one to better characterize the 3D information obtained from the micro-CT data.

allowed a direct comparison with the results obtained by sieving and LLS. It was found that the volume weighted $PSD_{sieve} < PSD_{image} < PSD_{LLS}$. Analysis of the digital data allowed not only the overall PSD measurement but also a measure of the long, intermediate and short axes of every individual particle. We compare the distributions of these different axes to the experimental data in Figure 6.4 and summarise in Table 6.1. From the data we see that the PSD from sieve is slightly larger than the measured short axis and the LLS is slightly smaller than the long axes derived from the digital data. This result allows one to understand and quantify the bias reported previously between sieve and LLS data in Buurman et al. (1997); Konert and Vandenberghe (1997). Sieving tends to measure the shortest axis of any particular particle (Eshel et al., 2004); due to the vigorous mixing of the particles on a sieve most possible grain orientations are 'sampled' on the sieve. The smallest axis will be the dominant scale measured as the orientation associated with the shorter axis will tend to pass through the openings in any given sieve. LLS analysis on the other hand is better correlated with the maximum projection of the particle (Xu and Di Guida, 2003; Campbell, 2003); this measure would tend to match the longest axis of the particle as derived from digital particle partitioning. The difference between LLS and sieve data could provide a means to estimate the variation of aspect ratio in particle sizes. This result further illustrates the value of this digital analysis for granular systems.

6.2.2 Textural and Shape characteristics

Unlike classical techniques such as LLS and sieve, the digital method allows one to more fully characterize the particle size, shape, and textural information of the granular materials. Textural characteristics are generally based on visual descriptions of representative particles and petrographic analysis of 2D thin sections. The classical methods have limitations in quantitatively describing the full 3D rock fabric; they are generally qualitative descriptions. The fabric and texture are readily quantifiable from the analysis of a 3D

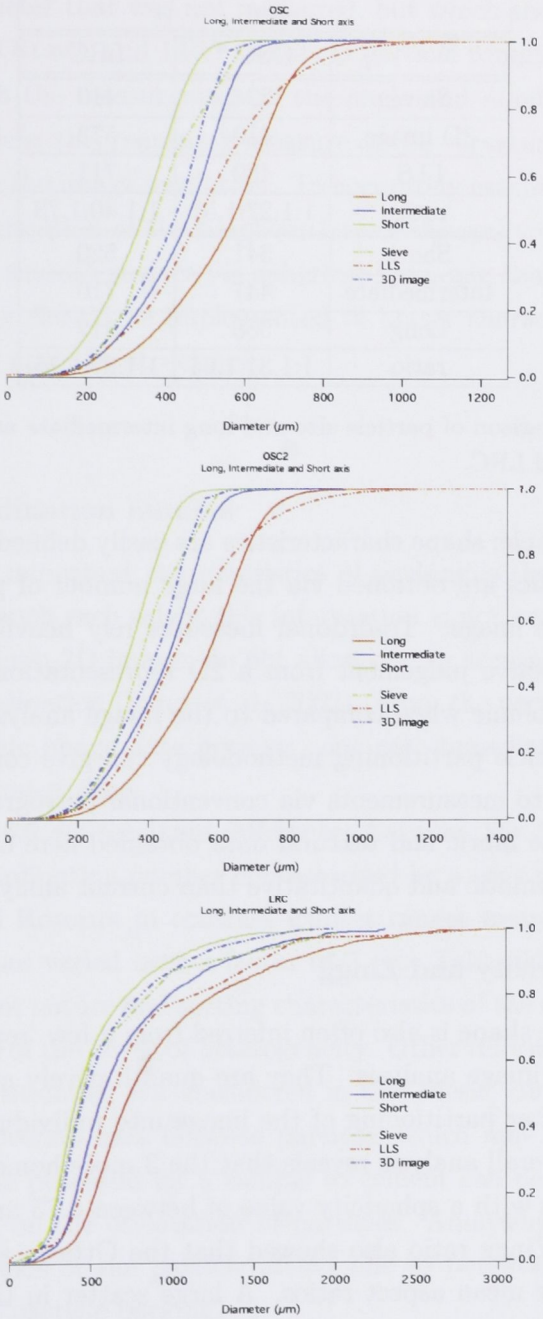

Figure 6.4: Long, intermediate and short axis measured on the particle partition data compared to PSD from sieve , LLS and image analysis for OSC, OSC2 and LRC.

μm		
	OSC *	LRC
Sieve	324	410
3D image	410	573
LLS	489	711
ratio	1:1.27:1.51	1:1.40:1.73
Short	341	520
Intermediate	447	710
Long	558	912
ratio	1:1.31:1.64	1:1.37:1.75

Table 6.1: Comparison of particle size and long intermediate and short axis measures for OSC and LRC.

image of the sample; shape characteristics are easily defined in 3 dimensions, and good statistics are obtained via the large number of particles that are processed in the image. Traditional measures rely heavily on the experimentalists subjective judgement from a 2D representation of a very small representative volume when compared to the image analysis. The development of the particle partitioning methodology can give complimentary and additional data to measurements via conventional petrographic techniques. In particular, the fabric and textural data obtained here can be more comprehensive, systematic and quantitative than current analysis techniques.

6.2.2.1 Sphericity and Zingg

Data for particle shape is also often inferred from a few 'representative' particles or via 2D image analysis. They are quantitatively available from the full 3D image after partitioning of the image into individual particles (Figure 6.5). The overall analysis reveals that the 3 more homogeneous samples contain particles with a sphericity value of between 0.75 and 0.77. The calculation of the Zingg ratio also showed that the Ottawa and LRC samples exhibited similar mean aspect ratios. A large scatter in the particle shape was apparent in the Zingg plots (recall Figures 3.10 and 4.8(b)) and a small change in shape with particle size was observed for all samples. These results are not apparent upon examination of the slice from the 3D images.

One shape parameter that was not measured, but which should allow one to differentiate the Ottawa and LRC sample is particle roundness. Roundness is associated with the measurement of the angle and number of sharp corners in each particle; this requires a measure of the curvature of the particle, which varies with the image resolution. To accurately estimate roundness requires the approximation of the rough surface of the real voxelated image to a continuous and smooth surface via spherical harmonic analysis (Garboczi). This methodology should be implemented to better characterise the shape differences in the granular structures.

6.2.2.2 Co-ordination number

One of the most important characteristics of packing is the frequency with which particles touch each other; this information is not available from conventional techniques; 2D images do not allow one to accurately characterize the particle co-ordination (Fauzi et al., 2002). From the particle partitioning of the tomographic image data however, one can immediately analyze this property on the image data.

From Figure 6.6 we see large differences between the 3 samples. OSC has very low co-ordination number characterised by a very tight distribution range. LRC and Rotorua in contrast exhibit ranges many times as large. The mean Z values varied over a factor of 3 (see Table 6.2). These values reflect the different nature and sorting characteristics of the samples and give a good indication of the levels of heterogeneity. Other information associated with particle partitioning, not considered in this thesis, can also be quantified. The total overlap area between particles which may be important in understanding the potential for a sample to cement can be measured along with information on the orientation of particles. Analysing the orientation of the principal axis of the particle allows one to potentially quantify the anisotropy in the particle packing.

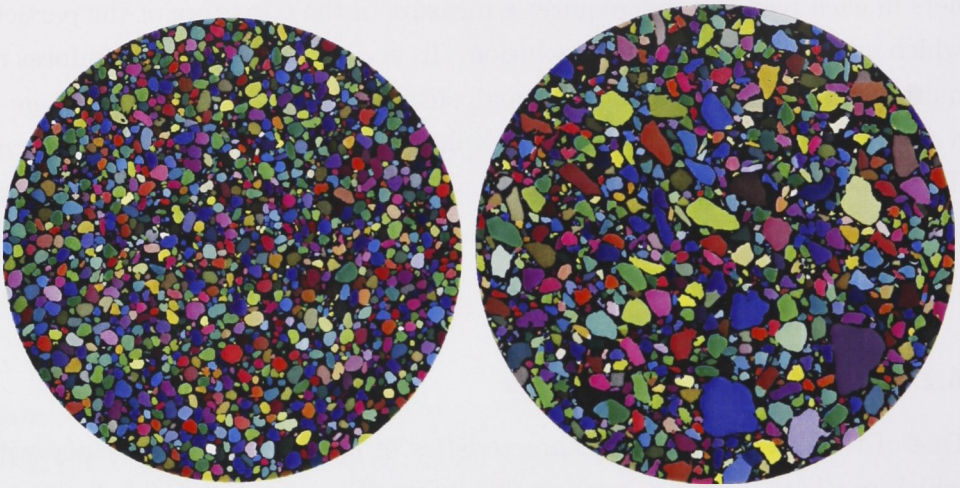

(a) Slice from a 3D particle partition of OSC.

(b) Slice from a 3D particle partition of LRC.

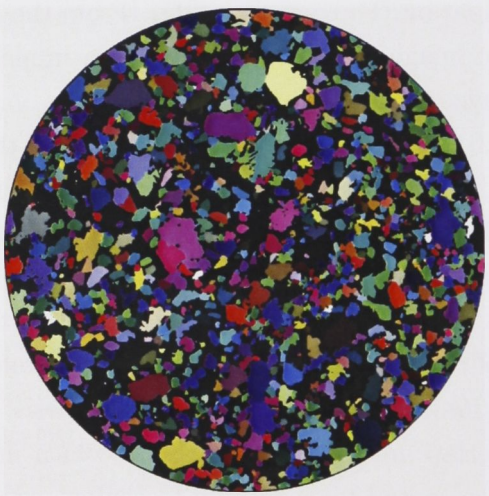

(c) Slice from a 3D particle partition of Rotorua.

Figure 6.5: 2D cross section slices showing the results of the particle partioning algortithm through samples OSC, LRC and Rotorua respectively.

	OSC	LRC	Rotorua
Z (VW mean)	9.5	35	23
Z (VW max)	42	277	206
Z (VW med.)	4.5	20	15

Table 6.2: Co-ordination number statistics for OSC, LRC and Rotorua.

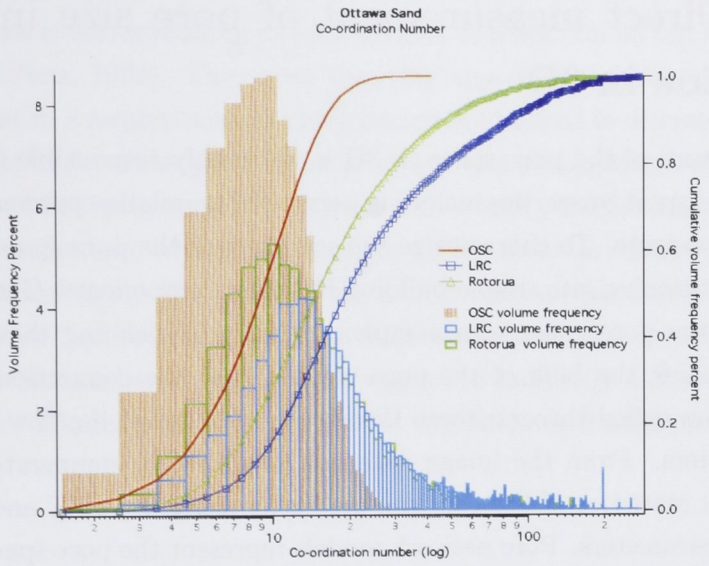

Figure 6.6: A comparison of the measured volume weighted co-ordination values for all 3 samples.

6.2.2.3 Sorting (SD)

SD is well defined from the image data for both OSC and LRC samples. Values of $0.45\phi_u$ (well sorted) and $0.78\phi_u$ (moderately sorted), were calculated from the particle partitioned data. These values are consistent with a visual inspection of 2D cross sections through the tomogram (recall Figures 6.5(a-b) respectively).

The PSD for the Rotorua sample is problematic; the small particles are not captured due to limited resolution (recall Section 6.1), and the large particles excluded due to sample size-FOV ratio. SD was calculated from both the image data and LLS data for comparison. From the image data SD was measured as $0.63\phi_u$ or moderately sorted; clearly this underestimates

the true breadth of the distribution. The distribution from LLS on the other hand returns an SD value of 1.78 ϕ_u; poorly sorted, more closely reflecting the nature of the sample determined from a visual examination (recall Figure 6.5(c)).

6.3 Direct measurement of pore size information in 3D

The structure of the pore space in 3D is ultimately responsible for the hydraulic transport properties including permeability, relative permeability and capillary pressure. To characterize the structure of the pore space in 3D requires partitioning into simple building blocks or components. Generally one describes the pore space of a complex medium by defining the pore bodies (containing the bulk of the pore volume) and the connections between these bodies called throats; these throats strongly effect the flow properties of the system. From the image data one can directly enumerate the pore and throat statistics of the complex media by using the CRT and capillary drainage parameters. Pore network models represent the pore space by a 3D network of interconnected pores and throats. From the pore network one can directly enumerate the pore size, shape and interconnectivity of the unconsolidated sediment samples. Results for the pore and throat sizes based on the image-based and network-based data is consistent.

For all samples we observe that pore and throat distributions place upper and lower bounds on the pore-size distribution generated by the CRT and MICP simulations and the pores are approximately 2-3 times as large as the throats (Figure 6.7). The capillary drainage parameter obtained from the MICP simulation is smaller than CRT because it measures throats whereas CRT places a radius on every pore element.

The image based derivation of pore size is directly compared to pore size from A&P. A&P estimated the distribution quite well for OSC (Figure 6.7(a)) but significantly overestimates pore sizes for LRC and Rotorua (Figure 6.7(b)(c)). The largest pore sizes given by the empirical model are over an order of magnitude larger than those found in the image (Figure 6.7).

This error is due to the assumption of a direct correlation between pore and particle size.The relatively good result for OSC reflects the lack of variability in the PSD. The overestimation for the other 2 samples reflects the PSD variability present in most natural systems.

Arya and Paris use the similarities between the WRC and the PSD curve to justify their derivation. The aim is to find a pore volume and representative pore radius corresponding to each particle size fraction on the PSD curve (Arya and Paris, 1981). They note that this approach requires us to ignore the fact that in a natural sample particles are not packed in discrete domains consisting of uniform size particles, but believe this assumption leads to good estimation of flow properties. It appears from results obtained here that estimating pore volume without accounting for the structure found in natural sample is insufficient. Berg (1970) notes that reduced pore size associated with particles that are not packed in discrete domains will impede flow regardless of the number of larger pores which are randomly distributed. The quantitative 3D analysis presented here is consistent with this prediction.

6.3.1 Direct testing of particle to pore-size correlations:

From the particle and pore partitioning of the image data one can quantifiably probe whether pore and particle sizes are correlated. Do pores of a particular size aggregate into families directly associated with a particular particle size as assumed by Arya and Paris (1981) or as noted by Berg (1970) do the large particles in granular materials have little correlation with the largest pores? The view of Berg (1970) is more consistent with the images of the samples shown in Figure 6.5 where we see a more or less random distribution of particles and pores of different size and shape. Berg also noted that a random distribution of small particles would lead to a reduced pore size which will impede flow regardless of the number of large particles/pores.

To directly test for a pore to particle size correlation we use the image data where all individual pores and particles within the FOV are identified. In particular for all particles all the directly neighbouring, or touching pores are identified. The pore size of these neighbouring pores are averaged to

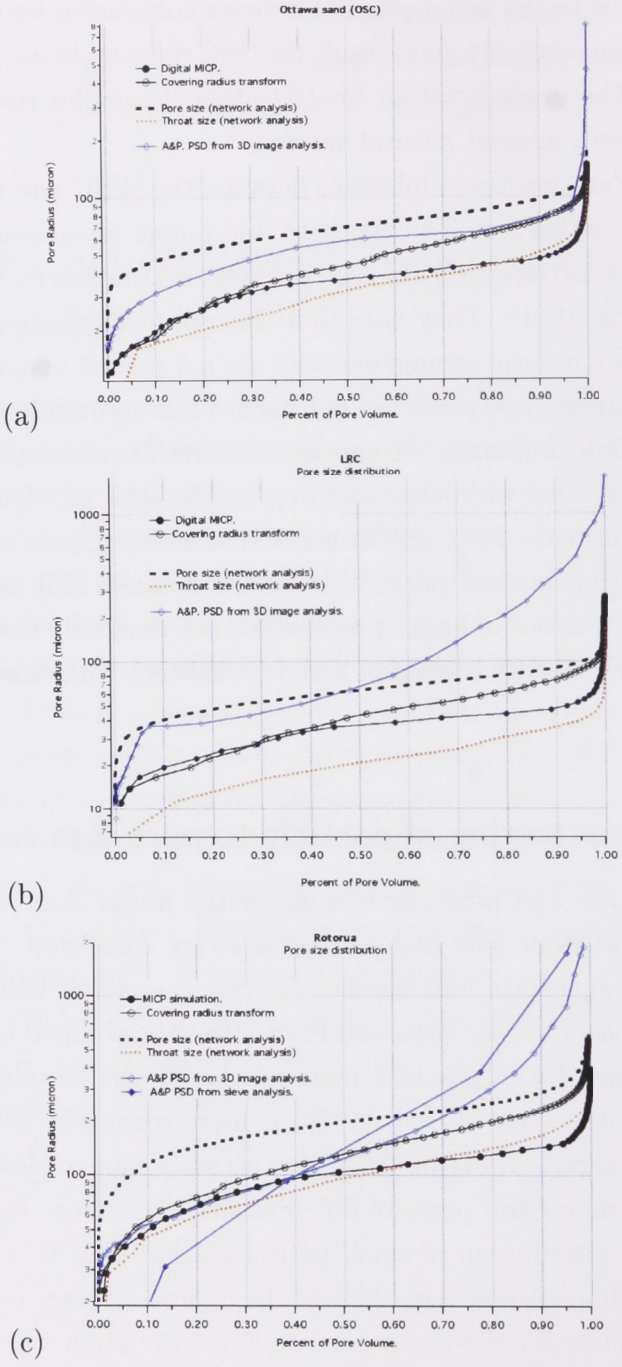

Figure 6.7: Pore-size distributions calculated using A&P (PSD from 3D image) and the 3D image as a MICP simulation, CRT and a network analysis of the pore and throat distributions for OSC, LRC and Rotorua respectively.

give a mean neighbouring pore size for all particle sizes. This information is plotted as the size of every particle against the mean size of all neighbouring pores. Figure 6.8 shows the resulting correlation plots for all 3 samples. From this analysis we see that particle and pore size are *not* spatially correlated and that the presence of a large particle does not necessitate the presence of large pores. The ratio of pore to particle size calculated from the numerical data shows that an increase in mean particle size is not necessarily followed by an increase in mean pore size (see Table 6.3). From a comparison of the OSC and LRC datasets we see, as stated by Berg, an increase in SD is followed by a decrease in pore to particle size ratio.

dia (μm)	OSC	OSC2	LRC
Throat	70	66	50
Pore	146	138	135
Particle	410	401	573
pore/particle	0.36	0.34	0.24
SD	$0.45\phi_u$	$0.46\phi_u$	$0.78\phi_u$

Table 6.3: Average pore to particle size.

Additionally, from a visual examination of the interconnected pore and particle networks presented in Figure 6.9 we see a distinct lack of pore:particle size correlations in these samples. From Figure 6.9(a) we see that as there is a small particle size range, the pore and particle distributions are very uniform. Figure 6.9(b) and (c) show a much less uniform structure but it is notable that the largest particles are surrounded by numbers of small pores and throats.

The dotted lines in Figure 6.8(a-c) show the particle to pore conversion used by A&P; the assumed correlation between particle and pore size is in contrast to the directly measured data. These results show that the assumption made that particle size determines pore size based on the shape similarities of the WRC and PSD is incorrect.

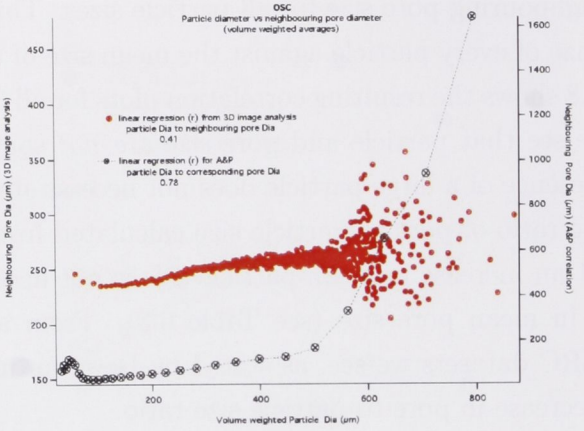

(a) OSC

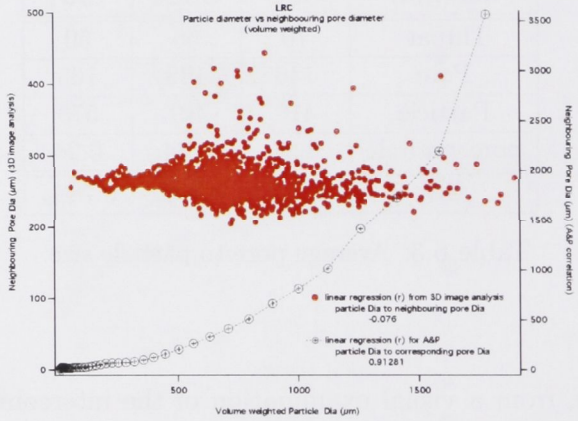

(b) LRC

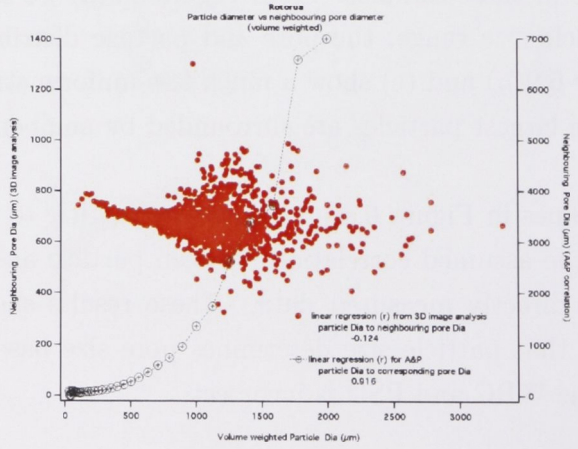

(c) Rotorua

Figure 6.8: Pore to particle correlation shows no spatial correlation between pore size and particle size.

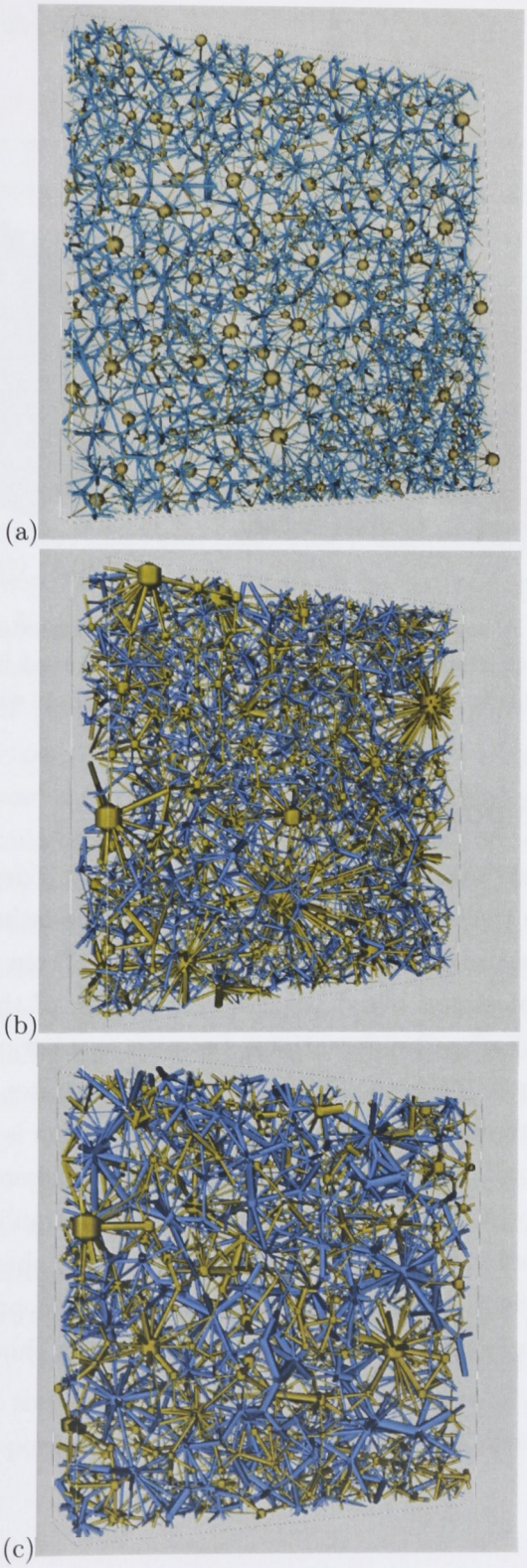

Figure 6.9: Pore and particle networks for (a) OSC, (b) LRC and (c) Rotorua, illustrating no visually apparent correlation between pore and particle sizes. All the figures are 110x500x500 voxel subsets showing the particle network in orange.

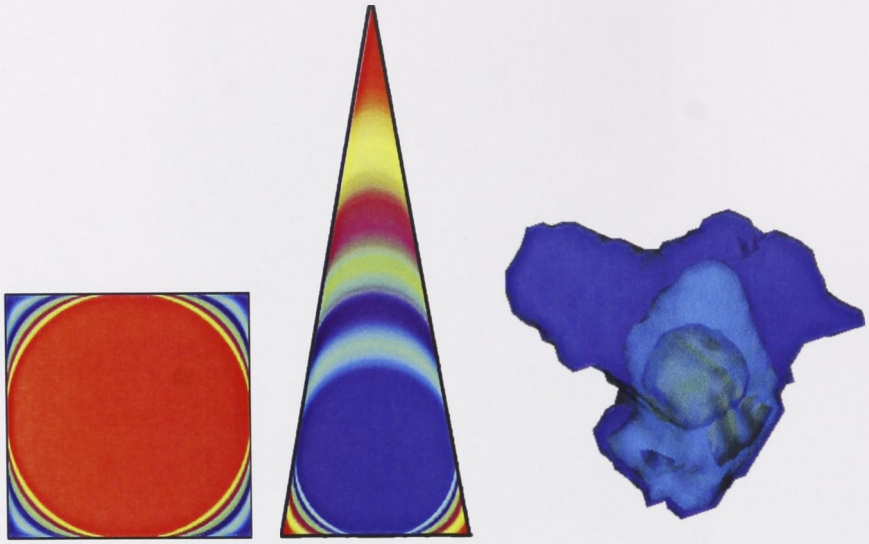

(a) (b) (c)

Figure 6.10: (a) A square pore with a G value approximately $0.8/4\pi$. (b) An elongated pore with a smaller G. (c) A real pore extracted from a tomographic image. Different shades of blue show where the wetting phase will reside at different saturations.

6.3.2 Other pore size information

Future work should consider the role of pore shape. This descriptor is directly quantifiable from the image and important when accounting for connectivity and capillary pressure effects that control the WRC. From the image a shape factor is often calculated based on the cross section of the 2D pore shape; G =Area/Perimeter^2. G differentiates between a spherical pore ($G = \frac{1}{4\pi}$) and a long thin pore ($G \to 0$). Figure 6.10 (a-b) illustrates 2 common shapes that have been attributed to real pores; the cross section is assumed constant along the full pore. The different colours represent where a wetting phase will reside at increasing saturations under capillary equilibrium. In Figure 6.10(c) a real pore is shown; it is apparent that pore shape descriptions in (a-b) are insufficient; use of these shapes may lead to poor estimations of capillary pressure, saturation and permeability. This should be pursued in further work.

6.4 Permeability

Flow and transport processes in porous media depend upon the geometric properties of their pores (Lehmann et al., 2006). The 3D characterisation of the pore structure enables one to calculate permeability on a realistic description of the connected pore space. This quantitative information can be compared to the estimations of permeability made by PTF calculations and other indirect estimations.

From the comparisons we find that the PTF investigated here (A&P) performed badly and systematically underestimated K due both to a flawed representation of pore space based on parallel tubes and the empirical nature of the correlation. The models that included a realistic representation of the flow paths (Berg, 1970; Panda and Lake, 1994), and critical geometric models (Katz and Thompson, 1986) performed much better. We find that generally $K_{A\&P} < K_{Berg} < K_{P\&L} \approx K_{lc} \approx K_{LB}$ (see Table 6.4).

The Berg derivation performs better than A&P but also underestimates K. The inclusion of packing, particle size, SD and particle shape results in a model that moves toward approximating the reality of an aggregate of non-uniform particles and the K_{Berg} calculations are approximately a factor of 3 less than that calculated from LB. Berg logically assumes that the greatest resistance to flow is contributed by the smallest pores and therefore explicitly includes them by the use of the sorting parameter $Pd_{\phi u}$, which states the greater the deviation from the median the greater the effect of small pore sizes. His conclusion is that one can assume that permeability is controlled by a dominant small pore size because in a natural sample large pores will alternate somewhat with small pores and the small pores will offer the greater resistance to flow. While his physical intuition is correct his correlation underestimates K. It is unclear why this is so. Perhaps a tortuosity factor accounting for the variation in flowpath length (τ approximately 3) would lead to a more accurate correlation.

Panda and Lake's model included an expanded number of PSD statistics to include not only the sorting of the material but also the skewness of the distribution and a tortuosity coefficient to more realistically model the pore space. This model performed well for both OSC and LRC but underestimated

K by a factor of almost 3 for the Rotorua sample. This error could be due to the poor estimation of PSD. However Panda and Lake's model was focussed on cleaner highly permeable sandstones.

The calculation of K using l_c from Katz and Thompson (1987) performed well on all 3 datasets. This parameter is not based on the PSD of the sample but is calculated directly from the pore-size distribution. For LRC an underestimation of less than 30% was achieved and a 10-15% deviation from LB found for OSC and Rotorua respectively. Using the same logic as Berg, Katz and Thompson reason that K is controlled by the smallest constrictions in the spanning cluster (l_c) and in so doing appear to have more accurately captured the reality of flow through a porous medium. It should be noted that we have used a modified prefactor (0.16 (Bauget et al., 2005a)) compared to Katz and Thompson (1986) original value of $\frac{1}{226}$. If we had used Katz and Thompsons' value we would have consistently underestimated K. A significant drawback to the Katz and Thompson method is in attaining a measure of l_c. In consolidated media this parameter is attainable from an MICP experiment but this technique is not suitable for application to friable material due to an inability to maintain natural structure and bulk density for the duration of the experiment. The experimental measurement of the WRC may have the potential to provide the analogous measure in a friable material and is worthy of further investigation.

	OSC	LRC	Rotorua
K (Darcies)			
A&P	0.3	12	24
Berg	34	21	74
P&L	77	104	214
l_c	70	64	698
LB	63	92	491

Table 6.4: Absolute permeability comparisons.

6.5 Relative permeability

Using the A&P algorithm and the LB simulation K_r curves for the samples have been calculated and compared (Figure 6.11). The K_r curves from A&P were very different to the curves calculated directly on the 3D image using LB. Figures 6.11(b) and (c) illustrate the distinct difference; the A&P results are dominated by large pores, therefore they do not significantly conduct until saturation reaches >80%. The largest 5-10% of the pores contributing as much as 95% of K. In contrast data from LB shows the largest 60% of the pores contribute significantly to overall K.

The multiphase flow properties simulated in this thesis assume a strongly water wet configuration; the wetting fluid, water, is concentrated in the smallest pores at saturations less than 100%. In reality wettability of soils can vary due to environmental alteration and presence of clays. The prediction of K_r requires a realisic mapping of wettability. Preliminary work on this problem has been undertaken via micro-CT and image analysis by Seright et al. (2006). In Figure 6.11 (d) we show data from micro-CT and partitioning from a strongly wetting system which illustrates the wetting fluid filling the smaller pores first.

Seright et al. (2006) have also shown the wetting fluid distribution in a mixed wet material. In this case the fluid is concentrated in pores of varying size. The effect of variability in wetting configuration will alter the K_r and WRC and should be considered in future work.

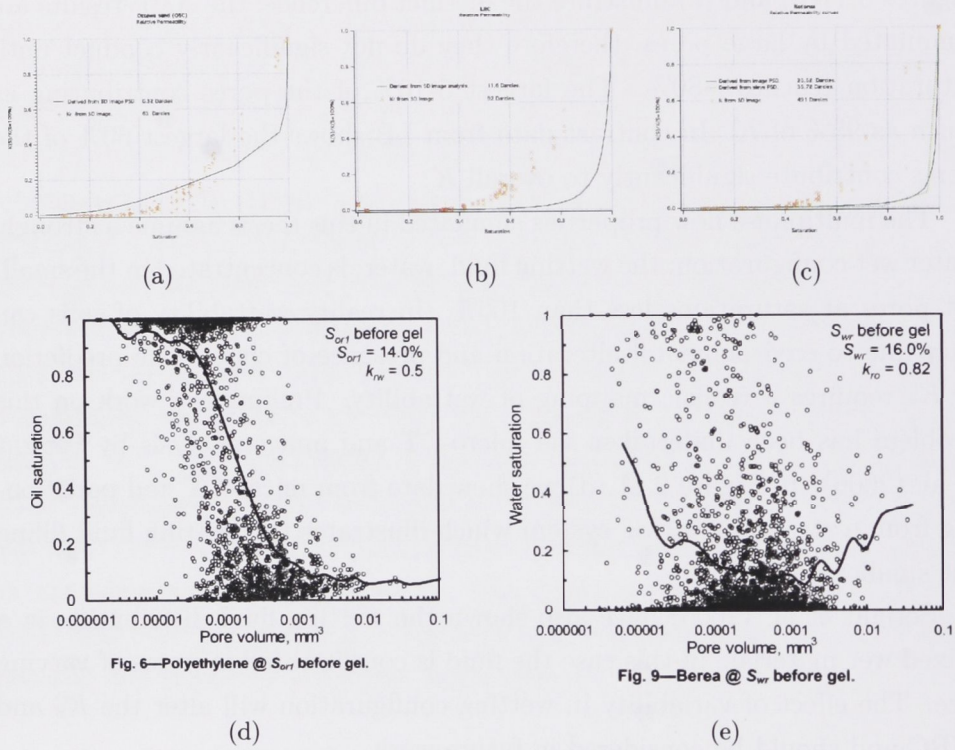

Figure 6.11: (a-c) K_r curves from A&P and LB calculations for OSC, LRC and Rotorua respectively. (d) Average residual oil saturation for >2000 individual pores in an oil wet smooth walled porous media as a function of pore size after drainage from Seright et al. (2006). Showing a conventional saturation curve in a smooth walled porous media (e) Residual water saturation for >2000 individual pores in rough walled Berea which allowed more efficient drainage of all pores via films and thus an even spread of saturation throughout the media regardless of pore size. ie. residual is not always related to capillary pressure.

Part IV

References

Bibliography

A. Allaby and M. Allaby. *Oxford Dictionary of Earth Sciences.* Oxford University Press, New York, 2nd edition, 1999.

M.P. Anderson. Hydrogeologic facies models to delineate large-scale spatial trends in glacial and glaciofluvial sediments. *Geological Society of America Bulletin*, 101(4):501–511, 1989.

C.H. Arns, M.A. Knackstedt, W.V Pinczewski, and W.B. Lindquist. Accurate estimation of transport properties from microtomographic images. *Geophysical Research Letters*, 28(17):3361–3364, 2001.

C.H. Arns, M.A. Knackstedt, W.V. Pinczewski, and N.S. Martys. Virtual permeametry on microtomographic images. *Journal of Petroleum Science and Engineering*, 45(1-2):41–46, 2004.

C.H. Arns, F. Bauget, A. Ghous, A. Sakellariou, T.J. Senden, A.P. Sheppard, R.M. Sok, W.V. Pinczewski, J.C. Kelly, and M.A. Knackstedt. Digital Core Laboratory - Petrophysical analysis from 3D imaging of reservoir core fragments. *Petrophysics*, 46(4):260–277, 2005a.

C.H. Arns, M.A. Knackstedt, and N.S. Martys. Cross-property correlations and permeability estimation in sandstone. *Physical Review E*, 72(4), 2005b. Part 2.

L.M. Arya and J.F. Paris. A physicoempirical model to predict the soil moisture characteristic from particle size distribution and bulk density data. *Soil Science Society of America Journal*, 45(6):1023–1030, 1981.

L.M. Arya, F.J. Leij, P.J. Shouse, and M.Th. van Genuchten. Relationship between the hydraulic conductivity function and the particle size distribution. *Soil Science Society of America Journal*, 63:1063–1070, 1999a.

L.M. Arya, F.J. Leij, M. T. van Genuchten, and P.J. Shouse. Scaling parameter to predict the soil water characteristic from particle size distribution data. *Soil Science Society of America Journal*, 63(3):510–519, 1999b.

S. Assouline. A model for soil relative hydraulic conductivity based on the water retention characteristic curve. *Water Resources Research*, 37(2): 265–271, 2001.

S. Assouline and Y. Rouault. Modeling the relationships between particle and pore size distributions in multicomponent sphere packs: Application to the water retention curve. *Colloids and Surfaces a-Physicochemical and Engineering Aspects*, 127(1-3):201–210, 1997.

F. Bauget, C.H. Arns, M. Saadatfar, A.P. Sheppard, R.M. Sok, M.L. Turner, W.V. Pinczewski, and M.A. Knackstedt. What is the characteristic length scale of permeability? Direct analysis from microtomographic data. In SPE, editor, *2005 SPE ATCE*, volume 95950, Dallas, Texas, USA., 2005a. Society of Petroleum Engineers.

F. Bauget, C.H. Arns, M. Saadatfar, M.L. Turner, A.P. Sheppard, R.M. Sok, W.V. Pinczewski, and M.A. Knackstedt. Rock typing and petrophysical property estimation via direct analysis on microtomographic images. *Society of Core Analysts*, 2005b.

R.R. Berg. Method for determining permeability from reservoir rock properties. *Transactions of the Gulf Coast Association of Geological Sciences*, 20:303, 1970.

D.A. Berkman. *Field Geologists Manual.* The Australasian Institute of Mining and Metallurgy, Carlton, Victoria, Australia., 1995.

J. D. Bernal and J. Mason. Co-ordination of randomly packed spheres. *Nature*, 188(4754):910–911, 1960.

L. Beuselinck, G. Govers, J. Poesen, G. Degraer, and L. Froyen. Grain size analysis by laser diffractometry. comparison with the sieve pipette method. *Catena*, 32:193–208, 1998.

H. Blatt, G. Middleton, and R. Murray. *Origin of sedimentary rocks.* Prentice Hall Inc. USA, 1972.

J. Blouwolff and S. Fraden. The coordination number of granular cylinders. *Europhysics Letters*, 76(6):1095–1101, 2006.

J. Bouma, O. Jongerius, O. Boersma, A. Jager, and Schoonderbeek. The function of different types of macropores during saturated flow through four swelling soil horizons. *Soil Science Society of America Journal*, 41: 945–950, 1977.

S.A. Bradford and M. Bettahar. Straining, attachment, and detachment cryptosporidium oocysyts in saturated porous media. *Journal of Environmental Quality*, 34(2):469–479, 2005.

S.A. Bradford, K.M. Rathfelder, J. Lang, and L.M. Abriola. Entrapment and dissolution of DNAPLs in heterogeneous porous media. *Journal of Contaminant Hydrology*, 67:133–157, 2003.

P. Buurman, Th. Pape, and C.C. Muggler. Laser grain size determination in soil genetic studies 1. Practical problems. *Soil Science*, 162(3):211–218, 1997.

J.R. Campbell. Limitations in the laser particle sizing of soils. In Ian Roach, Aspandiar Mehrooz, John Field, Rob Fitzpatrick, and Steven Hill, editors, *Advances in Regolith: Proceedings of the CRCLEME Regional Regolith Symposia, 2003*, volume 1, pages 38–42, Australian National University, Canberra, ACT. Australia, 2003. Cooperative Research Centre for Landscape Environments and Mineral Exploration, PO Box 1130, Bentley, WA, 6102.

P.C. Carman. Fluid flow through a granular bed. *Transactions of the Institution of Chemical Engineers.*, 15:150–167, 1937.

D.W. Carrier. Goodbye, Hazen; Hello, Kozeny-Carmen. *Journal of Geotechnical and Geoenvironmental Engineering*, 129(11):1054–1056, 2003.

D. Chakraborty, A. Chakraborty, P. Santra, R.K. Tomar, R.N. Garg, R.N. Sahoo, S.G. Choudhury, M. Bhavanarayana, and N. Kalra. Prediction of hydraulic conductivity of soils from particle-size distribution. *Current Science*, 90(11):1526–1531, 2006.

P.A. Domenico and F.W. Schwartz. *Physical and Chemical Hydrogeology.* John Wiley and Sons, Inc, Brisbane, 2nd edition, 1998.

E.R. Dougherty and R.A. Lotufo. *Hands on morphological image processing.* SPIE. The Intenational Society for Optical Engineering, Bellingham, Washington. USA., 2003.

J.P. Duplessis and J.H. Masliyah. Flow through isotropic granular porous-media. *Transport in Porous Media*, 6(3):207–221, 1991.

J.R. Eggleston. Can we predict subsurface mass transport? *Environmental science and technology*, 34(18):4010–4017, 2000.

J.R. Eggleston and S. Rojstaczer. Identification of large-scale hydraulic conductivity trends and the influence of trends on contaminant transport. *Water Resources Research*, 34(9):2155–2168, 1998.

J.R. Eggleston and S. Rojstaczer. The value of grain-size hydarulic conductivity estimates: Comparison with high resolution in-situ field hydraulic conductivity. *Geophysical Research Letters*, 28(22):4255–4258, 2001.

G. Eshel, G.J. Levy, U. Mingelgrin, and M.J. Singer. Critical evaluation of the use of laser diffraction for particle-size distribution analysis. *Soil Science Society of America Journal*, 68:736–743, 2004.

U. Fauzi, A. Hoerdt, and F.M. Neubauer. Influence of coordination number and percolation probability on rock permeability estimation. *Geophysical Research Letters*, 29(8), 2002.

L.A. Feldkamp, L.C. Davis, and J.W. Kress. Practical cone-beam algorithm. *Journal of the Optical Society of America A - Optics Image Science and Vision*, 1(6):612–619, 1984.

B. Ferreol and D.H. Rothman. Lattice-Boltzmann simulations of flow through Fontainebleau sandstone. 20:3–20, 1995.

L. Feyen and S.M. Gorelick. Framework to evaluate the worth of hydraulic conductivity data for optimal groundwater resources management in ecologically sensitive areas. *Water Resources Research*, 41(3), 2005.

J.C. Fiés and A. Bruand. Particle packing and organisation of the textural porosity in clay-silt-sand mixtures. *European Journal of Soil Science*, 49: 557–567, 1998.

E. Fillion and M-L. Moyer. Flow modelling in a dual porosity domain with automatic mesh generation and parameter calibration: application to the Aspo site. *Journal of Hydrology*, 180:1–19, 1996.

R.L. Folk and W.C. Ward. Brazos river bar; a study in the significance of grain size parameters. *Journal of Sedimentary Petrology*, 27:3–27, 1957.

D.G. Fredlund. The 1999 R.M. Hardy lecture: The implementation of unsaturated soil mechanics into geotechnical engineering. *Canadian Geotechnical Journal*, 37(5):963–986, 2000.

D.G. Fredlund and A. Xing. Equations for the soil water characteristic curve. *Canadian Geotechnical Journal,*, 31(3):521–532, 1994.

M.D. Fredlund, D.G. Fredlund, and G.W. Wilson. An equation to represent grain size distribution. *Canadian Geotechnical Journal*, 37(4):817–827, 2000.

E.J. Garboczi. Three-dimensional mathematical analysis of particle shape using x-ray tomography and spherical harmonics: Application to aggregates used in concrete. *Cement and Concrete Research*, 32(10):1621–1638.

E.J. Garboczi and D.P. Bentz. Advances in cementitous materials. *Ceramics Transactions*, 16:365–380, 1991.

L.C. Graton and H.J. Fraser. Systematic packing of spheres with particular relation to porosity and permeability and experimental study of the porsity and permeability of clastic sediments. *Journal of Geology*, 43:785–909, 1935.

D. Hansen. Discussion of "On the use of the Kozeny-Carman equation to predict the hydraulic conductivity of soils". *Canadian Geotechnical Journal*, 41:990–993, 2004.

R. Hilfer. Local porosity theory for electrical and hydrodynamical transport through porous-media. *Physica A*, 194(1-4):406–414, 1993.

D Hillel. *Soil and water: Physical principles and processes.* Academic, New York, 1971.

M. Hilpert, R. Glantz, and C. T. Miller. Calibration of a pore-network model by a pore- morphological analysis. *Transport in Porous Media*, 51(3):267–285, 2003.

T. Inamuro, M. Yoshino, and F. Ogino. Non slip boundary condition for lattice-Boltzmann simulations. *Physics of Fluids*, 7(12):2928–2930, 1995.

R.M. Jones. Particle size analysis by laser diffraction: ISO 13320, standard operating procedures, and Mie theory. *American Laboratory*, 35(1), 2003.

R. Kasteel, H.-J. Vogel, and K. Roth. From local hydraulic properties to effective transport in soil. *European Journal of Soil Science*, 51:81–91, 2000.

A.J. Katz and A.H. Thompson. Quantitative prediction of permeability in porous rock. *Physical Review B*, 34(11):8179–8181, 1986.

A.J. Katz and A.H. Thompson. Prediction of rock electrical conductivity from mercury injection measurements. *Journal of GEOPhysical Research*, 92(B1):599–607, 1987.

A.A. Keller and S. Sirivithayapakorn. Early breakthrough of colloids and bacteriophage MS2 in a water-saturated sand column. *Water Resources Research*, 40, 2004.

N. Kettle, L. Harrington, and J. Harrington. Groundwater depletion and agricultural land use change in the high plains: A case study from Wichita County, Kansas. *Professional Geographer*, 59(2):221–235, 2007.

C.E. Koltermann and S.M. Gorelick. Heterogeneity in sedimentary deposits: A review of structure-imitating, process-imitating, and descriptive approaches. *Water Resources Research*, 32(9):2617–2658, 1996.

M. Konert and J. Vandenberghe. Comparison of laser grain size analysis with pipette and sieve analysis: a solution for the underestimation of the clay fraction. *Sedimentology*, 44:523–535, 1997.

J. Kozeny. Uber kapillare Leitung des Wassers in Boden (About capillaries conducting water in the earth). *Sitzungsberichte der Mathematisch-Naturwissenschaftlichen Classe der Kaiserlichen Akademie der Wissenschaften. (Committee Report of the Viennese Academy).*, 136(IIA):271–306, 1927.

W.C. Krumbein. Measurement and geological significance of shape and roundness of sedimentary particles. *Journal of Sedimentary Petrology*, 11: 67–76, 1941.

K.C. Lawrie, T.J. Munday, D.L. Dent, D.L. Gibson, R.C. Brodie, J. Wilford, N.S. Reilly, R.A. Chan, and P. Baker. A geological systems approach to understanding the processes involved in land and water salinisation. *AGSO Research Newsletter*, May:13–32, 2000.

J. Y. Lee, Y. K. Choi, H. S. Kim, and S. T. Yun. Hydrologic characteristics of a large rockfill dam: Implications for water leakage. *Engineering Geology*, 80(1-2):43–59, 2005.

P. Lehmann, P. Wyss, A. Flisch, E. Lehmann, P. Vontobel, M. Krafczyk, A. Kaestner, F. Beckmann, A. Gygi, and H. Fluhler. Tomographical imaging and mathematical description of porous media used for the prediction of fluid distribution. *Vadose Zone Journal*, 5(1):80–97, 2006.

Y. Li, D. Chen, R.E. White, A. Zhu, and J. Zhang. Estimating soil hydraulic properties of Fengqiu County soils in the North China Plain using pedotransfer functions. *Geoderma*, 138(3-4):261–271, 2007.

C.L. Lin and J.D. Miller. Pore structure analysis of particle beds for fluid transport simulation during filtration. *International Journal of mineral processing*, 73:281–294, 2004.

L.-L Loizeau, D. Arbouille, S. Santiago, and J.-P Vernet. Evaluation of a wide range laser diffraction grain size analyser for use with sediments. *Sedimentology*, 41:353–361, 1994.

J. Loveday, editor. *Methods for analysis of irrigated soils. Technical Communication No. 54 of the Commonwealth Bureau of Soils.* Commonwealth Agricultural Bureaux, 1974.

R. Ludwig, K. Schelkes, P. Vogel, and J. Wollrath. Implications of large-scale heterogeneities for hydraulic model studies at the potential site of a radioactive waste repository at Gorleben, Germany. *Engineering Geology*, 61:119–130, 2001.

N.S. Martys. Improved approximation of the Brinkman equation using a lattice Boltzmann method. *Physics of Fluids*, 13(6):1807–1810, 2001.

N.S. Martys and H. Chen. Simulation of multicomponent fluids in complex three-dimensional geometries by the lattice Boltzmann method. *Physical Review E*, 53(1):743–750, 1996.

N.S. Martys, J.G. Hagedorn, D. Goujon, and J.E. Devaney. Large-scale simulations of single and multicomponent flow in porous media. volume 3772, pages 205–213. SPIE, 1999.

M.D. Matthews, editor. *The dffect of grain shape and density on the size measurement* . Principals, methods, and applications of particle size analysis. Cambridge University Press, Cambridge, 1991.

A.B. McBratney, B. Minasny, and S.R. Cattle. From pedotransfer functions to soil inference systems. *Geoderma*, 109:41–73, 2002.

I.N. McCave, R.J. Bryant, H.F. Cook, and C.A. Coughanowr. Evaluation of a laser-diffraction-size analyzer for use with natural sediments. *Journal of Sedimentary Petrology*, 56:561–564, 1986.

H.W. Meinardus, V. Dwarakanath, J. Ewing, G.J. Hirasaki, R.E. Jackson, M. Jin, J.S. Ginn, J.T. Londergan, C.A. Miller, and G.A. Pope. Performance assessment of NAPL remediation in heterogenous alluvium. *Journal of Contaminant Hydrology*, 54:173–193, 2002.

D.U. Ophori. Constraining permeabilities in a large scale groundwater system through model calibration. *Journal of Hydrology*, 224:1–20, 1999.

S. Ozcoban, M.M. Berilgen, H. Kilic, T.B. Edil, and I.K. Ozaydin. Staged construction and settlement of a dam founded on soft clay. *Journal of Geotechnical and Geoenvironmental Engineering*, 133(8):1003–1016, 2007.

C. Pan, M. Hilpert, and C.T. Miller. Lattice - Boltzman simulation of two-phase flow in porous media. *Water Resources Research*, 40(1), 2004.

M.N. Panda and L.W. Lake. Estimation of single phase permeability from parameters of particle size distribution. *AAPG Bulletin. American Association of Petroleum Geologists*, 78(7):1028–1039, 1994.

L. Paterson, S. Painter, M.A. Knackstedt, and W.V Pinczewski. Patterns of fluid flow in naturally heterogenous rocks. *Physica A*, 233:619–628, 1996.

M.C. Powers. A new roundness scale for sedimentary particles. *Journal of Sedimentary Petrology*, 23:117–119, 1953.

Y.H. Qian, D. d'Humiéres, and P. Lallemand. Lattice BGK models for Navier-Stokes equation. *Euro Physical Letters*, 17:479, 1992.

H. Rajaram, L.A. Ferrand, and M.A. Celia. Prediction of relative permeabilities for unconsolidated soils using pore-scale network models. *Water Resources Research*, 33(1):43–52, 1997.

H. Ruan and T.H. Illangasekare. Estimation of relative hydraulic conductivity of sandy soils based on a sheet flow model. *Journal of Hydrology*, 219: 83–93, 1999.

M. Saadatfar. *Morphological and mechanical characterisation of microstructural materials.* PhD, Australian National University, 2007.

M. Saadatfar, C.H. Arns, M.A. Knackstedt, and T.J. Senden. Mechanical and transport properties of polymeric foams derived from 3D images. *Colloids and Surfaces A:Physicochemical and Engineering Aspects*, 263(1-3):284–289, 2005.

M. Sahimi. Flow phenomena in rocks: from continuum to fractals, percolation, cellular automata, and simulated annealing. *Reviews of Modern Physics*, 65(4):1393–1534, 1993.

A. Sakellariou, T.J. Sawkins, T.J. Senden, and A. Limaye. X-ray tomography for mesoscale physics applications. *Physica A*, 339:152–158, 2004a.

A. Sakellariou, T.J. Senden, T.J. Sawkins, M.A. Knackstedt, M.L. Turner, A.C. Jones, M. Saadatfar, R.J. Roberts, A. Limaye, C.H. Arns, A.P. Sheppard, and R.M. Sok. An x-ray tomography facility for quantitative prediction of mechanical and transport properties in geological, biological and synthetic systems. In Ulrich Bonse, editor, *Developments in X-ray Tomography IV.*, pages 473–484. SPIE, Bellingham, WA USA, 2004b.

R.S. Seright, M. Prodanovic, and W.B. Lindquist. X-ray computed microtomography studies of fluid partitioning in drainage and imbibition before and after gel placement: Disproportionate permeability reduction. *SPE Journal*, 11(2):159–170, 2006.

A.P. Sheppard, R.M. Sok, and H. Averdunk. Techniques for image enhancement and segmentation of tomographic images of porous materials. *Physica A. Statistical Mechanics and Its Applications*, 339(1-2):145–151, 2004.

A.P Sheppard, R.M. Sok, and H. Averdunk. Improved pore-network extractions. In *19th International Symposium of the Society of Core Analysts*, volume SCA2005-P89, Toronto, Canada., 2005. Society of Core Analysts.

A.P. Sheppard, R.M. Sok, H. Averdunk, V.B. Robins, and A. Ghous. Analysis of rock microstructure using high-resolution x-ray tomography. In

Proceedings of the Society of Core Analysts, Trondheim, Norway, 2006. Society of Core Analysts.

K.R.J. Smettem, Y.M. Oliver, L.K. Heng, K.L. Bristow, and E.J. Ford. Obtaining soil hydraulic properties for water balance and leaching models from survery data. 1. Water retention. *Australian Journal of Agricultural Research*, 50:283–289, 1999.

E.D. Sneed and R.L. Folk. Pebbles in the Lower Colorado River, Texas a Study in Particle Morphogenesis. *Journal of Geology*, 66(2):114–150, 1958.

M. Solymar and I.L. Fabricius. Image analysis and estimation of porosity and permeability of Arnager Greensand, Upper Cretaceous, Denmark. *Physics and Chemistry of the Earth (A)*, 24(7):587–591, 1999.

M. Swartz, B.D.R. Misstear, D. Daly, and E.R. Farrell. Assessing subsoil permeability for groundwater vulnerability. *Quarterly Journal of Engineering Geology and Hydrogeology*, 36:173–184, 2003. Part 2.

K. Tan, V. Berens, M. Hatch, T. Munday, and K.C. Lawrie. Mapping zones of saline groundwater discharge using Nano TEM, River Murray, South Australia. In *Geophysical Applications for Environmental and Engineering Hazards - Advances and Constraints*, pages 60–68, Doubletree Hotel, Seattle, Washington., 2006. Society of Applied Geophysics for Environmental and Engineering Problems: SAGEEP.

The Standards Association of Australia. AS 1289.3.6.2-1995, Australian Standard Methods of testing soils for engineering purposes. Method 3.6.2: Soil classification tests -Determination of the particle size distribution of a soil -Analysis by sieving in combination with hydrometer analysis (subsiduary method), 1995.

The Standards Association of Australia. AS 4863.1-2000, Australian Standard Particle size analysis -Laser diffraction methods. Part 1: General principles. ISO 13320-1:1999, 2000.

The Standards Association of Australia. AS 1289.3.6.3-2003, Australian Standard Method of testing soils for engineering purposes. Method 3.6.3:

Soil classification tests - Determination of the particle size distribution of a soil - Standard method of fine analysis using a hydrometer., 2003.

C.D. Tsakiroglou and A.C. Payatakes. Characterisation of the pore structure of reservoir rocks with the aid of serial sectioning analysis, mercury porosimetry and network simulation. *Advances in Water Resources*, 23: 773–789, 2000.

J.A. Udden. Mechanical composition of wind deposits. *Augustana Library Publication*, 1, 1898.

US Army Corps of Engineers. Engineering and Design. Geotechnical Investigations. EM 1110-1-1804, 2001.

P.H. Valvatne, M. Piri, X. Lopez, and M.J. Blunt. Predictive pore-scale modeling of single and multiphase flow. *Transport in Porous Media*, 58 (1-2):23–41, 2005.

C.M.P. Vaz, M.D. Iossi, J.D. Naime, A. Macedo, J.M. Reichert, D.J. Reinert, and M. Cooper. Validation of the Arya and Paris water retention model for Brazilian soils. *Soil Science Society of America Journal*, 69(3):577–583, 2005.

M. Viana, P. Jouannin, C. Pontier, and D. Chulia. About pycnometric density measurments. *Talanta*, 57:583–593, 2002.

H. Wadell. Volume, shape and roundness of rock particles. *Journal of Geology*, 40:443–451, 1932.

H. Wadell. Sphericity and roundness of rock particles. *Journal of Geology*, 41:310–331, 1933.

H. Wadell. Volume, shape and roundness of quartz particles. *Journal of Geology*, 43:250–280, 1935.

R. Webster. The development of pedometrics. *Geoderma*, 62:1–15, 1994.

C.K. Wentworth. A scale of grades and class terms for clastic sediments. *Journal of Geology*, 30:377–392, 1922.

I. White and M.J. Sully. Macroscopic and microscopic capillary length and time scales from field infiltration. *Water Resources Research*, 23(8):1514–1522, 1987.

J.H.M. Wösten, Y.A. Pachepsky, and W.J. Rawls. Pedotransfer functions: bridging the gap between available basic soil data and missing soil hydraulic characteristics. *Journal of Hydrology*, 251:123–150, 2001.

R.L. Xu and O.A. Di Guida. Comparison of sizing small particles using different technologies. *Powder Technology*, 132(2-3):145–153, 2003.

T. Zingg. Beitrage zur Schotteranalyse. Die Schotteranalyse und ihre Anwendung auf die Glattalschotter. *Schweizerische Mineralogische und Petrographische Mitteilungen*, 15:39–140, 1935.